

PROGRESS REPORT

Wave Particle Interactions in Nonneutral Plasmas

for calendar year 1994

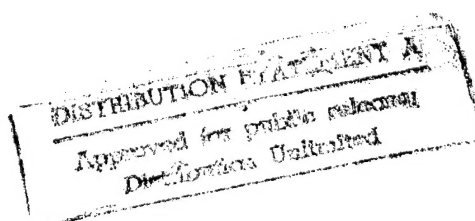
sponsor:

**Office of Naval Research
Grant N00014-89-J-1264**



from:

***California Institute of Technology
Pasadena, California 91125
Roy W. Gould, Principal Investigator***



19950925 088

CONTENTS

Publication:

Damping and Trapping in 2D Inviscid Fluids

Manuscripts Submitted:

2D Dynamics of Nonneutral Plasmas

Theory of Cyclotron Resonance in a Cylindrical Nonneutral Plasma

Papers presented at the 1994 A. P. S. Meeting

Dynamics of Nonneutral Plasmas

Negative Energy and Dispersion of the Diocotron Resonances

Numerical Collisionless Damping of the Diocotron Resonance

Accession For	
NTIS GRA&I	<input checked="checked" type="checkbox"/>
DTIC TAB	<input type="checkbox"/>
Unannounced	<input type="checkbox"/>
Justification	
By <i>Perletter</i>	
Distribution/As	
Availability Codes	
Dist	Avail and/or Special
<i>A-1</i>	

Damping and Trapping in 2D Inviscid Fluids

N. Sateesh Pillai and Roy W. Gould

California Institute of Technology, Pasadena, California 91125

(Received 6 July 1993; revised manuscript received 11 August 1994)

We demonstrate collisionless decay due to phase mixing of a disturbance in an inviscid 2D fluid with sheared flow. Experiments performed on a cylindrical pure electron plasma, which behaves as a 2D inviscid fluid, show that a small amplitude quadrupole excitation ($m = 2$, $k = 0$ mode) decays exponentially. At larger amplitudes, the exponential decay is modulated by bounce motion of fluid elements trapped in the azimuthally traveling wave field, with the bounce frequency proportional to the square root of the excitation amplitude. We also show that the linear decay rate is *decreased* by the addition of external dissipation. We describe a calculation of the linearized response function.

PACS numbers: 47.15.Ki, 52.25.Wz, 52.35.Lv, 52.35.Mw

Two-dimensional flow of incompressible inviscid fluids has a long history [1–3]. The 2D behavior of non-neutral plasmas, in the drift approximation, is analogous to that of inviscid fluids [4,5], with equipotentials as fluid streamlines and plasma density proportional to vorticity. Very recently this property has been exploited to study several classic problems in 2D vortex dynamics [5–8]. In sheared 2D flows, disturbances are convected in different layers with different velocities, and this is predicted to lead to collisionless decay of disturbances due to phase mixing. For example, using an initial value approach, Case [3] showed theoretically that in planar Couette flow of an inviscid fluid, small perturbations decay algebraically in the asymptotic limit. Briggs *et al.* [4], in a theoretical study, also argued that small 2D perturbations in a cylindrical non-neutral plasma column with sheared flow are expected to decay due to a collisionless phase mixing process similar to Landau damping of Langmuir oscillations [9]. deGrassie [10] was the first to search for this phenomena experimentally. Although he found the perturbations decayed, the decay rates obtained were about 2 orders of magnitude smaller than expected, and they decreased with increasing amplitude of excitation, i.e., a *nonlinear* behavior. The sensitivity of his receiver was inadequate to observe the linear regime.

We present three new experimental results on vortex dynamics. (a) We observe collisionless damping of 2D disturbances of the form $\exp[i m \theta + i k z - i \omega t]$, with $m = 2$ and $k = 0$, in an inviscid fluid in the *linear* regime. (b) We find that as the amplitude of excitation is increased, the decay rate is modulated periodically in a manner consistent with bounce motion of trapped fluid elements in the field of the disturbance. This is in accordance with the early picture of Kelvin's cat's eyes [2] and a prediction of Briggs *et al.* [4] that the bounce frequency should be proportional to the square root of the perturbed amplitude. This phenomenon is qualitatively similar to the effect of bounce oscillations of particles trapped by a Langmuir mode [11–13]. (c) We show that adding external dissipation to the system *reduces* the

linear damping rate, thus demonstrating that the mode has *negative energy*, i.e., excitation of the mode reduces the energy of the system.

We also describe a calculation of the linear response function of a 2D cylindrical fluid which exhibits exponential decay at early times, associated with a simple pole, followed by a transition to algebraic decay, similar to the asymptotic prediction of Case [3]. This response function also shows that the mode has *negative energy*.

Our experiments were performed using a cylindrical pure electron plasma column illustrated in Fig. 1(a). Electrons emitted from a hot thoriated tungsten filament are injected into the trap region where they are confined in the radial direction by a 50 G magnetic field and in the axial direction by electrostatic traps held at -100 V. The trapped electrons will rotate around the cylinder axis under steady state. A radial monotonically

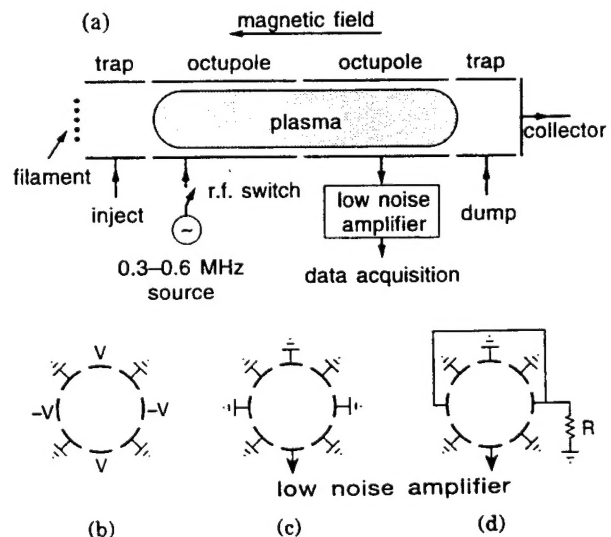


FIG. 1. (a) Schematic of cylindrical structure for plasma trapping and excitation. (b) phasing of first octupole for exciting an $m = 2$ disturbance, (c) configuration of second octupole for signal reception, and (d) configuration of second octupole for negative energy test.

decreasing particle density profile (vorticity profile in fluid terms) produces a monotonically decreasing angular velocity of fluid rotation, i.e., sheared flow. The plasma radius and lengths are 1.2 and 40 cm, respectively. The cyclotron frequency, central plasma, and rotation frequencies are about 140 MHz, 10 MHz, and 350 kHz, respectively. The Reynolds number is estimated to be 10^4 . Other aspects of this device have been described earlier [14]. The experiment is performed in a repetitive inject-observe-dump cycle. The trapped plasma is excited by a 5 μ sec burst of 300 to 600 kHz sinusoid on one octupole set. The frequency of the rf pulse is adjusted so as to maximize the response of the $m = 2$ mode, typically 2–4 times the frequency of the well studied $m = 1$ diocotron mode [9]. As shown in Fig. 1(b), signal phases on the octupole sectors generate an $m = 2$ field. The charge induced on one sector of a second octupole section is amplified by a low noise charge amplifier and digitized. The response to the short burst, after it has ended, is a decaying sinusoid as shown in the inset of Fig. 2. Each digitized signal is processed by passing it through a software peak detector to obtain the envelope of the decaying sinusoid. The envelopes of 20 decays (typically) at the same amplitude are averaged and the process repeated for applied voltage between 10 mV to 1 V. The averaged envelopes are shown on a semilogarithmic plot in Fig. 2. For clarity, the traces in the plot are stopped when the signal becomes comparable with the system noise level. The lowest four traces in Fig. 2 evidently represent the linear regime, since the response is simply proportional to the applied voltage. The linear decay rate is $\gamma = 34.3$ krad/sec and $\omega/\gamma = 84$. The

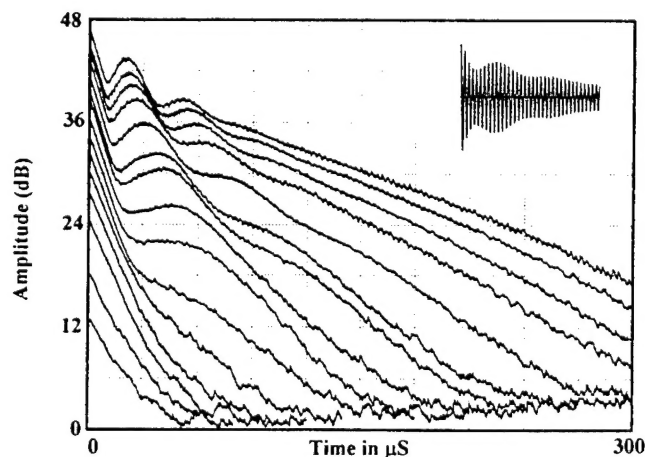


FIG. 2. Decay of the envelope of $m = 2$ signal at about 400 kHz, excited by an rf pulse with voltages 10, 20, 40, 60, 80, 120, 160, 200, 250, 300, 400, 500, 600, 700, and 1000 mV. Lower left curve corresponds to 10 mV rf voltage and uppermost curve corresponds to 1000 mV. Plotted on semilogarithmic scale with vertical scale calibrated in dB. Time scale starts with $t = 0$ at the end of the rf pulse. Inset shows received signal for 500 mV applied voltage.

decay time in the linear regime is much shorter than the electron-electron collision time of 10 msec. Hence this decay is *collisionless*. The *initial* decay rates for *all* traces during the first 15 μ sec are approximately the same. Later in time and at higher amplitudes, the decay rate is periodically modulated, with the shortest modulation period occurring at the highest amplitude. At the lower amplitudes, the modulation period becomes larger than the decay time and the nonlinear modulation phenomenon disappears. At these low amplitudes, a fluid element cannot complete a trapped orbit before the mode decays and, in effect, does not know that it is trapped. At higher amplitudes a fluid element is able to complete a trapped orbit before the mode decays and the modulation of the wave amplitude becomes noticeable. The smallest observable bounce frequency, 94.3 krad/sec, is larger than the linear decay rate. At the largest amplitudes, the late-time decay is much slower, and we find a nonlinear behavior in which the decay rate decreases with increasing amplitude, similar to that described by deGrassie [10].

In order to determine the dependence of the bounce period on the mode potential we have analyzed the data of Fig. 2 in the following way. First, we determine a least squares exponential fit to the early part of one of the traces to get the average rate of decay. We then subtract this exponential from that trace and determine the bounce period by measuring the time between successive maxima. We observe that the period lengthens as the mode decays, as expected. We correct the mode potential for this decay using the exponential function and, assuming the initial mode potential to be proportional to the applied voltage, plot the resulting bounce frequency versus the corrected *applied* potential. Figure 3 shows the resulting bounce frequency f versus V on a log-log plot. A least squares fit of the form $f = AV^n$ to the data, shown by the solid line, gives $n = 0.44$ and $A = 2.77$ (f in kHz and V in mV). Calculations for 21 other data sets, similar to those shown in Figs. 2 and 3, give values of n between 0.42 and 0.77 with a mean value of 0.55 ± 0.10 . This is equal, within experimental error, to the value of 0.5 expected for oscillations of trapped particles in the mode [4], and reinforces our conclusion that the amplitude modulation of the decaying $m = 2$ mode is due to fluid trapping at a radius where the local angular velocity is equal to the mode velocity.

We now sketch the theoretical calculation of the linear response function of the system associated with a single m value, namely $m = 2$. The response of the plasma to a burst of sinusoid of amplitude V is induced current I in the wall of the electrode (Fig. 1). In the linear regime, the Fourier transform of I is related to the Fourier transform of V through a *transfer* admittance $Y(\omega)$: $I(\omega) = V(\omega)Y(\omega)$. It is easy to show that $Y(\omega) = i\omega 2\pi\epsilon_0 L F_1 F_2 (rE_r/\phi)_{r=b}$, where L is the total length of the trap, F_1 and F_2 are geometrical form

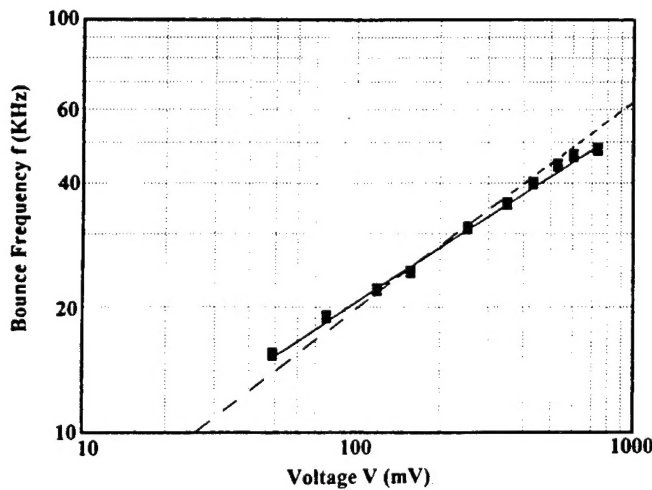


FIG. 3. Bounce frequency f versus voltage V (applied voltage corrected for the decay) plotted on a log-log scale. Filled boxes correspond to data. Solid line is a least squares fit $f = AV^n$, where $n = 0.44$. Together with 21 other data sets, $n = 0.55 \pm 0.1$. Dashed line shows a line where $n = 0.5$ for comparison.

factors (<1) pertaining to length, mode number m , and phasing of the sectors of the input and output octupole sections. E_r/ϕ represents the ratio of the radial electric field to the potential and should be evaluated at the wall ($r = b$). $Y(\omega)$ is just the Fourier transform of the impulse response of the plasma. The value of E_r/ϕ at the wall can be obtained by solving the linearized equation for the potential [4,5]:

$$\frac{d^2\phi}{dr^2} + \frac{1}{r} \frac{d\phi}{dr} - \frac{m^2}{r^2} \phi + \frac{me}{\epsilon_0 B_0} \frac{dn_0(r)/dr}{r[\omega - m\omega_0(r)]} \phi = 0, \quad (1)$$

where $n_0(r)$ represents the particle density and $\omega_0(r)$ the angular velocity of electrons of charge e confined in a magnetic field B_0 . For a band of ω 's a mode particle resonance will occur at a radius r_s within the plasma where $m\omega_0(r_s) = \omega$, giving rise to a logarithmic singularity in ϕ at $r = r_s$. To solve Eq. (1) requires a knowledge of $n_0(r)$ from which $\omega_0(r)$ is determined. Power series expressions have been obtained for special profile functions, but for a greater variety of profiles we also integrate Eq. (1) numerically for various ω . In order to deal with the singularity at $r = r_s$ in the solution of Eq. (1), ω is assumed to have a small positive imaginary part. Using this technique we obtain the frequency-dependent real and imaginary parts of $(rE_r/\phi)_b$ that are shown in Fig. 4(a). The corresponding envelope of the impulse response is obtained by taking the inverse Fourier transform of $(rE_r/\phi)_b$ and is shown in Fig. 4(b). $(rE_r/\phi)_b$ can be fit rather well by the expression for a simple pole, plus a small remainder function $\Re(\omega)$, which accounts for the asymmetry: $Y(\omega) = i\omega B/(\omega - \omega_2 + i\gamma_2) + \Re(\omega)$ ($\gamma_2 > 0$). The pole lies in the lower half

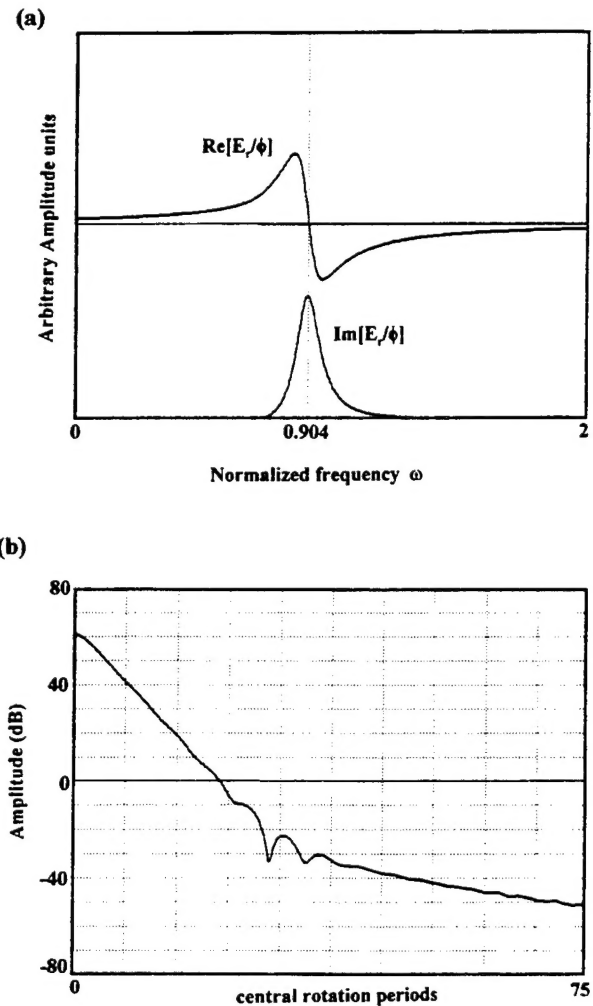


FIG. 4. (a) Real and imaginary parts of $(rE_r/\phi)_{r=b}$ as a function of frequency ω for the $m = 2$. Central angular velocity corresponds to $\omega = 2$, and angular velocity at the wall ($r = b$) corresponds to $\omega = 0.714$ for $m = 2$. The dotted vertical line in the middle corresponds to the theoretical prediction of the $m = 2$ resonant frequency $\omega = 0.904$ for this profile. (b) Semilogarithmic plot of the envelope of inverse Fourier transform of $(rE_r/\phi)_{r=b}$. Initial exponential decay change to an asymptotic algebraic decay with some interference in between.

frequency plane, a location which can only be reached by analytic continuation of our solution of Eq. (1), and is responsible for the early exponential decay (with rate γ_2) seen in Fig. 4(b). The precise way in which $\Re\{Y(\omega)\}$ goes to zero depends upon the way in which the density $n_0(r)$ goes to zero at the plasma edge, and this also determines the form of the algebraic decay in asymptotic limit of the impulse response. The Q of the resonance $\omega_2/2\gamma_2$ and the frequency ω_2 , relative to the central rotation frequency, depends on details of the density profile. Some profiles exhibit a Q close to the experimentally observed value of 84. The form of $Y(\omega)$

is qualitatively similar for the various density profiles and modes that we have studied numerically.

An important feature of the admittance calculation is that the constant B is *negative*, opposite from that expected for passive systems (e.g., a tuned RLC circuit). Neutrally stable (undamped) negative energy modes are destabilized by removal of energy through dissipation. This has been well documented for the $m = 1$ diocotron mode [15]. In our case, the $m = 2$ mode is already damped, though not by dissipation but one might expect that the addition of dissipation would *reduce* the damping rate and perhaps even turn it into a growing mode. Using the admittance function one can show that a resistive or dissipative boundary condition at the outer edge of the plasma *reduces* the growth rate. When a resistor R is placed in parallel with the octupole section, as in Fig. 1(d), the following equation holds: $Y(\omega) + (1/R) = 0$. Using the simple pole approximation and neglecting the small remainder function $\Re(\omega)$ we obtain for mode frequency $\omega \approx \omega_2 - i(\gamma_2 + \omega_2 BR)$. The last term shows that when $B < 0$ there should be a *reduction* in the damping rate of the mode proportional to the resistance R , whereas when $B > 0$ the damping rate is *increased*.

External dissipation is easily added experimentally by connecting resistors to unused segments of the octupole sections. Two precautions are necessary. First, the resistors must be connected so as to affect the $m = 2$ mode but not the $m = 1$ mode, because the latter would be immediately destabilized. This is accomplished connecting the resistor simultaneously to two diametrically opposite segments of an octupole, as shown in Fig. 1(d). Second, the cable capacitance must be "tuned out" by adding a parallel inductor, selected so that parallel resonant frequency is equal to the frequency of the $m = 2$ mode. Experimentally it is found that the connection of an external resistor to the wall electrodes in this fashion causes the damping rate to *decrease* rather than increase and with high enough resistance; the mode is seen to be destabilized. The reduction in decay rate by external dissipation is shown in Fig. 5. Theoretically, since the form of $Y(\omega)$ is similar for higher modes also, one expects similar behavior for the $m = 3$ and higher modes.

In summary, our experimental observations reveal, for the first time, three important characteristics of an $m = 2$ fluid perturbation. First is collisionless damping of small perturbations with evidence for a dominant pole which follows from the observed exponential decay of the linear

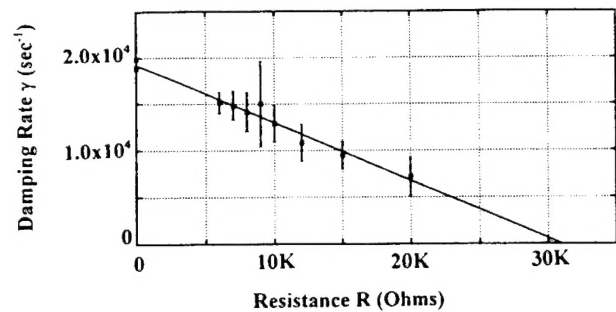


FIG. 5. Decay rate of the $m = 2$ response versus resistance when a resistor is connected to the wall electrode. Line is a least squares fit of the experimental data obtained from a large number of responses.

response. Second is evidence at large amplitudes for fluid trapping by the mode, with a bounce frequency proportional to the square root of the amplitude. Third, the decaying disturbance has negative energy and decays less rapidly when external dissipation is added.

This work was supported by ONR Grant No. N00014-89-J-1264.

- [1] J. W. S. Rayleigh, Proc. London Math. Soc. **11**, 57 (1880).
- [2] W. Thomson, Nature (London) **23**, 45 (1880).
- [3] K. M. Case, Phys. Fluids **3**, 143 (1960).
- [4] R. J. Briggs, J. D. Daugherty, and R. H. Levy, Phys. Fluids **13**, 421 (1970).
- [5] C. F. Driscoll and K. S. Fine, Phys. Fluids B **2**, 1359 (1990).
- [6] A. J. Peurrung and J. Fajans, Phys. Fluids A **5**, 493 (1993).
- [7] T. B. Mitchell, C. F. Driscoll, and K. S. Fine, Phys. Rev. Lett. **71**, 1371 (1993).
- [8] X.-P. Huang and C. F. Driscoll, Phys. Rev. Lett. **72**, 2187 (1994).
- [9] L. Landau, J. Phys. (Moscow) **10**, 25 (1946).
- [10] J. S. deGrassie and J. H. Malmberg, Phys. Rev. Lett. **39**, 1077 (1977); Phys. Fluids **23**, 63 (1980).
- [11] T. M. O'Neil, Phys. Fluids **8**, 2255 (1965).
- [12] J. H. Malmberg and C. B. Wharton, Phys. Rev. Lett. **19**, 775 (1967).
- [13] C. B. Wharton, J. H. Malmberg, and T. M. O'Neil, Phys. Fluids **11**, 1761 (1968).
- [14] R. W. Gould and M. A. LaPointe, Phys. Rev. Lett. **67**, 3685 (1991); R. W. Gould and M. A. LaPointe, Phys. Fluids B **4**, 2038 (1992).
- [15] W. D. White, J. H. Malmberg, and C. F. Driscoll, Phys. Rev. Lett. **49**, 1822 (1982).

DYNAMICS OF NONNEUTRAL PLASMAS

Roy W. Gould

*California Institute of Technology
Pasadena, California 91125*

This paper focuses mainly on the dynamics of two-dimensional cylindrical nonneutral plasma. After reviewing some highlights of the nonneutral plasma dynamics, some recent 2D results are described: vortex dynamics, diocotron instabilities of hollow profiles, collisionless damping of modes and fluid trapping by modes, fluid echos, the cyclotron center of mass modes and warm plasma Bernstein modes, their use for temperature determination. We call attention to some unsolved problems.

JAMES CLERK MAXWELL PRIZE LECTURE
Minneapolis, MN - November 10, 1994
Submitted to Physics of Plasmas

I. INTRODUCTION.

A brief chronology of developments in nonneutral plasmas is shown in Table I. Work on nonneutral plasmas goes back at least to the pioneering paper by Leon Brillouin,¹ in which he first described steady state flows of charged particle beams in a magnetic field, a form of magnetic focussing in which the repulsive space charge electric field E generated by charged particles is balanced by a Lorentz $v \times B$ force of the particles moving through a static magnetic field. He described both planar and cylindrical steady state flows, illustrated in Fig. 1 for the case of electrons. Both were later used for magnetic focusing of electron beams in various types of microwave devices. One of the earliest attempts to understand the dynamics of such beams was by McFarlane and Haye². In attempting to explain the operation the highly successful magnetron device, they studied the behavior of small perturbations in a planar Brillouin beam and showed that they could be unstable. Because of the sheared nature of the flow, the instability was termed the slipping stream instability and also the diocotron instability. However, attempts to give a quantitative theory of the magnetron were not very successful, but Brillouin flow found important applications in beam type microwave devices, such as the traveling wave tube³ (cylindrical beams) and the French M-type backward wave oscillator⁴ (planar beams). In these applications good quantitative theories of the of the beam dynamics, together with their interaction with slow-wave circuits, were possible.⁵ In the case of the M-type backward oscillator, the instability of the thin beam resulted in a reduced start-oscillation current.⁶ In the case of magnetically focused hollow beams, the instability resulted in beam breakup.⁷ However, most microwave device researchers of the time did not think of their beams as plasmas.

The science of plasma physics began to prosper in the 1960s because of the interest in fusion energy, accelerators, and ion sources. Work on nonneutral plasmas accelerated in the 1970s. The cylindrical Brillouin equilibrium was verified over the entire range of rotational velocities.⁸ Charged particles were injected and trapped in magnetic mirror fields.⁹ A variety of configurations were devised and studied, both experimentally and theoretically. Considerable attention was given to the equilibria and their stability.^{10,11} The diocotron instability was further analyzed and the analogy between with 2D incompressible inviscid fluid flow was recognized.^{10,11} An excellent and comprehensive review of this phase of the nonneutral plasma research is found in the two volumes on nonneutral plasmas by Davidson.^{12,13}

Confinement of pure electron and pure ion plasmas using Penning traps became important in the 1970s and developed along two tracks, largely independent at first. Both configurations employ electrostatic fields for axial confinement and are illustrated in Fig. 2.

The Penning trap with hyperbolic electrodes¹⁴ was introduced to contain charged particles for precision spectroscopic measurements. In hyperbolic traps the electrodes are shaped so that the confining potential is proportional to $r^2 - 2z^2$. This makes the orbit of a single particle in the trap particularly simple.¹⁵ In spectroscopic work, plasma effects are undesirable and minimized. There has been very extensive work by the chemists in ion-cyclotron resonance mass spectrometry in traps. Positrons and antiprotons in sizeable numbers are trapped, contained, and transported.^{16,17} The densities in hyperbolic traps can be made sufficiently high that plasma effects become important and very low temperatures have been achieved by laser

cooling.¹⁸ At low temperatures the thermal equilibrium in a quadratic trap potential is a rigidly rotating spheroid of constant density. These states are routinely observed. Dubin¹⁹ has given a theory of the plasma modes of cold spheroidal plasma in the rigid rotor state. These modes are now used as a diagnostic to determine plasma densities, shapes, and temperatures,^{20,21} the latter with an extension of Dubin's theory.

Malmberg and coworkers²² developed the cylindrical Penning trap to study basic plasma phenomena in a relatively idealized situations. Many phenomena have been identified and studied.^{23,24,25,26,27} One of the major developments to come from this line of investigation is the new experimental method for the study of 2D vortex dynamics,²⁴ a subject of longstanding interest in the field of fluid mechanics. A good summary of more recent research on nonneutral plasmas will be found in two A.I.P. Conference Proceedings.^{28,29}

The remainder of this paper deals with 2D phenomena in cylindrical pure electron plasmas and is organized as follows. In Sec. II we summarize the Brillouin equilibrium, the 2D drift-dynamic equations for low frequencies, low densities, and zero temperature. We review their similarity with the Euler equations for 2D inviscid incompressible fluid flow^{10,11,23} and cite a few simple but important results. In Sec. III we discuss the linearized equations for situations in which the density and angular velocity depend on radius (shear-flow) and instabilities when the density and angular velocity profiles are nonmonotonic. In Sec. IV we discuss internal perturbations, collisionless (Landau-like) damping of the response to an applied pulse. These can be understood in terms of phase mixing because of the different angular velocities

with which persistent density perturbations are convected at different radii. Experimental evidence is presented for trapping of the fluid by the wave. In Sec. V we discuss the possibility of echos which arise out of the nonlinear interaction between two applied pulses. In Sec. VI we discuss high frequency (cyclotron) modes where inertial terms and plasma temperature are important. Finally in Sec. VII we enumerate some unsolved problems connected with the above.

II. 2D CYLINDRICAL DYNAMICS AND THE INVISCID FLUID ANALOGY.

The Brillouin steady state for a cold cylindrical nonneutral plasma is one in which the inward magnetic force due to the rotational angular velocity cancels the outward electrostatic repulsive force of the charges and the outward centrifugal force at every radius. When the density $n_0(r)$ is independent of radius, the angular velocity of rotation $\omega_0(r)$ is also independent of radius, the so-called rigid rotor state. The rotation frequency is determined by the force-balance equation

$$\omega_0^2 - \omega_0 \omega_c + \omega_p^2/2 = 0 \quad (1)$$

and the solutions of this equation, which are well known, are depicted in Fig. 3, along with experimental data.⁸ At the maximum density, $\omega_p^2 = \omega_c^2/2$, the Brillouin limit. Most experiments on pure electron plasma, which will be the focus of this paper, are at low density, in the lower left corner of Fig. 3, where $\omega_p^2 \ll \omega_c^2$. Small amplitude 2D perturbations from the rigid rotor steady state are surface waves, traveling around the perimeter $\sim \exp(im\theta - i\omega t)$, as illustrated in Fig. 4. There are discrete low frequency and high frequency surface modes:

$$\omega = [m - 1 + (a/b)^{2m}] \omega_0 \quad (2a)$$

$$\omega = \omega_c + [m - 1 - (a/b)^{2m}] \omega_0 \quad (2b)$$

where a and b are the radii of the plasma and a surrounding metal cylinder, respectively. The $m = 1$ modes are simple center of mass modes and the sum of their frequencies is ω_c . The frequency of the $m = 1$ low frequency mode, $\omega = \omega_0(a/b)^2$, depends only on the mean density within the cylinder. These modes have no z -dependence ($k_z = 0$). With z -dependence $\sim \exp(ikz)$ the modes propagate in the z direction as well. Axially propagating modes have been analyzed^{12,13,30} and they are similar to the Trivelpiece-Gould modes³¹ of a neutral plasma, except that plasma rotation adds a new feature. For $m = 0$, plasma rotation does not matter, and the axially propagating modes have been studied experimentally²².

For low density and low frequencies the inertial terms can be neglected, e.g. the first term in Eq. (1), and the drift approximation can be used, and the electron fluid velocity is given by $\underline{v} = (\underline{E} \times \underline{B}_0)/B_0^2$. For electrostatic disturbances $\underline{E} = -\nabla\phi$ so that 2D fluid flow is incompressible, $\nabla \cdot \underline{v} = 0$. Since $\underline{v} = -\nabla\phi \times \underline{B}_0/B_0^2$, the flow is along equipotentials and ϕ is, aside from a factor $1/B_0$ the stream function. Furthermore the vorticity (z -component) $\nabla \times \underline{v} = \nabla^2\phi$ is, for a pure electron plasma, equal to ne/ϵ_0 . The density is related to the velocity by the continuity equation which, because $\nabla \cdot \underline{v} = 0$, can be written as $\partial n/\partial t + \underline{v} \cdot \nabla n = 0$. This means that the density is simply convected with the flow. The fact that these equations have the same form as the Euler equations for an inviscid ordinary (uncharged) fluid was recognized early in the study of non-neutral plasmas.¹⁰ A comparison of the the two sets of equations is given in Refs. 11 and 24. However it is only in the past half-dozen years that this feature has been exploited experimentally and it

has produced some beautiful experimental results in 2D vortex dynamics,^{24,25} and made contact with a large body of literature in theoretical and computational vortex dynamics in the field of fluid mechanics.

Perhaps one of the most striking examples is the merger of two vortex patches when their initial separation is less than a critical value, about 1.7 times the diameter of the vortex patch. This was a long standing prediction in fluid mechanics but it was first demonstrated experimentally in a definitive manner by Fine et al in a pure electron plasma.²⁶ This work is also an excellent example of the ability to image the line-averaged plasma density (proportional to vorticity) when it is dumped.

III. RADIAL DENSITY PROFILES AND STABILITY.

The instability of the planar beam described in the introduction has a cylindrical analog. It was first demonstrated experimentally in hollow electron beams by Kyle and Webster,⁷ when they showed that as the hollow beam propagates it tends to break up into a number of spiral vortices, the number depending on the thickness of the beam. This is the simplest example of a non-monotonic density profile: constant density between two radii, r_1 and r_2 , and zero for $r < r_1$ and for $r > r_2$. The flow is incompressible and sheared, with the angular velocity of electrons at the outer surface greater than at the inner surface. The stability boundaries for this geometry were determined by Levy.¹⁰ The notion of surface waves, running around the inner and outer surfaces at different velocities is useful. The wave on the outer surface has negative energy and the wave on the inner surface has positive energy. If the beam is not too thick (compared with the azimuthal wavelength) the fields of the positive and negative energy waves overlap and their

velocities are sufficiently close that they are coupled and this allows them both to grow exponentially. It is easy to show that the growth rate depends on the ratio of the beam thickness to azimuthal wavelength and has a maximum,^{6,32} as shown in Fig. 5. In experiments where the instability is initiated by noise, the wavelength with the fastest growth rate should be observed and this decreases with beam thickness. This feature of instability has been nicely demonstrated by Peurrung and Fajans³³ in a cylindrical trap as shown in Fig. 6.

In most pure electron plasmas, the radial density distribution is not uniform, though approximately axi-symmetric. In this case the angular velocity also depends on radius, i.e. the flow is sheared. This significantly increases the complexity and subtlety of the dynamics. The angular velocity becomes a function of radius and is determined by the density through the equation

$$\omega_0(r) = \frac{e}{\epsilon_0 B_0 r^2} \int_0^r n_0(r') r' dr' \quad (3)$$

It is convenient to normalize the density and angular velocity profiles to their central values $\omega_0(r) = \omega_0(0) f(r)$ and $n_0(r) = n_0(0) g(r)$ where

$\omega_0(0) = \omega_p^2(0)/2\omega_c$ is the central rotation frequency. Such profiles are expected to evolve to the rigid rotor steady state but the time to do so in many experiments is too long for this to be achieved. This evolution is sufficiently slow that, for most oscillation and wave phenomena, the profiles can be regarded as steady. Examples of monotonic and nonmonotonic density profiles and the resulting angular velocity profiles which will be discussed in this paper are shown in Fig. 7. The last of these, Fig. 7d, is the hollow beam described briefly above.

For this paper we are interested in the smooth profiles shown in Fig. 7b and Fig. 7c. Linear modes of these profiles have many similarities (and some differences) with longitudinal plasma waves in a Vlasov plasma. In Ref. 11 smooth profiles were examined and it was shown that a necessary condition for instability (existence of a temporally growing eigenmode) of such a system is that $dn_0(r)/dr$ change sign, i.e. that the profile is nonmonotonic, such as in Fig. 7c. This is not a sufficient condition however and specific profiles have to be examined. Fig. 7c depicts (approximately) the profile used in the experiment of Driscoll et al³⁴ which demonstrated that the $m=2$ mode was unstable. In that work, a small seeded $m=2$ perturbation was seen to grow exponentially from the linear regime and to form two vortices (density clumps) which eventually merge, as illustrated in Fig. 8.³⁴ Eventually, the high density annulus ends up in the center and the density profile is, in a coarse grain sense monotonically decreasing.

This situation was also studied³⁴ with a 2D fluid code which solved the nonlinear equations described in Section II on a 256×256 square grid on which the potential at all points outside an inscribed circle, corresponding to the conducting wall, was set to zero. A successive overrelaxation Poisson solver was used and the density was advanced in time using a 15 point Arakawa algorithm. The density at 6 times in the evolution, corresponding to about 20 rotation times of the column is shown in Fig. 9. The first "frame", where the $m=2$ perturbation of the annulus is hardly visible, is in the linear regime. By the third frame the two large vortices have formed and they are beginning to merge in the fourth frame. Two density holes persist near the edge for some time. Recently, Huang has shown that the asymptotic experimental density profile is reasonable well fit by a minimum enstrophy theory rather than a

maximum entropy theory.²⁷

IV. CONTINUUM OF MODES, COLLISIONLESS DAMPING, AND FLUID TRAPPING.

Before describing experimental results on collisionless damping and trapping³⁶ we review the linear behavior of disturbances in stable profiles, following an approach similar to that Ref. 11. We use the usual notation for unperturbed and perturbed quantities, denoting them by subscripts 0 and 1, respectively, and assume angular dependence of $\exp(im\theta)$. The linearized Poisson's equation becomes

$$\frac{d^2\phi_1}{dr^2} + \frac{1}{r} \frac{d\phi_1}{dr} - \frac{m^2}{r^2} \phi_1 = n_1 e / \epsilon_0, \quad (4)$$

and the linearized continuity equation becomes

$$\frac{\partial n_1}{\partial t} + im\omega_0 n_1 - \frac{im}{rB_0} \frac{dn_0}{dr} \phi_1 = 0 \quad (5)$$

where we have used the drift equation $\underline{v}_1 = \underline{B}_0 \times \nabla \phi_1 / B_0^2$, the fact that $v_0 = r\omega_0$ is in the θ direction, and neglected the nonlinear term $\underline{v}_1 \cdot \nabla n_1$. $n_0(r)$ is assumed to be known and $\omega_0(r)$ is determined from it by Eq. (3). One can write the solution of Eq. 4. as

$$\phi_1(r) = -e \int_0^b G_m(r, r') n_1(r') 2\pi r' dr' + \phi_{1\text{ext}} \quad (6)$$

where $G_m(r, r')$ is the Green's function for the problem with $\phi_1(0) = \phi_1(b) = 0$. In Eq. (6) the potential is split into the part produced by the plasma and the externally applied part. $\phi_{1\text{ext}}$ is the potential due to the voltages applied to the conducting wall.

There are two types of problems which one might want to solve: (a) an initial value problem where the initial density $n_1(r, 0)$ is given and one wants

to know how the density, potential, etc evolve subsequently in time or, (b) a situation where a voltage pulse is applied to a segment of the conducting electrode at $t=0$ when the plasma is otherwise undisturbed, and one wants to know how the plasma responds to the pulse. A Laplace transform with respect to time is suitable for either type of problem. In the latter case, $n_1(r,0) = 0$ and Eqs. (4) and (5) become

$$\frac{d^2\Phi_1}{dr^2} + \frac{1}{r} \frac{d\Phi_1}{dr} - \frac{m^2}{r^2} \Phi_1 = N_1 e / \epsilon_0 \quad (7)$$

and

$$(\omega - m\omega_0) N_1 = - \frac{m}{rB_0} \frac{dn_0}{dr} \Phi_1 \quad (8)$$

where $\Phi_1(r,\omega)$ and $N_1(r,\omega)$ are the Laplace transforms of the potential and density. We use for the Laplace variable $s = i\omega$ with ω in the upper half plane. Eliminating N_1 gives

$$\frac{d^2\Phi_1}{dr^2} + \frac{1}{r} \frac{d\Phi_1}{dr} - \frac{m^2}{r^2} \Phi_1 + \frac{em}{rB_0\epsilon_0} \frac{dn_0/dr}{(\omega - m\omega_0)} \Phi_1 = 0 \quad (9)$$

This equation has been extensively studied. Briggs et al¹¹ were the first to give a general discussion of the analytic properties of Φ_1 in the complex ω plane and to note the similarity of this situation with that of Landau damping of longitudinal plasma waves. $\Phi_1(r,\omega)$ and $N_1(r,\omega)$ are defined in the upper half ω plane and as the real ω axis is approached from above, the denominator of Eq. (9) becomes singular if the real part of ω lies in the range

$$m\omega_{0min} < \text{Re}\{\omega\} < m\omega_{0max}, \quad (10)$$

where ω_{0min} and ω_{0max} are the minimum and maximum rotation frequencies in the plasma. This gives rise to a branch line along the real frequency axis between these limits as shown in Fig. 10a. The potential function can be

analytically continued into the lower half plane as discussed in Ref. 11, leading to the deformed contour of Fig. 10b.

As with Langmuir waves, one can show that Eq. (9) has a continuum of singular eigenmodes (generalized functions) in the frequency range, similar to the Van Kampen-Case modes^{37,38} for Langmuir oscillations. This leads to two different views, or descriptions, of collisionless damping which are equally valid. Although the diocotron mode problem is similar in many ways to the Landau problem, it is different in two significant ways: the frequency range is limited by Eq. (10) and each (angular) velocity is associated with a *different radius*.

For comparison with experiment³⁶ we are primarily interested in the response of the plasma to an applied pulse. We need solutions of Eq. (9) in which $\Phi_1(b, \omega)$, the Laplace transform of the potential at the conducting wall is the applied potential. Φ_1 must vary as r^m near the origin. To compare with experiment we need the radial electric field at $r=b$ from which the current flowing to the wall can be obtained. For a parabolic density, $f(r) = 1 - (r/a)^2$, Corngold⁴⁰ has shown that the solution of Eq. (9) can be expressed in terms of the hypergeometric function and the location of the pole illustrated in Fig. 10b can be determined analytically.

We are interested in more general profiles, $n_0(r)$ and $\omega_0(r)$, where solutions are not necessarily expressible in terms of known functions. Our approach is to numerically integrate Eq. (9) for a specific density profile and for a discrete set of equally spaced frequencies ω_k along the contour shown slightly above the real frequency axis in Fig. 10a. We obtain the temporal response (wall current) from an inverse Discrete Fourier Transform

(DFT) of $-i\omega\epsilon_0 \left| \frac{\partial \Phi_1(r, \omega_k)}{\partial r} \right|_{r=b}$. To compare with experimental measurements the admittance function³⁶ is defined by

$$Y(\omega) = +i\omega 2\pi\epsilon_0 F_1 F_2 \left| r \left[\frac{\partial \Phi_1(r, \omega)}{\partial r} \right] / \Phi_1(r, \omega) \right|_{r=b}, \quad (11)$$

where F_1 and F_2 are sector form factors. The admittance function is the Fourier transform of the response to current in sector 2 due to an impulse applied to sector 1. For smoothness of this function, there is a requirement that the ratio of the step size in the radial integration and the step size in frequency satisfy the inequality $\Delta r \ll \Delta\omega / (d\omega_0/dr)$. Evaluation of the function $Y(\omega)$ at frequencies at a distance σ slightly above the real frequency axis, followed by taking its inverse with a DFT which assumes ω to be real, gives rise to an additional exponential damping factor, $e^{-\sigma t}$ which can easily be corrected for. The real and imaginary parts of the the principal factor in the admittance function, $(r[\partial\Phi_1/\partial r]/\Phi_1)_{r=b}$, are shown for a typical monotonic density profile and for $m=2$ in Fig. 11. Also shown in Fig. 11 is the $m = 2$ impulse response obtained from the inverse DFT of $Y(\omega)$. The admittance has a nonzero real part only in the the frequency range described by Eq. (10) when there is a resonance in the denominator of Eq. (9). The admittance function is defined so that $\text{Re}\{Y\} > 0$ corresponds to absorbtion. Since we find that $\text{Re}\{Y\} < 0$ in this range, energy is *released* when a disturbance is excited, so the system is a negative energy system.

The real and imaginary parts of rE_r/Φ shown in Fig. 11 can be approximated by a simple pole below the real frequency axis plus a small remainder function

$$Y(\omega) = \frac{A}{-i(\omega - \omega_2 + i\gamma_2)} + \Re(\omega) \quad (12)$$

where A is negative because of the negative energy property. Eq. (12) is

consistent with Fig. 10b, which shows a simple pole below the real frequency axis. $\Re(\omega)$ comes from integrals along the branch cuts. The exponential decay which dominates the early time behavior is associated with the pole and the algebraic decay which appears later is associated with $\Re(\omega)$. While the precise details of $Y(\omega)$, and thus of the impulse response, are profile dependent, the general features are the same for qualitatively similar profiles. The frequency ω_2 corresponds to twice ($m=2$) the rotational angular velocity at a radius near the outer limit of the plasma ($\sim 0.8a$).

Collisionless damping of the $m = 2$ mode in the linear regime has recently been observed by Pillai³⁶ using the experimental apparatus depicted in Fig. 12. The *envelope* of the decaying sine wave, which is excited by a 5 μ sec sinusoidal burst (about 3 cycles), is shown in Fig. 13 for various amplitudes of the burst. Each trace is the average of 20 "identical" traces and an example of the actual sinusoidal signal is shown in the inset. The lowest three traces are essentially in the linear regime. As the amplitude of the excitation is increased, "bounce" oscillation begin to appear, indicating trapping of the fluid near the resonant layer. An analysis of the bounce frequency, when corrected for decay of the wave amplitude, shows that it is proportional to the square root of the applied voltage. Trapping in fluids in shear flow was anticipated by Kelvin with his "cats-eyes" describing fluid trajectories. In Ref. 11 it was predicted the "bounce" or trapping frequency should be given by

$$\omega_b \approx m \sqrt{|\Phi_1 \omega'_0(r)/r|}_{r_s} \quad (12)$$

Pillai³⁶ observes that the bounce frequency is proportional to the applied potential to the power 0.55 ± 0.10 using 22 data sets. Using the 2D fluid

code described earlier, both collisionless damping and amplitude modulation of the decaying wave due to trapped particles have been verified⁴¹. Fig. 14. shows a calculation using this fluid code of the charge induced on one octant of the conducting cylinder when a three cycle sinusoidal burst is applied. The linear decay rate agrees well with that obtained by numerical solution of the linear differential equation and the bounce frequency is proportional to the square root of the amplitude. deGrassie²³ first looked for linear collisionless damping, but his detection sensitivity did not allow him to study the linear regime. Instead he found a much slower decay whose rate decreased with increasing amplitude, much like the late time behavior in Fig. 13. He also failed to see the bounce motion.

The negative energy feature of the perturbations has an interesting consequence. When energy is removed from the system, by external resistors for example, the amplitude should grow. This was previously established for the $m=1$ center of mass mode by White, Malmberg, and Driscoll⁴². For $m > 1$, however the modes are already damped by the collisionless phase mixing just described. When external resistors are added in the $m=2$ case as shown in Fig. 12c, the collisionless damping rate is *decreased*. Fig. 15 shows the damping rate versus resistance. Furthermore, with sufficient external dissipation the otherwise damped mode is turned in to a growing mode.

We have seen, by examining the electric field at the conducting wall, that the linear response to a short applied pulse is a decaying sinusoid, approximately exponential. However, density perturbations at each radius within the plasma persist, indefinitely in the ideal drift approximation. This can be seen by inverting Eq. 8

$$n_1(r,t) = \frac{m}{rB_0} \frac{dn_0}{dr} \int \frac{\Phi_1(r,\omega)}{[\omega - m\omega_0(r)]} e^{-i\omega t} \frac{d\omega}{2\pi} \quad (13)$$

which, because of the simple pole at $\omega = m\omega_0(r)$ gives an undamped contribution to $n_1(r,t)$ proportional to $\exp[-im\omega_0(r)t]$. Thus, perturbations at each radius continue to be convected, undamped, at the local angular velocity. The density $N_1(r,\omega)$ and $n_1(r,t)$, calculated by the numerical methods described above, is shown for several representative radii in Fig. 16. It is seen that $n_1(r,t)$ does not decay (lower panel) but has different frequencies (upper panel) at different radii. However, the electric field at the conductor (and therefore the charge on the conductor) decays away because it is caused by (a weighted average of) charge density perturbations at various radii. This result is expressed mathematically as the derivative with respect to r of the *integral* in Eq. 6. Because of the radially dependent phase factor in the integrand, contributions from different radii have different frequencies and phase mix away. The initial and phase mixed density perturbations are illustrated in Figs. 15a and 15b, respectively.

V. FLUID ECHOS

The dynamics of the ideal fluid is time reversible and one suspects by analogy with the cyclotron echos⁴³ and plasma wave echos⁴⁴ that this system might also exhibit echos. The application of a second pulse might partially unmix the undamped phase-mixed remnants of the first pulse and create a coherent response at a later time, long after the responses of both pulses have decayed away. The mixing occurs because of different *angular* velocities so, by analogy with the plasma wave echo, we examine the effects of two pulse applied to the electrode structure shown in Fig. 12. The connections are arranged so as to produce potentials with different angular dependences: m_1

for the first pulse and m_2 for the second pulse. For simplicity we take the time dependence of the applied pulse to be $V_1 t_1 \delta(t)$ and $V_2 t_2 \delta(t-\tau)$ respectively. This form serves as the Green's function (in time) for other pulse shapes. We use the following notation:

$$\phi = \phi_0(r) + \phi_1(r, t) + \phi_2(r, t) + \phi_3(r, t) \quad (14a)$$

$$n = n_0(r) + n_1(r, t) + n_2(r, t) + n_3(r, t) \quad (14b)$$

where the subscript 0 refers to the steady state, subscripts 1 and 2 refer to the first and second applied pulses, and subscript 3 refers to the echo, which results from the nonlinear interaction between pulses 1 and 2.

We treat the first and second pulses in the linear approximation (as described above), and seek the nonlinear interaction between the two pulse to obtain the echo response to *second* order in the amplitudes. To this order the continuity equation for the echo may be written

$$\frac{\partial n_3}{\partial t} + \omega_0 \frac{\partial n_3}{\partial \theta} + v_{3r} \frac{dn_0}{dr} = v_{2r} \frac{\partial n_1}{\partial r} + \frac{v_{2\theta}}{r} \frac{\partial n_1}{\partial \theta} + v_{1r} \frac{\partial n_2}{\partial r} + \frac{v_{1\theta}}{r} \frac{\partial n_2}{\partial \theta} \quad (15)$$

where the nonlinear terms arising out of the interaction of the pulses 1 and 2 have been put on the right hand side. These terms, which we denote by $s_3(r, t)$, act as *source* terms for the echo and are obtained from the linear solutions for pulses 1 and 2. The left hand side is the usual linearized continuity equation.

Since we are using complex exponentials to describe quantities which are real and, by convention, taking the real part (or adding the complex conjugate and dividing by 2), some care is required with the quadratic source term. It is readily shown that when using complex notation one should use the complex conjugate of the complex solution for one of the pulses and divide by 2. We chose to do this for pulse 1, so that the echo has angular mode number

$m_3 = m_2 - m_1 > 0$, where m_1 and m_2 are positive. Since the source term $s_3(r,t)$ consists of *products* of time-dependent quantities, the Laplace transform of s_3 is given by the *convolution* of the transforms of the individual quantities. Of the four terms in s_3 , the first dominates because $n_1(r,t)$ contains terms $\sim \exp[-i\omega_0(r)t]$, unlike $v_1(r,t)$. Because it is differentiated with respect to r , it contains terms which grow with t . In transform space the source term has the form

$$S_3(r,\omega) \approx -\frac{im_2}{rB_0} \int \Phi_2(r,\omega-\omega') \frac{dN_1(r,\omega')}{dr} \frac{d\omega'}{2\pi} \quad (16)$$

in the dominant term approximation.

We now describe the method of solution. Eqs. (7) and (8) must be solved, for a specified density profile, to obtain $\Phi_1(r,\omega)$, $N_1(r,\omega)$, $\Phi_2(r,\omega)$, and $N_2(r,\omega)$ for pulses 1 and 2. Analytic solutions can only be obtained for special profiles so we resort to numerical methods and consider discrete values of r and ω , $r_j = j \Delta r$, $\omega_k = k \Delta \omega + i\sigma$. In particular we use 512 or 1024 discrete values of ω so as to use DFTs to obtain the time functions. For each of the discrete values of ω , we numerically integrate Eqs. (7) and (8) from $r=0$ to $r=a$ using a fourth order Runge-Kutta method so as to obtain values of the functions at 500 radial points within the plasma. Since we also need $\partial N_1(r,\omega)/\partial r$ it is also calculated during the numerical integration at the 500 radial points. The potentials so obtained must vary as $(r)^{m_1}$ and $(r)^{m_2}$ near the origin and match the Laplace transforms of the applied potentials at the cylinder, respectively. The convolution, Eq. (16), is then done numerically to obtain $S_3(r_j,\omega_k)$. The equations for the echo pulse are similar to those of pulses 1 and 2, except that instead of being driven by potentials applied to the conducting cylinder, the source term is S_3 :

$$\frac{d^2\Phi_3}{dr^2} + \frac{1}{r} \frac{d\Phi_1}{dr} - \frac{m^2}{r^2} \Phi_3 = N_3 e / \epsilon_0 \quad (17)$$

$$(\omega - m_3 \omega_0) N_3 = - \frac{m_3}{r B_0} \frac{dn_0}{dr} \Phi_3 + i S_3 \quad (18)$$

These are also integrated numerically in radius for 512 discrete frequencies and inverted with an DFT to obtain the time dependence. Fig. 18 shows the response to pulses 1 and 2 as well as the echo for a typical profile. Here $m_1=2$, $m_2=4$, and $m_3=2$. In each case the time dependent electric field at the wall is shown. The echo amplitude is proportional to the product of the amplitudes of pulses 1 and 2, $V_1 t_1 V_2 t_2$, is generally much smaller than the responses to the two pulses. It is not shown to scale in Fig. 18.

The echo amplitude is expected to be diminished by viscous effects as the time between the first pulse and the echo lengthens. This is because perturbations at nearby radii have been convected by substantially different amounts in azimuth causing the radial gradients become very large. Thus the echo phenomenon may form the basis for studying viscous effects. However, the particles primarily responsible for the echo are restricted to the outer radii of the plasma, so that is probably the only region which could be probed.

VI. HIGH FREQUENCY MODES.

So far the discussion has been limited to low frequencies where the drift approximation is valid. 2D modes near the cyclotron frequency also exist whose frequency is given by Eq. 2b for uniform density (rigid rotor steady state). The $m=1$ center of mass mode lies *below* the cyclotron frequency by the diocotron frequency, and the higher modes are up shifted by the rotation of the plasma. In this section we again focus on nonuniform density and angular velocity profiles such as shown in Fig. 7b. Inertial terms can no longer be

neglected, and expressions for the fluid velocity in a nonuniformly rotating fluid become much more complicated.

An analysis of the high frequency behavior⁴⁵, near the cyclotron frequency, of a cold nonuniformly rotating pure electron plasma has been carried out. The mode structure and the admittance function $Y(\omega)$, as defined in Sec. IV, has been evaluated for a number of stable monotonic profiles. The results are not unlike those for the low frequency diocotron modes described in Sec. IV. For $m=1$ there is a single discrete mode lying slightly below the cyclotron frequency

$$\omega = \omega_c - \langle \omega_p^2 \rangle / 2\omega_c . \quad (19)$$

For each m greater than 1 there is an *absorbition* band

$$(m-1)\omega_0(a) < (\omega - \omega_c) < (m-1)\omega_0(0) , \quad (20)$$

upshifted from the cyclotron frequency by the Doppler effect of rotation. As with the low frequency modes, an alternative point of view is that the absorbition band is associated with continuum of singular normal modes. A typical result for the cold plasma admittance function is shown in Fig. 19. These are positive energy modes as demonstrated later.

Experimentally, the $m=1$ discrete mode is found, as expected, below the cyclotron frequency, but the $m>1$ absorbition bands are not found.⁴⁶ Instead, in the parameter range where the absorption bands are expected from the cold plasma theory, a set of discrete modes for each m greater than 1 is found. Fig. 20 shows a two dimensional scan in density (horizontal axis) and magnetic field (vertical axis). The modes for $m>1$ have been interpreted as radially trapped (by the density and angular velocity profiles) azimuthally propagating Bernstein modes.⁴⁷ Bernstein modes arise out of finite

temperature (finite Larmor radius) effects, which were not included in the cold plasma rotating fluid analysis. However an *approximate* modification of the theory which includes electron temperature has been given,^{45,46} and the temperature required to match the experimental observations is consistent with other determinations of plasma temperature (0.5 - 2.0 eV).

For $m > 1$ the effect of plasma temperature is to turn the continuous absorption band described by Eq. (10) into a band in which Bernstein modes can propagate. This is similar, in a general way, to the effect of temperature on the modes of a *neutral* plasma column: Tonks-Dattner modes,⁴⁸ which are propagating Langmuir oscillations trapped by the radial density profile. Similarly, in a magnetized neutral plasma the Buchsbaum-Hasegawa modes⁴⁹ near the 2nd harmonic of the cyclotron frequency arise from Bernstein waves which are trapped because of the radial density gradient. In both cases the inclusion of temperature raises the order of the differential equation and results in additional "thermal" modes in the region where there would otherwise be a continuum of singular eigenmodes.

In the remainder of this section we concentrate on the $m=1$ center of mass mode whose frequency is just below the cyclotron frequency. We describe a measurement of spontaneous thermal excitation of this mode and a method for using this measurement to determine electron temperature. The method consists of measuring the noise power delivered to a low noise receiver caused by the fluctuating currents, associated with thermal excitation of the $m=1$ mode, which are induced on the sector electrodes surrounding the plasma. The received power is compared with the power from a calibrated reference noise source, and the ratio of the powers is denoted by ρ . The absorption coefficient, A , is also required to determine the temperature. This

procedure results in nondestructive method of temperature determination for pure electron plasmas. In related measurements, spontaneous emission associated with the $m>1$ Bernstein modes has also been observed and the inferred temperatures are in the same range, although these measurements are subject to greater shot-to-shot irreproducibility. Our method is a variation on the method used by Stenzel⁵⁰ for neutral afterglow plasmas and is related to the stored ion calorimeter discussed by Wineland⁵¹. These situations differ drastically from the usual radiation transport regime in astrophysics and in fusion devices where radiation is emitted and absorbed over many wavelengths. This radiation also differs markedly from Larmor radiation from a collection of independent single particles, since we are dealing with a single collective mode of the plasma.

A schematic diagram of the experimental configuration is shown in Fig. 21. To increase the sensitivity to the noise fluctuations the signals from all eight sectors of an octupole section are combined, with phasing so as to be sensitive to the $m=1$ mode, and sent to a low noise ($NF \approx 3\text{db}$) 140 MHz receiver whose bandwidth is 12 kHz. The cyclotron frequency is set slightly above the receiver frequency so that, as the plasma density decays, the $m=1$ mode frequency *sweeps upward through* the receiver frequency. By stepping the magnetic field, and thus the cyclotron frequency, by a small amount on successive shots, the $m=1$ mode resonance can be made to sweep through the receiver frequency at various times in the plasma decay. Emission and absorption measurements (using the r.f. generator) are made on alternate shots. This is illustrated in Fig. 22, which shows both the noise emission and the reflected power (inverted trace) as a function of time for 3 representative different values of the magnetic field. At the beginning and end of an

emission trace, the receiver is switched briefly to reference noise source at temperature, T_{ref} . All elements of the system are 50 ohm coaxial components and the insertion loss of all elements must be accounted for.

Typical experimental results: emission, absorption, and radiation temperature, are shown in Figs. 23a-c. These are obtained by fitting Lorentzian curves to the type of data shown in Fig. 22 and using the maximum values. The results from about 20 shots for the same parameters are averaged to obtain more precise values. Fig. 23a shows the absorption coefficient, A , the fraction of the power absorbed by the plasma when the r.f. signal generator is on. Since the errors in the absorption data are small a polynomial fit is shown and it is used in determining the temperature. Note also that A is close to unity! Fig. 23b shows the noise power received from the plasma, relative to that from the calibrated noise source, ρ . The radiation temperature of the plasma shown in Fig. 23c is then determined from the relationship $T_{\text{rad}} = (\rho/A) T_{\text{ref}}$. The temperature is 0.5 - 0.6 eV and changes only slightly over 400 msec; whereas the plasma density decays by nearly a factor of 10 during this time. The near constancy of the temperature has been observed on most measurements, although the value of the temperature varied between 0.5 and 3.0 eV with different injection conditions. These temperatures are typical of those obtained by other methods.

Because the cylinder radius (2.5cm) is small compared to the free space wavelength (215cm) of the radiation, these results can be interpreted in terms of the electric circuit model shown in Fig. 24. If the plasma is at temperature T , the power emitted per unit bandwidth into the load R_0 (50 Ω) is κTA , where κ is Boltzmann's constant and A is the absorption coefficient. The latter is obtained from the equivalent circuit as $A = 4R_0 R / |R_0 + Z(\omega)|^2$,

where the impedance function, $Z(\omega) = 1/Y(\omega)$, is the inverse of the admittance function.

One of the surprising results is that the $m = 1$ mode absorbs energy since it is expected, from elementary considerations, to be lossless. Furthermore, as illustrated in Fig. 23a, the absorption coefficient changes only slightly while the density decays by nearly an order of magnitude. It is possible to obtain the frequency shift and linewidth versus time of the $m=1$ mode from the Lorentzian fits to the data of Fig. 22. These are shown in Fig. 25. The linewidth is 10-40 kHz, a significant fraction of the frequency shift, 30-180 kHz. Furthermore the linewidth tracks the density decay. The frequency width of the mode is found from $\Delta\omega = (d\omega_1/dt)\Delta t$, where Δt is the time to sweep through the mode as determined from Fig. 22 and $d\omega_1/dt$ is the rate of change of the $m=1$ mode frequency. Since the absorption coefficient A is about unity, the plasma is matched to the 50Ω system, and therefore half the linewidth is due to the external system and the remaining half is *intrinsic* to the plasma.

An independent determination of the line width of the $m=1$ cyclotron mode has been made by measuring its decay rate when excited by a short burst at the mode frequency. By adding 50Ω resistors to various numbers (N) of the octupole sectors, their effect on damping rate can be found. This is the high frequency analog of the $m=1$ and $m=2$ low frequency resistor experiments,^{36,42} except that here the external dissipation *increases* the damping, indicating that the mode is a positive energy mode. The result is shown in Fig. 26 and shows clearly that the damping rate increases linearly with N . The minimum value of N is 2, from the source and the receiver, giving a decay time of about 50 μ sec. To determine the *intrinsic* ($N=0$) damping rate of the mode we

plot the damping rate versus N and determine the intercept corresponding to $N=0$. This result is shown in Fig. 27 for several different densities. The most important conclusions are that the intrinsic damping rate is non-zero and that, for low densities, the intrinsic damping rate increases with density. The latter is consistent with A being approximately independent of density.

VII. DISCUSSION.

Experimental results presented above suggest some unresolved issues which may lead to a still better understanding of the phenomena.

For $m=1$ the cold plasma equations for a nonneutral plasma predict two discrete undamped center of mass modes. The low frequency mode is observed to be undamped²³ or weakly damped⁵²; whereas, the high frequency mode is strongly damped. This origin of this damping is as yet unexplained.

For $m>1$, the cold plasma equations predict absorption bands (continuum of singular eigenmodes) for *both* the low frequencies, $\omega \sim \omega_0$, and high frequencies, $\omega \sim \omega_c$. However, experimentally, radially trapped Bernstein modes are found in the frequency band in which the high frequency absorption band is supposed to appear. These require temperature or finite Larmor radius (FLR) effects. However, temperature and FLR effects *appear* to be unimportant for the the low frequency modes. Why?

For the collisionless damping of low frequency disturbances in sheared flows, such as those described in Sec. VI, what is the role and importance of viscosity. One normally thinks of viscosity as a dissipative phenomenon and we have seen that external dissipation *reduces* the collisionless damping rate. Does viscosity have the same effect?

Approximate solutions of the Vlasov equation in *sheared* flow, such as

those presented by Pearson⁵³ for neutral cylindrical plasmas and by Prasad et al⁵⁴ for a nonneutral slab plasma, are needed for both the high frequency and low frequency regimes. In order to carry out such analyses it is necessary to find slowly evolving self-consistent *sheared* profiles from which to start.

Plasma temperature appears to decay much more slowly than plasma density in pure electron plasmas. This observation needs an explanation. Release of energy through expansion of the plasma as the density decays probably plays a role in determining the temperature.

ACKNOWLEDGEMENTS. I gratefully acknowledge the vital contributions of Sateesh Pillai and Michael A. LaPointe to the results described in Secs. IV and VI, respectively, and the Office of Naval Research for its support of research reported here. I am also deeply grateful to the late John H. Malmberg and Thomas M. O'Neil for rekindling my interest in this subject and, together with Fred Driscoll, for freely sharing their insights and expertise.

REFERENCES

1. L. Brillouin, Phys. Rev. 67, 260 (1945).
2. G. G. McFarlane and H. G. Haye, Proc. Phys. Soc. 63, 409 (1953).
3. W. W. Rigrod and J. A. Louis, Bell System Tech. J. 33, 399 (1954).
4. R. R. Warnecke, P. Guenard, O. Doehler, and B. Epsztein, Proc. Inst. Radio Eng. 43, 413 (1955).
5. R. G. E. Hutter, *Beam and Wave Electronics in Microwave Tubes*, D. Van Nostrand (1960), see chapters 10 and 11.
6. R. W. Gould, Jour. Appl. Phys. 28, 599 (1957); R. W. Gould, Ph.D. thesis, California Institute of Technology, Pasadena California (1956).
7. H. F. Webster, J. Appl. Phys. 26, 1386 (1955); R. L. Kyle and H. F. Webster, I.R.E. Trans. El. Dev. 3, 172 (1956).
8. A. J. Theiss, R. A. Mahaffey, and A. W. Trivelpiece, Phys. Rev. Lett. 35, 1436 (1975).
9. R. E. Pechacek, C. A. Kapetanakis, and A. W. Trivelpiece, Phys. Rev. Lett. 21, 1436 (1968); Phys. Fluids 14, 1555 (1971)
10. R. H. Levy, Phys. Fluids, 8 1288 (1965)
11. R. J. Briggs, J. D. Daugherty, and R. H. Levy, Phys. Fluids 13 421 (1970)
12. R. C. Davidson, *Theory of Nonneutral Plasmas*, W. A. Benjamin, Inc. Reading, Mass. (1974).
13. R. C. Davidson, *Physics of Nonneutral Plasmas*, Addison-Wesley Co. (1990).
14. H. Dehmelt and Walls, Phys. Rev. Lett. 21 127 (1968)
H. Dehmelt, Adv. in Atomic and Molecular Phys. 3, 53 (1967)
G. Graff, Z. fur Naturforschung, 22a 1960 (1967).

- J. Byrne, Proc. Roy. Soc. (London) 86, 801 (1965)
15. L. S. Brown and G. Gabrielse, Rev. Mod. Phys. 58, 233 (1986).
16. R. G. Greaves, M. D. Tinkle, and C. M. Surko, Phys. Plasmas 1, 1439 (1994).
17. G. Gabrielse, Sci. Am. 267, 78 (1992).
18. J. J. Bollinger, D. J. Wineland, and D. H. E. Dubin, Phys. of Plasmas 1 1403 (1994).
19. D. H. E. Dubin, Phys. Rev. Lett. 66, 2076 (1991).
20. M. D. Tinkle, R. G. Greaves, C. M. Surko, R. L. Spenser, and G. W. Mason, Phys. Rev. Lett. 72, 352 (1994)
21. C. S. Weimer, J. J. Bollinger, F. L. Moore, and D. J. Wineland, Phys. Rev. A 49, 3842 (1994)
22. J. H. Malmberg and J. S. deGrassie, Phys. Rev. Lett. 35, 577 (1975)
23. J. S. deGrassie and J. H. Malmberg, Phys. Fluids, 23, 63 (1980)
24. C. F. Driscoll and K. S. Fine, Phys. Fluids, B 2, 1359 (1990)
25. A. W. Hyatt, C. F. Driscoll, and J. H. Malmberg, Phys. Rev. Lett. 59, 2975 (1987), see also B. R. Beck, J. Fajans, and J. H. Malmberg, Phys. Rev. Lett. 68, 317 (1992).
26. K. S. Fine, C. F. Driscoll, J. H. Malmberg, and T. B. Mitchell, Phys. Rev. Lett. 67, 588 (1991).
27. X.-P. Huang and C. F. Driscoll, Phys. Rev. Lett. 72, 2187 (1994).
28. C. W. Roberson and C. F. Driscoll (editors), *Non-neutral Plasma Physics*, Am. Inst. Phys. Conf. Proc. #175 (1988).
29. D. H. E. Dubin and J. Fajans (editors), *Non-neutral Plasma Physics*, Am. Inst. Phys. Conf. Proc., in preparation.
30. S. A. Prasad and T. M. O'Neill, Phys. Fluids 27, 206 (1984).

31. A. W. Trivelpiece and R. W. Gould, Jour. App. Phys. 30, 1784 (1959);
A. W. Trivelpiece, "Slow-Wave Propagation in Plasma Waveguides", San Francisco Press, Inc. San Francisco (1967).
32. R. W. Gould, in Chap. 11 of Ref. 5.
33. A. J. Peurrung and J. Fajans, Phys. Fluids A 5, 493 (1993).
34. C. F. Driscoll, J. H. Malmberg, K. S. Fine, R. A. Smith, X.-P. Huang,
and R. W. Gould, in Plasma Physics and Controlled Nuclear Fusion Research
1988, Vol. 3, Vienna: IAEA, 507 (1989).
35. A. Arakawa, Jour. Comp. Phys. 1 119 (1966).
36. S. Pillai and R. W. Gould, Phys. Rev. Lett. 73 2849 (1994).
37. N. G. Van Kampen, Physica, 21, 949 (1955).
38. K. M. Case, Annals of Phys. 7, 349 (1959).
39. L. D. Landau, J. Phys. (USSR) 10 25 (1946)
40. N. Corngold, Phys. of Plasmas, submitted.
41. D. Bachman and R. W. Gould, Bull. A.P.S. 39 1738 (1994).
42. W. D. White, J. H. Malmberg, and C. F. Driscoll, Phys. Rev. Lett. 49,
1822 (1982).
43. R. W. Gould, Am. Jour. Phys. 37, 585 (1969).
44. R. W. Gould, T. M. O'Neil, and J. H. Malmberg, Phys. Rev. Lett. 19, 219
(1967).
45. R. W. Gould, Phys. of Plasmas, submitted.
46. R. W. Gould and M. A. LaPointe, Phys. Rev. Lett. 67, 3685 (1991);
Phys. Fluids B, 4, 2038 (1992).
47. I. B. Bernstein, Phys. Rev. 109, 10, (1958).
48. J. V. Parker, J. C. Nickel, and R. W. Gould, Phys. Rev. Lett. 11, 183
(1963); Phys. Fluids 7, 1489 (1964).

49. S. J. Buchsbaum and A. Hasegawa, Phys. Rev. Lett. 12, 685 (1964); Phys. Rev. 143, 303 (1966).
50. R. L. Stenzel and R. W. Gould, Phys. Rev. Sci. Inst. 40 1461, (1969).
51. D. J. Wineland and H. G. Dehmelt, Jour. Appl. Phys. 46, 919 (1975).
52. B. Cluggish and C. F. Driscoll, Bull. A.P.S. 38, 1736 (1994)
53. G. A. Pearson, Phys. Fluids 9, 2454, 2464 (1966).
54. S. A. Prasad, G. J. Morales, and B. D. Fried, Phys. Fluids 30, 3093 (1987).

FIGURE CAPTIONS

Table I. Advances in Nonneutral Plasmas

- Fig. 1. Brillouin Flow. a. cylindrical, b. planar. b. is shown with a slow-wave circuit as used in Backward Wave Oscillators.
- Fig. 2. Penning traps. a. cylindrical and b. hyperbolic. Radial containment is by the axial magnetic field and axial containment is electrostatic.
- Fig. 3. Rotation Frequency versus plasma density in Brillouin Equilibrium. Experimental points are from Ref. 8.
- Fig. 4. Surface modes of a cylindrical nonneutral plasma with constant density.
- Fig. 5. Growth rate versus thickness for planar Brillouin beam.
- Fig. 6. Images of unstable hollow plasmas showing azimuthal wavelength for three thicknesses (0.67, 0.17, and 0.14 cm). Left side: before instability, Right side: after onset. From Ref. 33.
- Fig. 7. Density profiles and corresponding angular velocity profiles, monotonically decreasing and stable (upper), and hollow profiles which are unstable (lower).
- Fig. 8. Measured z-averaged density $n(r, \theta)$ at $t = 50, 120, 170$, and $1000 \mu\text{sec}$, as $m=2$ hollow profile instability grows, saturates, and evolves to a stable monotonic profile. From Ref. 34.
- Fig. 9. Fluid code calculation of $n(r, \theta, t)$ at 6 successive times in the evolution (upper left to lower right) of the $m=2$ hollow profile instability. Density scale is shown at the right.
- Fig. 10. a. Bromwich contour in complex ω plane used in inverting the Laplace

transform. b. Deformed contour revealing simple pole in the lower half plane.

Fig. 11. (a) Real and Imaginary Parts of $(rE_r/\phi)_{r=b}$ as a function of frequency normalized to the central rotation frequency, for $m=2$. The vertical dotted line corresponds to the $m=2$ resonant frequency $\omega = .904$ for this profile. (b) Semilog plot of the envelope of inverse Fourier transform of $(rE_r/r\phi)_{r=b}$. The initial decay changes from exponential to algebraic. From Ref. 36.

Fig. 12. (a) Schematic of cylindrical structure for plasma excitation and trapping, (b) phasing of first octupole for exciting an $m=2$ disturbance, (c) configuration of second octupole for signal reception, and (d) configuration of second octupole for negative energy test. From Ref. 36.

Fig. 13. Decay of the envelope of $m=2$ signal at about 400 KHz excited by and r.f. pulse with voltages 10 (lower left), 20, 40, 60, 80, 120, 160, 200, 250, 300, 400, 500, 600, 700, and 1000 (uppermost) mV, plotted on a semi-log scale with vertical scale. From Ref. 36.

Fig. 14. 2D Fluid Code Calculation of Damping and Trapping. Plotted is the charge induced on one octant of the cylinder, and in each successive trace the excitation amplitude is doubled.

Fig. 15. Decrease in Decay Rate of the $m=2$ response versus resistance when a resistance R is connected to the wall electrode. The line is a least squares fit to the experimental data. From Ref. 36.

Fig. 16. Density perturbations at $(r/a) = 0.93, 0.87, 0.81, 0.75, 0.69,$ and 0.63 (traces a-e). Upper figure is magnitude of Laplace transform of the density along the contour in Fig. 10a and the lower figure is

a semilog plot of density versus time.

Fig. 17. Internal $m=2$ perturbation of cylindrical nonneutral plasma. (a)

Density countours when perturbations at all radii are in phase and

(b) after phase mixing.

Fig. 18. Time dependence of the response to two applied pulses, $m=2$ at $t=0$ and

$m=4$ at $t=\tau$, followed an $m=2$ echo at $t=2\tau$. Upper curve: Waveforms of the electric field at the wall, lower curve: semilog plot of the magnitudes of waveforms. The echo amplitude has been increased for clarity.

Fig. 19. Real and Imaginary parts of the admittance function versus frequency

for high frequency modes ($T=0$). When $\text{Re}\{Y(\omega)\} > 0$ absorption occurs due to an upper hybrid resonance somewhere within the plasma.

Due to rotation, absorption bands are upshifted by rotation. From Ref. 41.

Fig. 20. Experimental Scan of $k = 0$ modes near the cyclotron frequency,

showing a single $m=1$ center of mass mode below the cyclotron frequency, and bands of $m=2$ and 3 Bernstein modes above.

Fig. 21. Schematic for measurement of radiation temperature from the $m=1$

mode. Emission and Absorption are measured on alternate shots and before and after the emission measurement a comparison with a calibrated noise source is made.

Fig. 22. Emission and absorbtion traces versus time. As the density decays

the resonance sweeps through the receiver frequency and by changing the magnetic field slightly the resonance can be positioned at various times. Lowest trace is semilog plot of density with each tic mark indicating a factor of 10.

Fig. 23. Emission, Absorption, Temperature versus time obtained from 35 traces similar to those shown in Fig. 22.

Fig. 24. Model for emission and absorption. Left, electrical schematic of the of the experiment. Right, equivalent circuit with the plasma replaced by equivalent noise source and its impedance function.

Fig. 25. Experimentally determined frequency downshift and linewidth versus time from the $m=1$ mode, as determined from traces similar to those of of Fig. 22.

Fig. 26. Semilog plot of the free decay of the $m=1$ mode amplitude versus time when excited by a short resonant burst. Traces are for 2 to 16 sectors terminated in 50Ω , indicating that additional traces increase the decay rate.

Fig. 27. Measured free decay rate of the $m=1$ mode versus the number of sectors with resistors. The non-zero intercept indicates an *intrinsic* damping of the $m=1$ mode.

TABLE 1. ADVANCES IN NONNEUTRAL PLASMAS

(The last column indicates references in the text)

1945	BRILLOUIN EQUILIBRIUM	1
1954	BEAMS IN MICROWAVE TUBES	3,4,5,6
1965	HYPERBOLIC ION TRAP	14
1968	RELATIVISTIC BEAM EQUILIBRIA	9
1974	BOOK ON NONNEUTRAL PLASMAS	12
1975	CYLINDRICAL ELECTRON TRAP	22,23
1987	COLLISIONAL EQUILIBRATION	25
1989	VORTEX DYNAMICS	24,26,27,33,34
1991	MODES OF A SPHEROIDAL PLASMA	18,19,20,21
1992	BERNSTEIN MODES	46
1994	COLLISIONLESS DAMPING AND TRAPPING	36

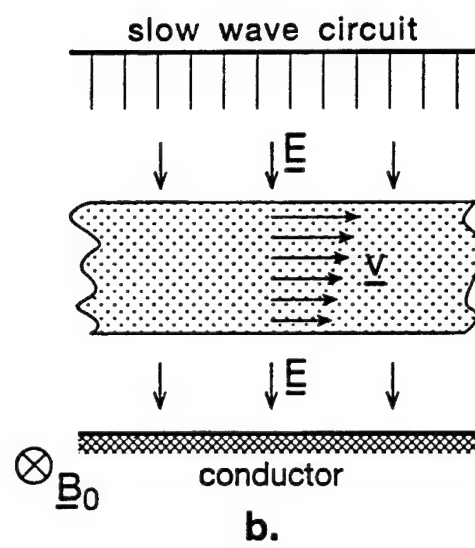
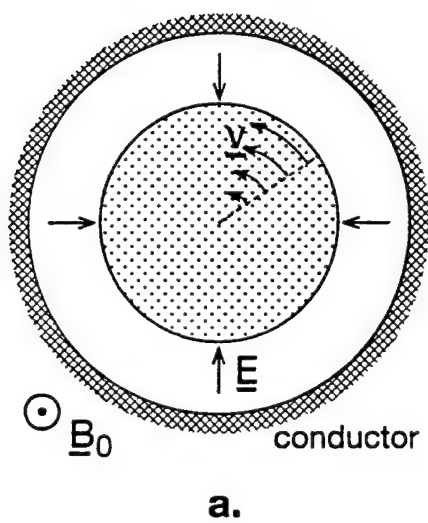


FIG 1.

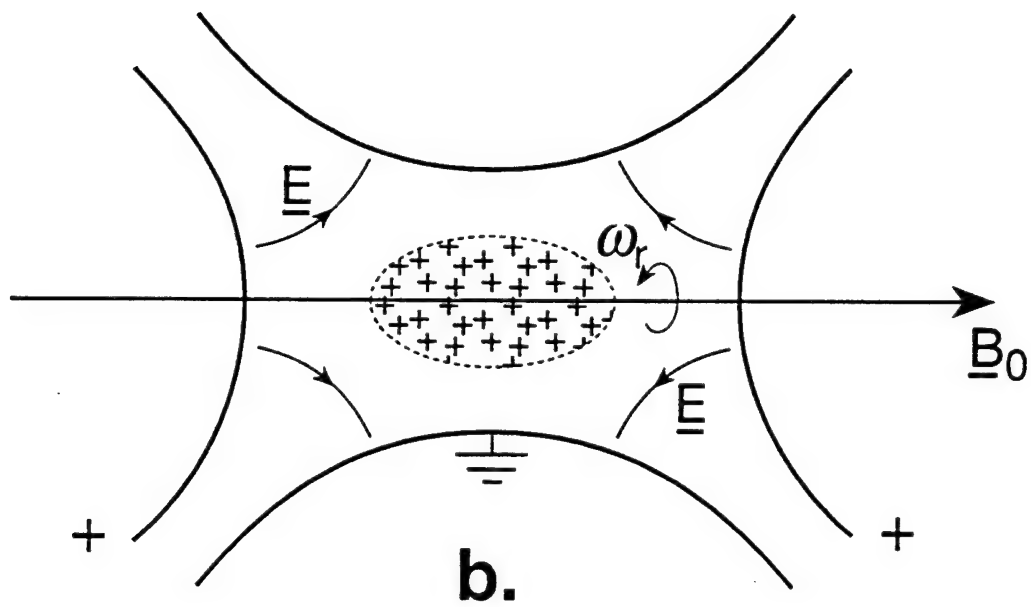
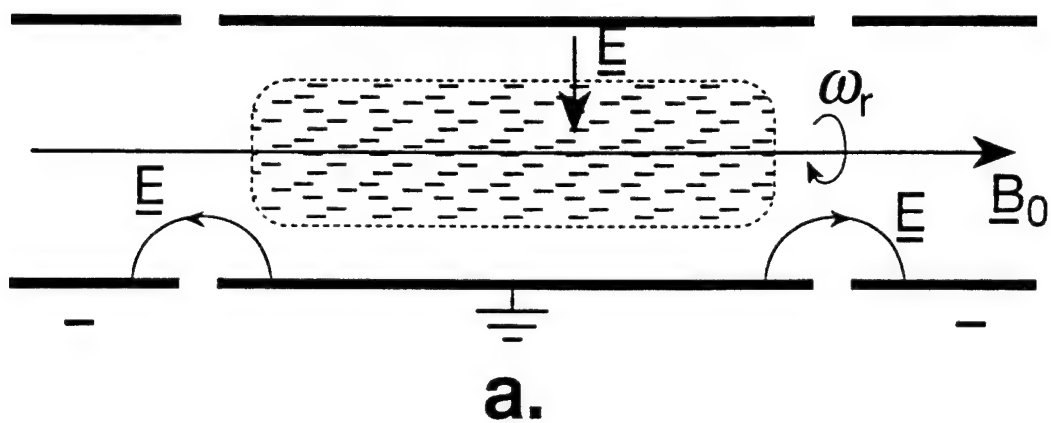


Fig 2.

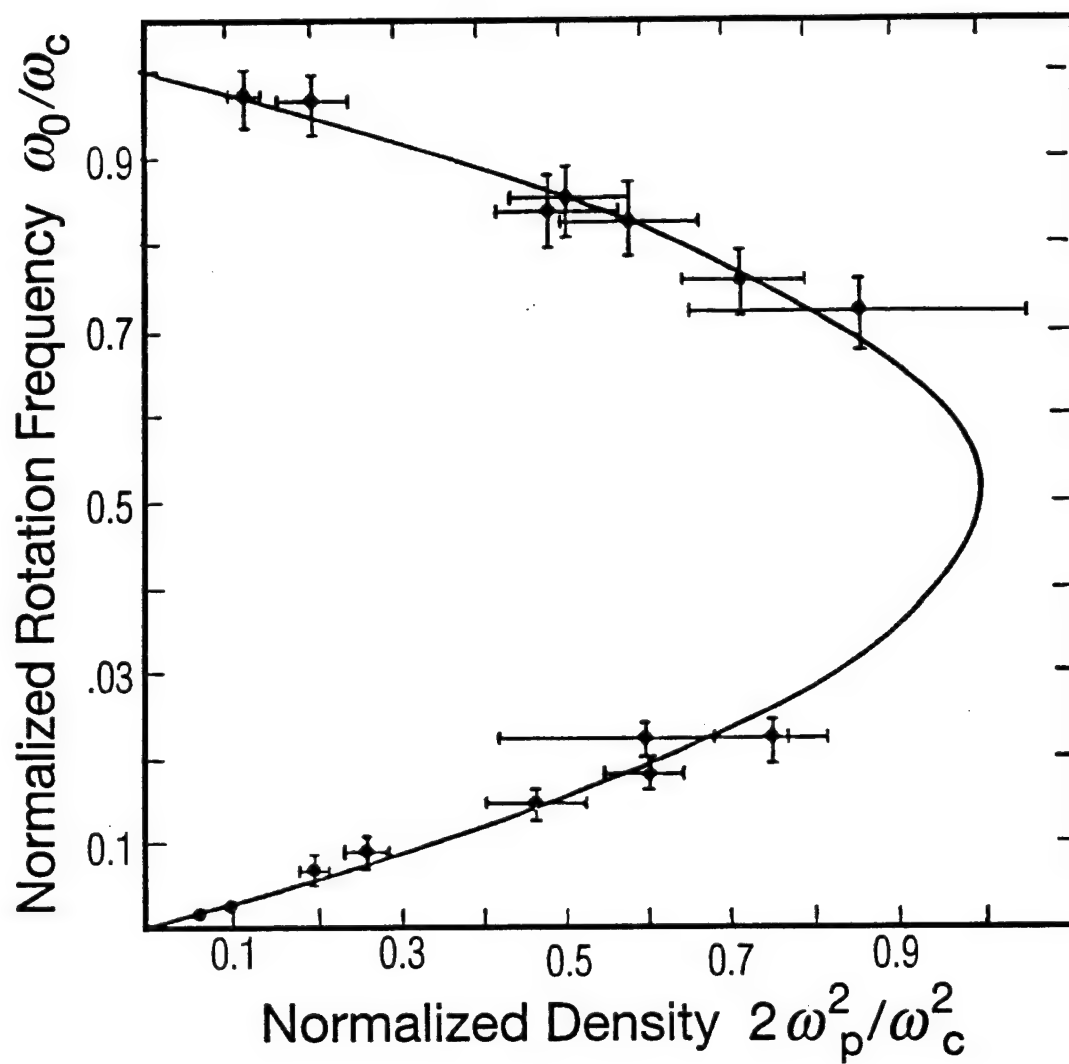
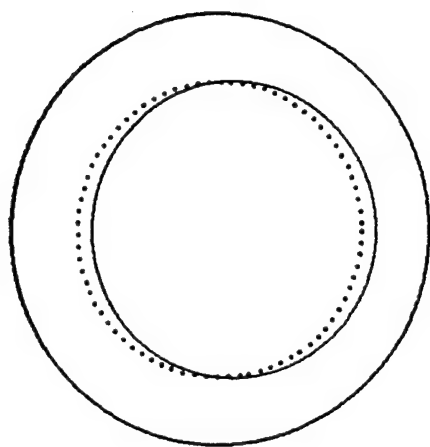
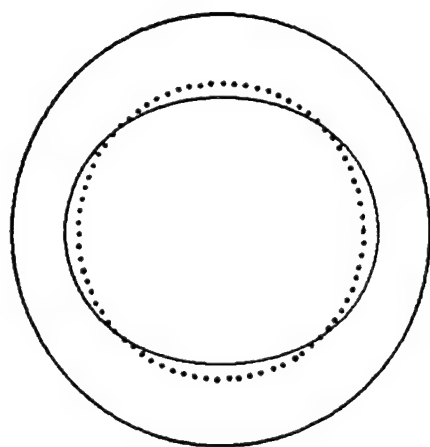


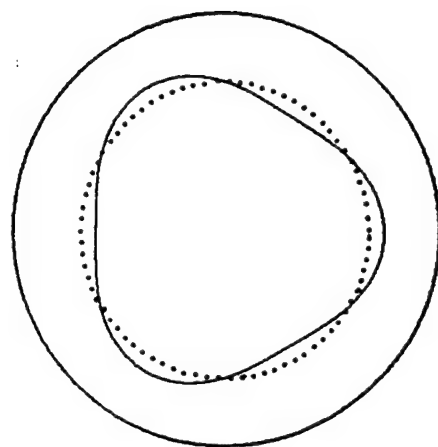
Fig. 3.



$m = 1$



$m = 2$



$m = 3$

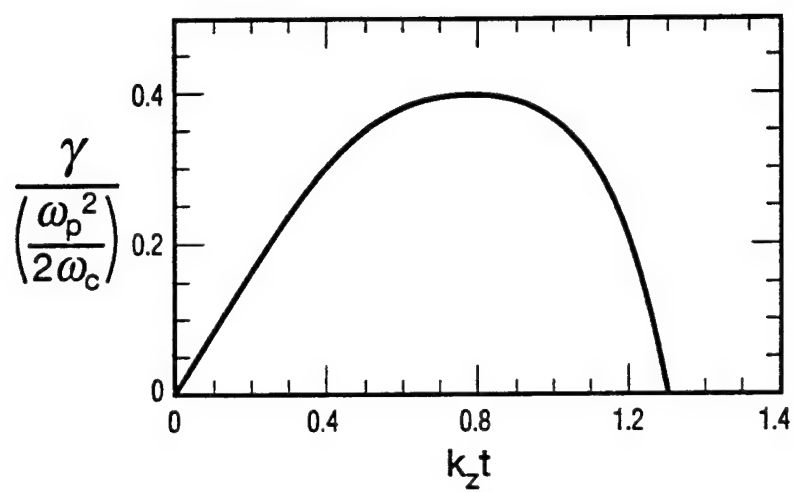


Fig. 5.

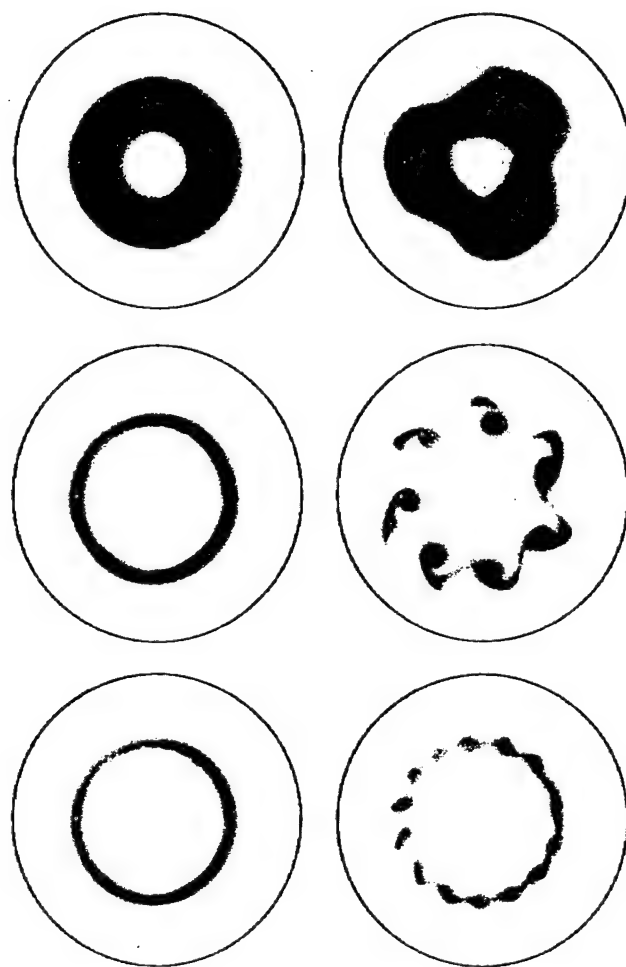


Fig 6.

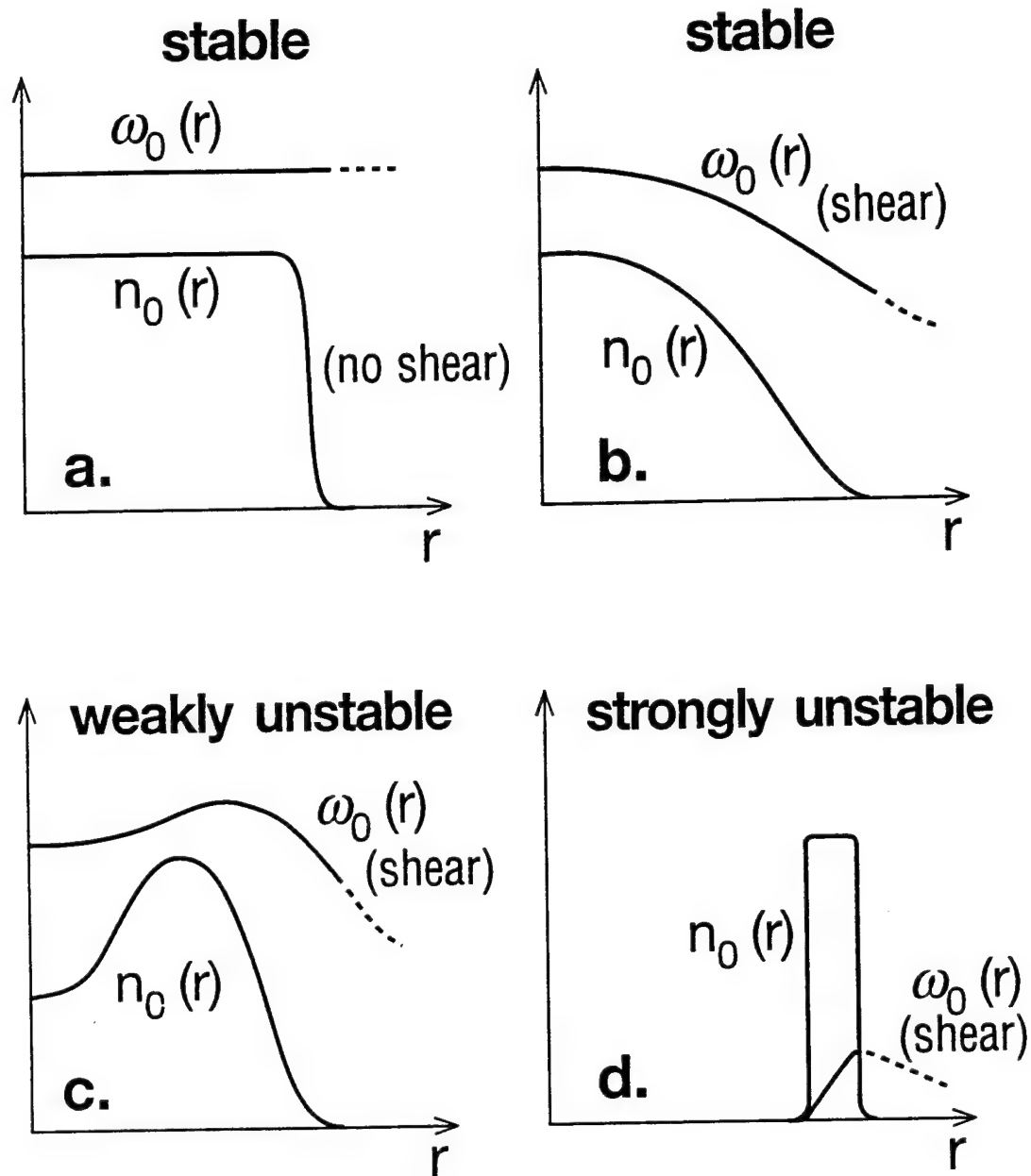
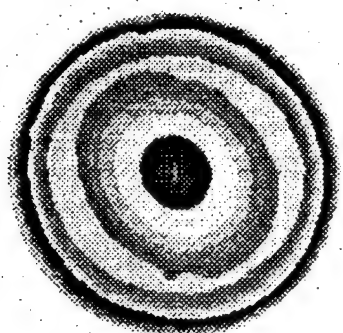
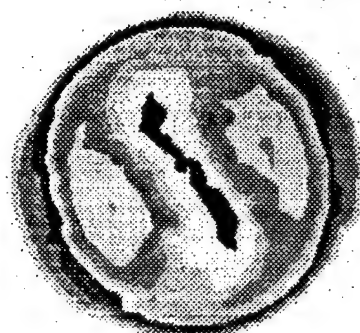


Fig. 7.

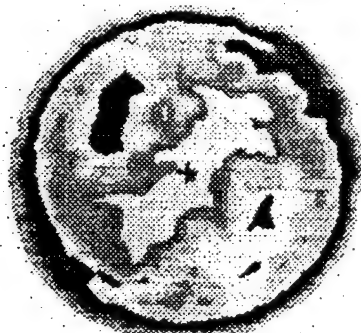
50 μ s



120 μ s



170 μ s



1000 μ s

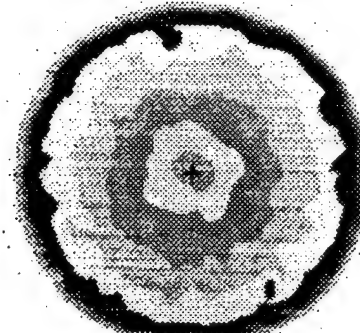


Fig 8.

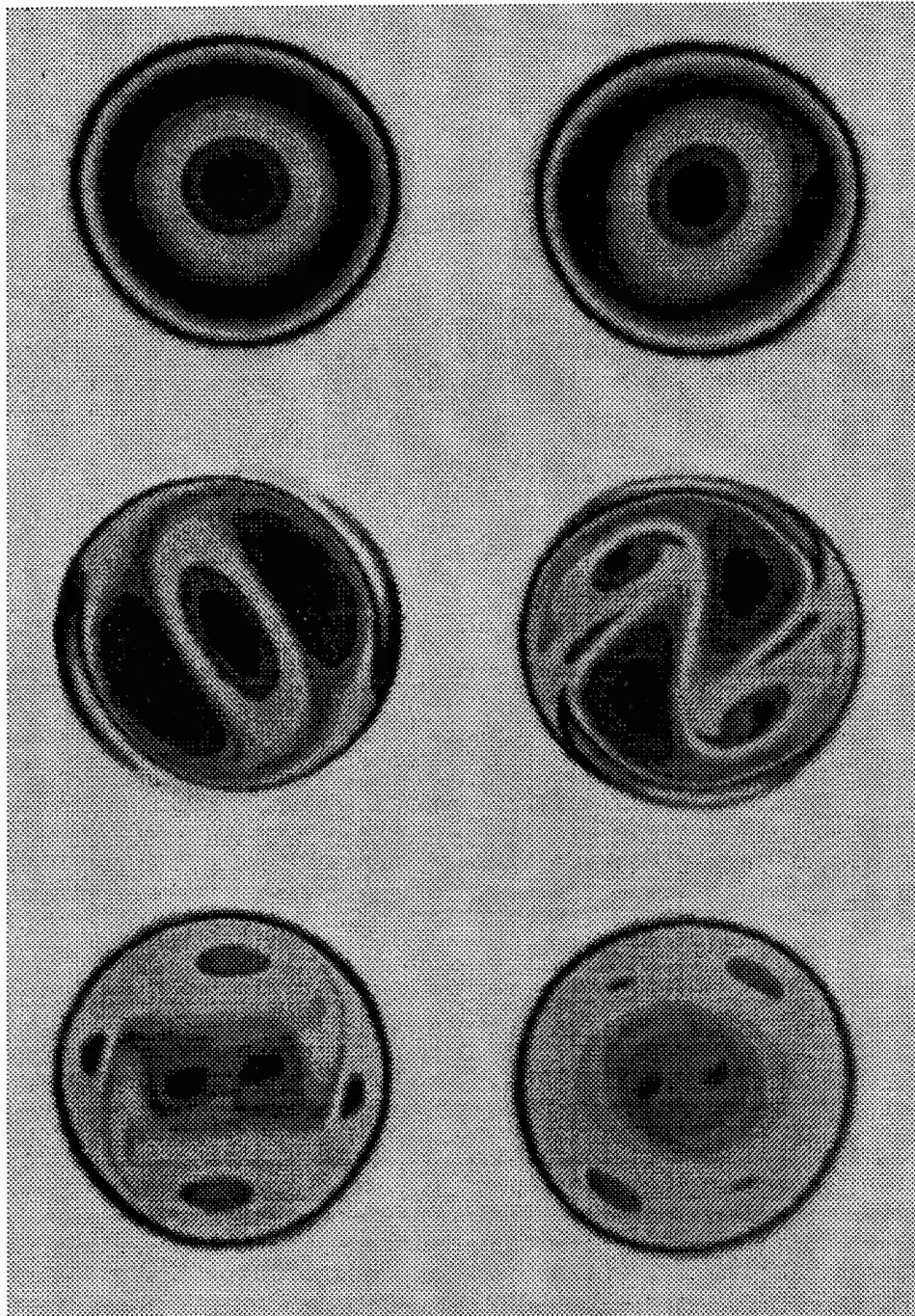
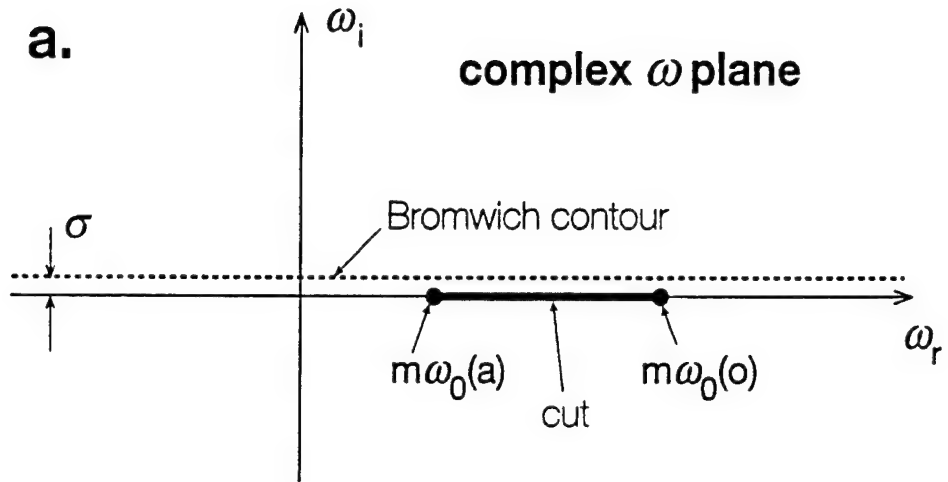
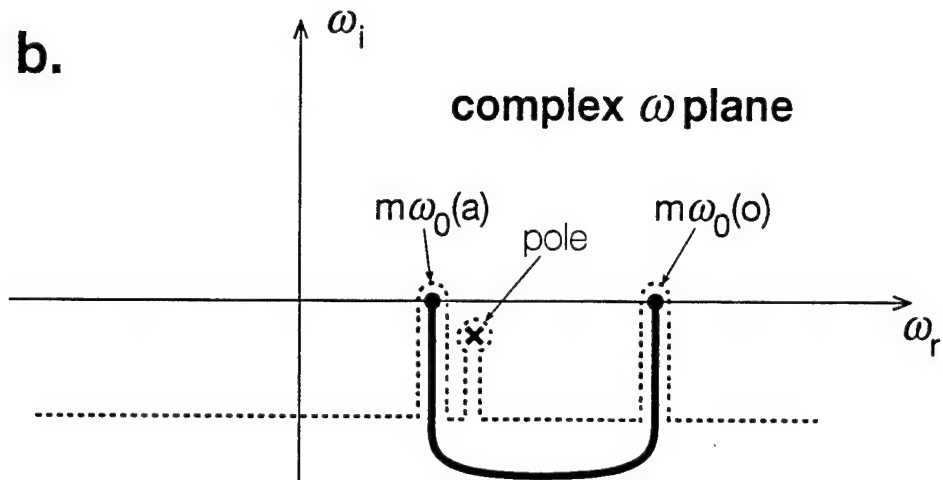


Fig 9.

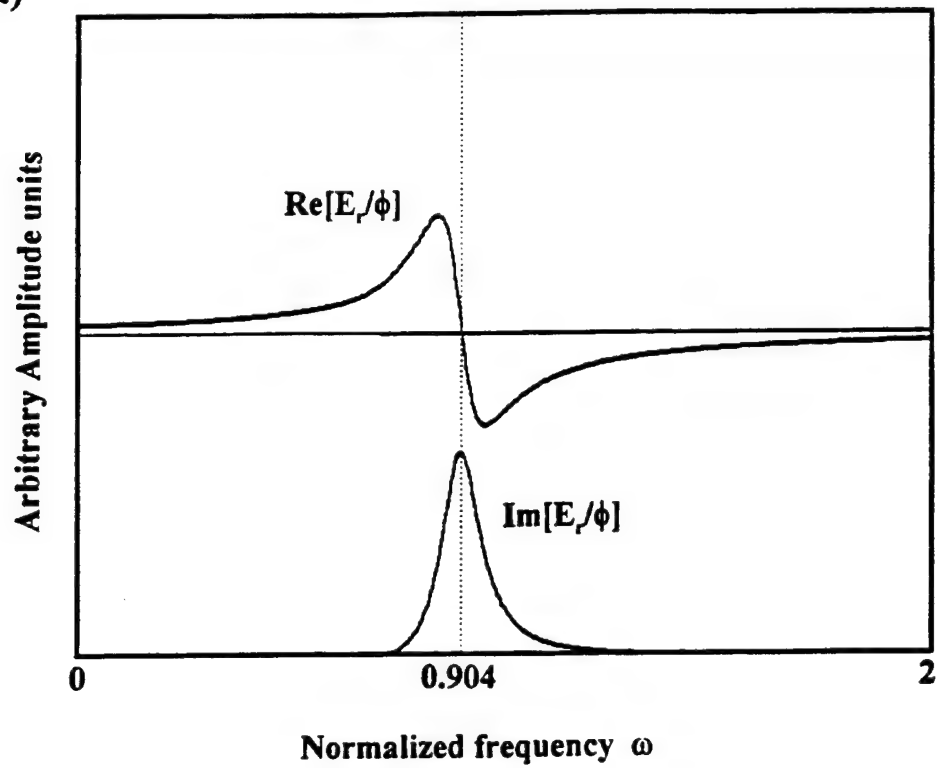
a.



b.



(a)



(b)

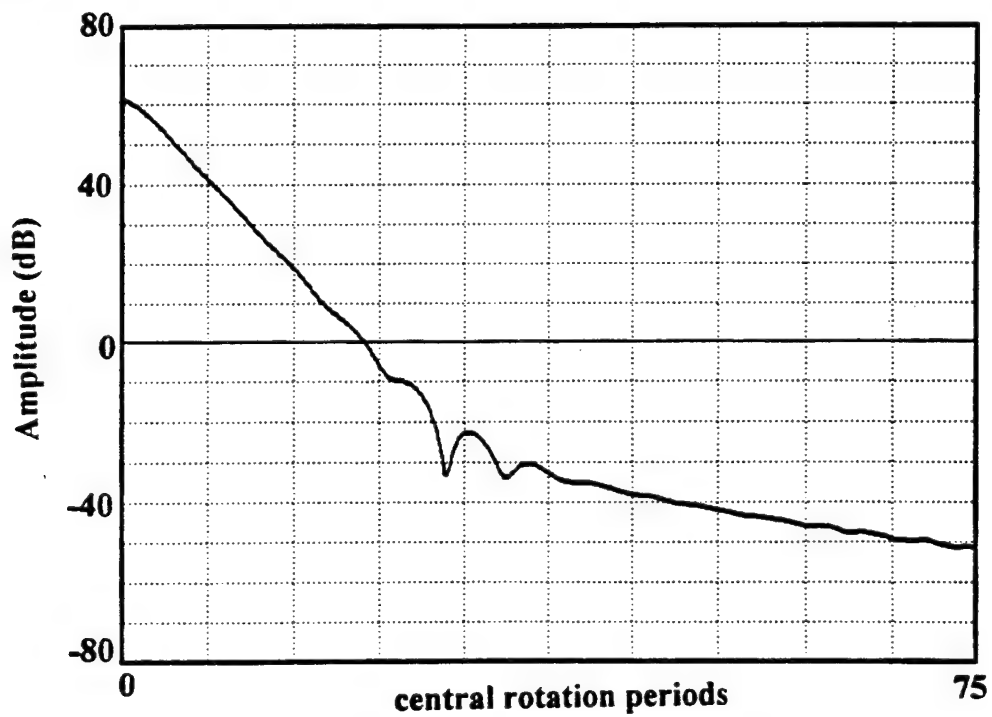
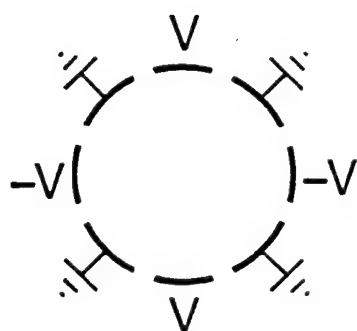
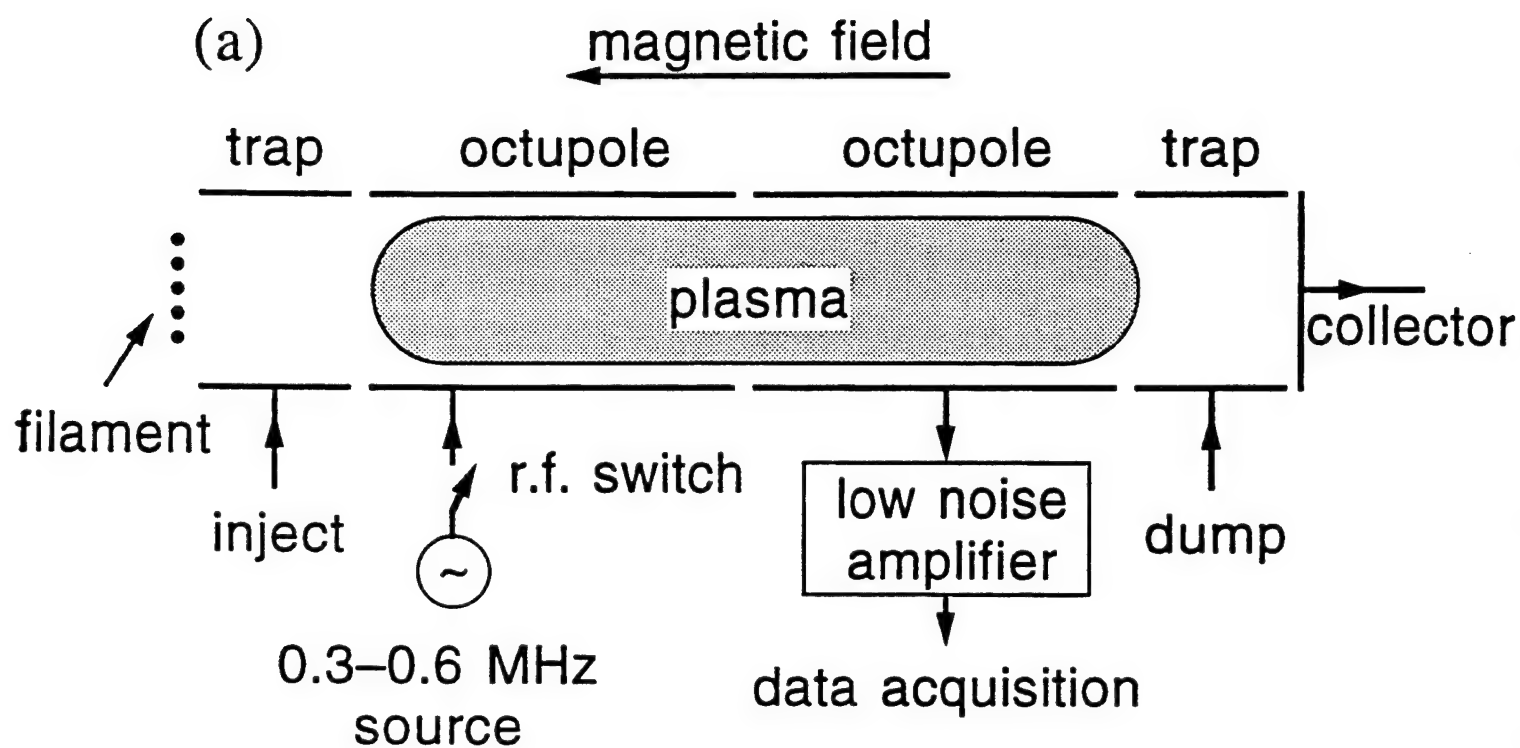
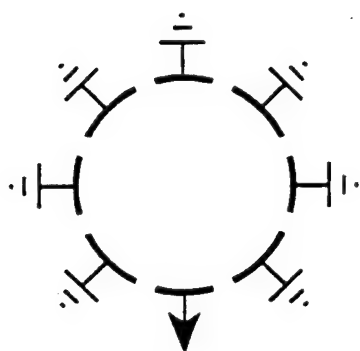


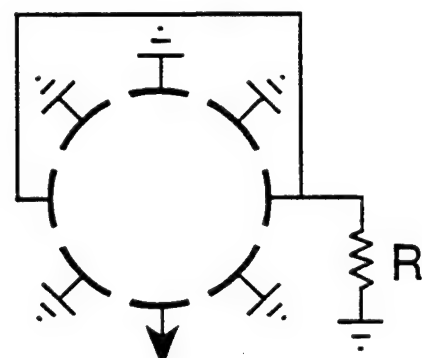
Fig. 11.



(b)



(c)



(d)

low noise amplifier

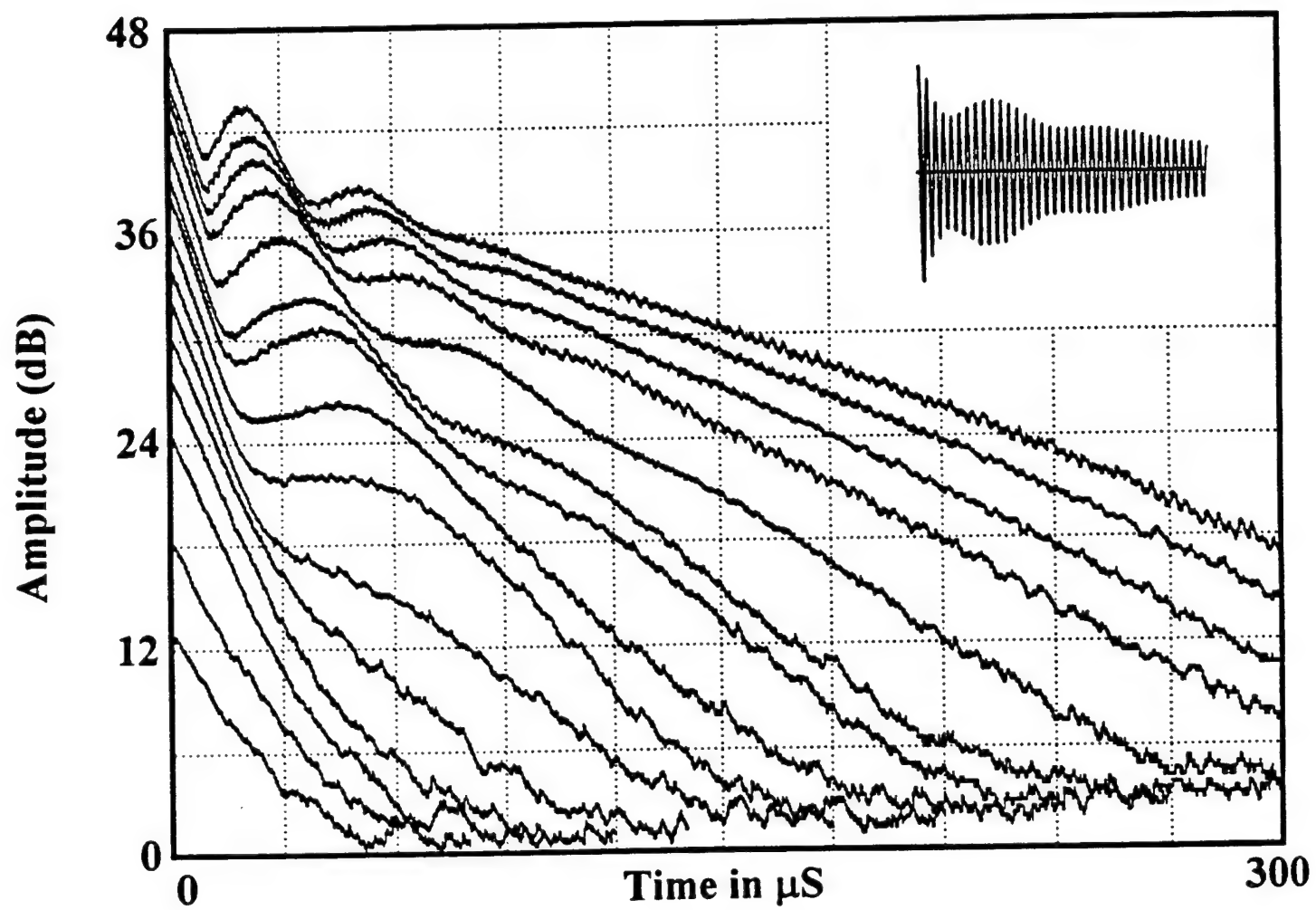
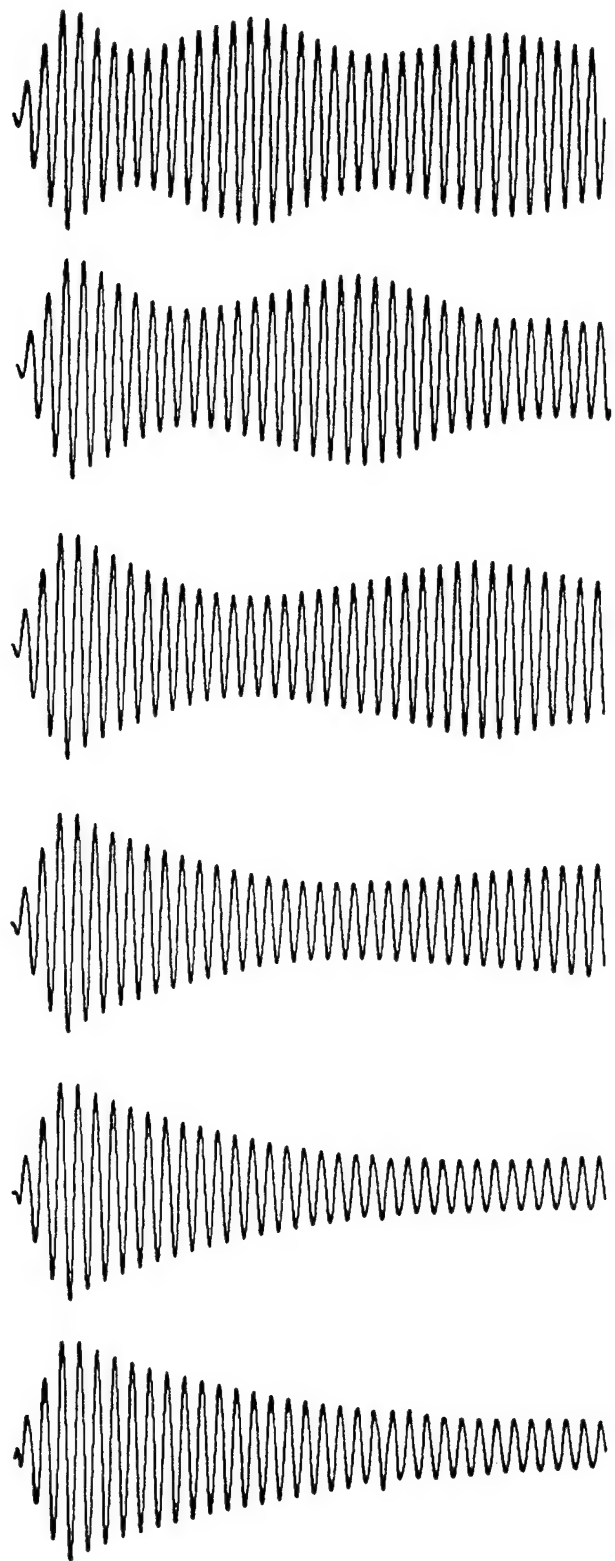


Fig. 13

increasing amplitude of excitation ↑



time →

Fig. 14.

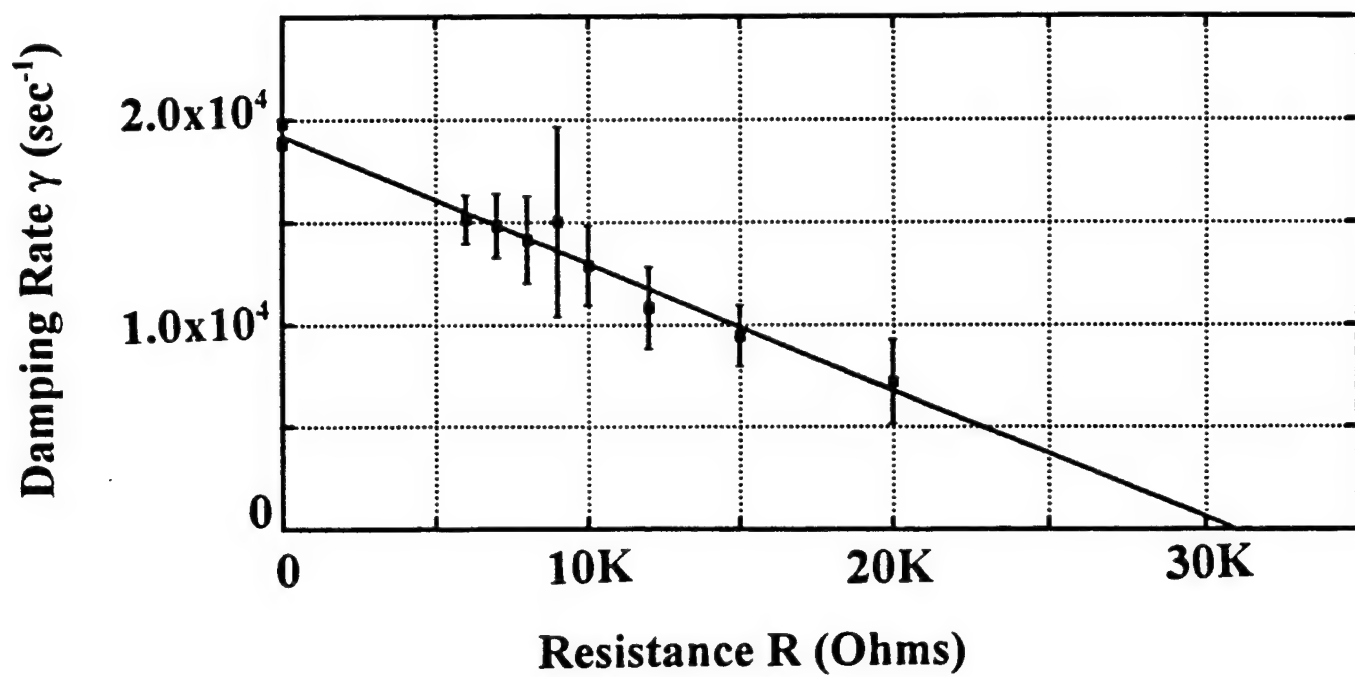


Fig. 15.

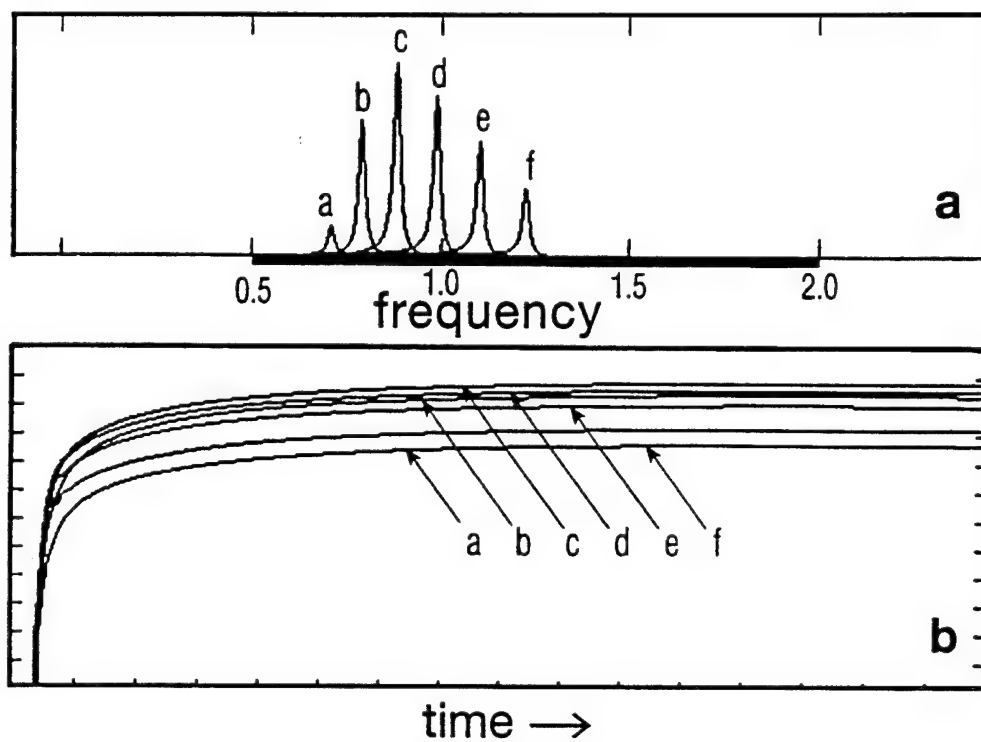
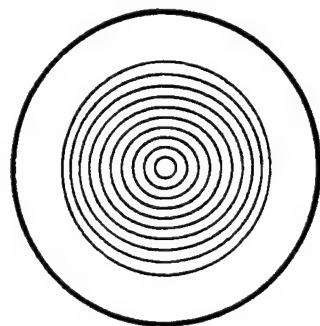
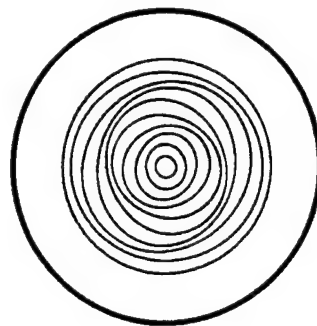


FIG. 16.



a.



b.

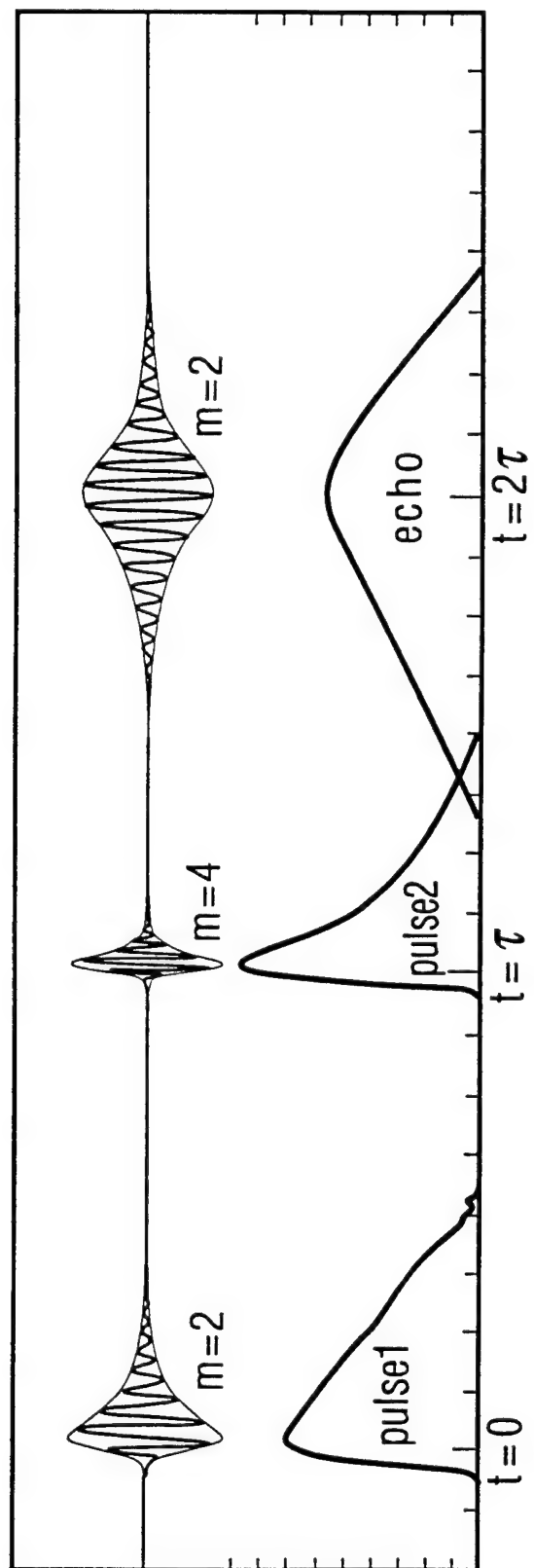


FIG. 18.

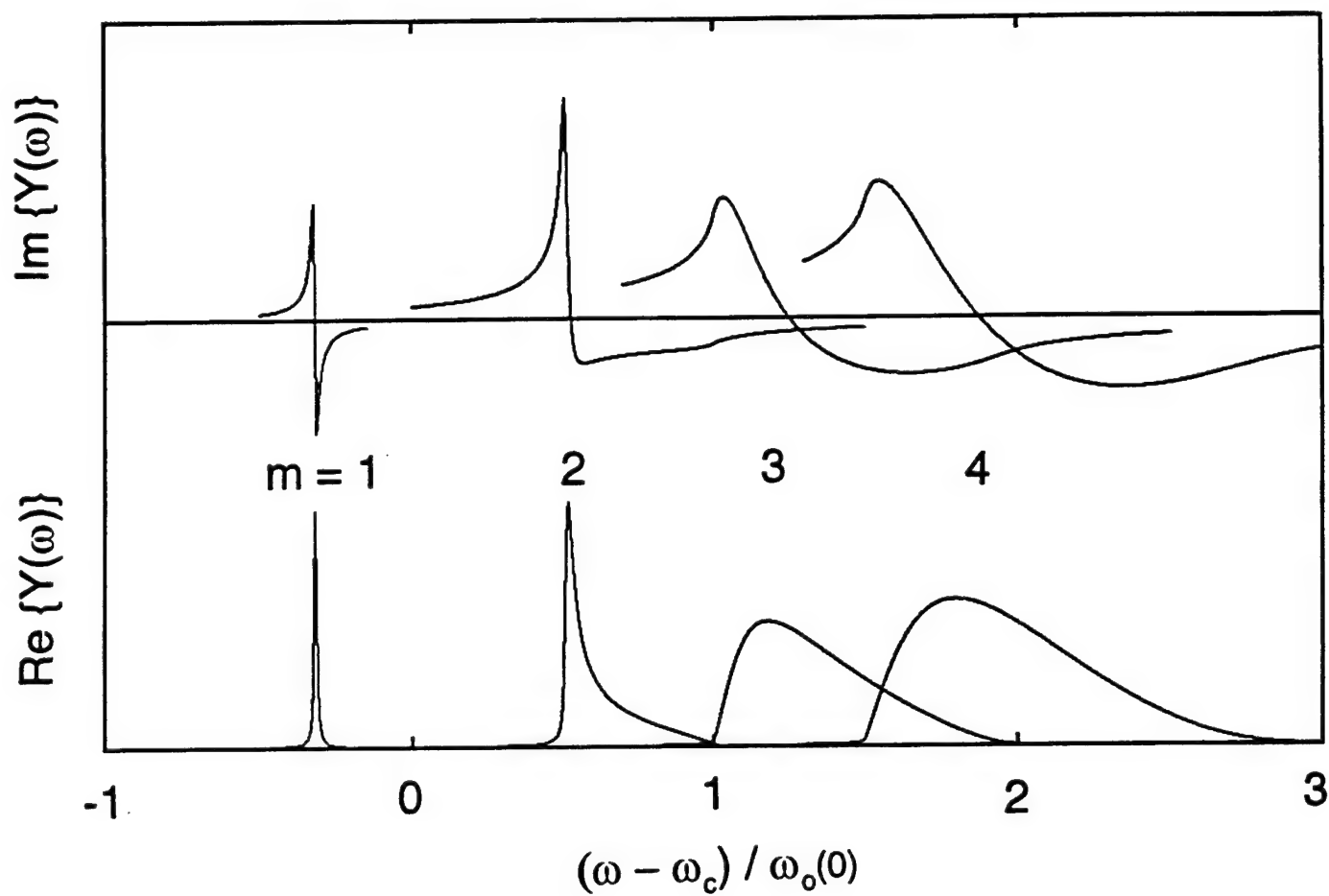


Fig. 19.

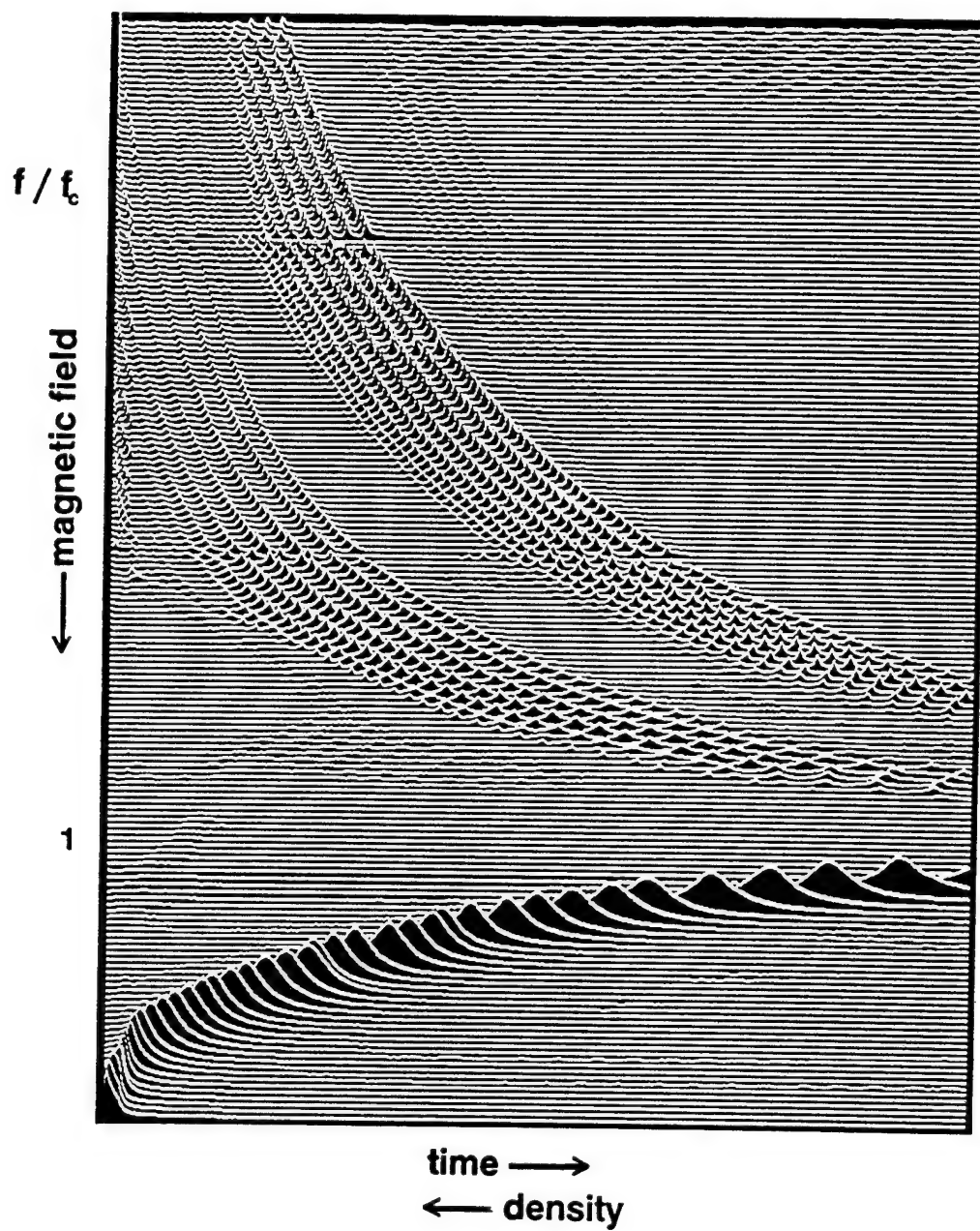
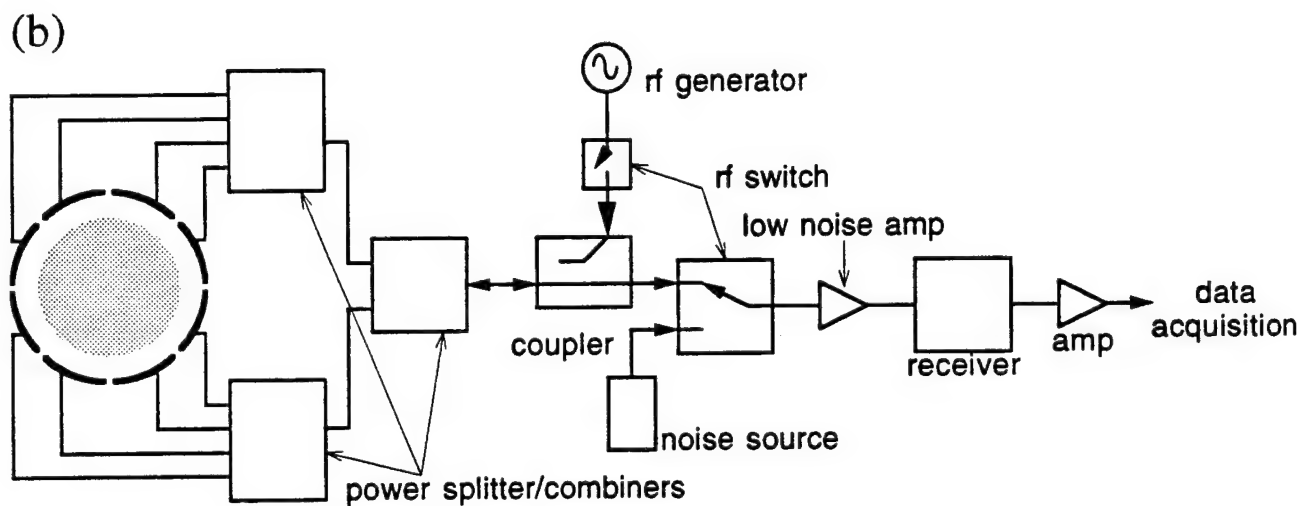
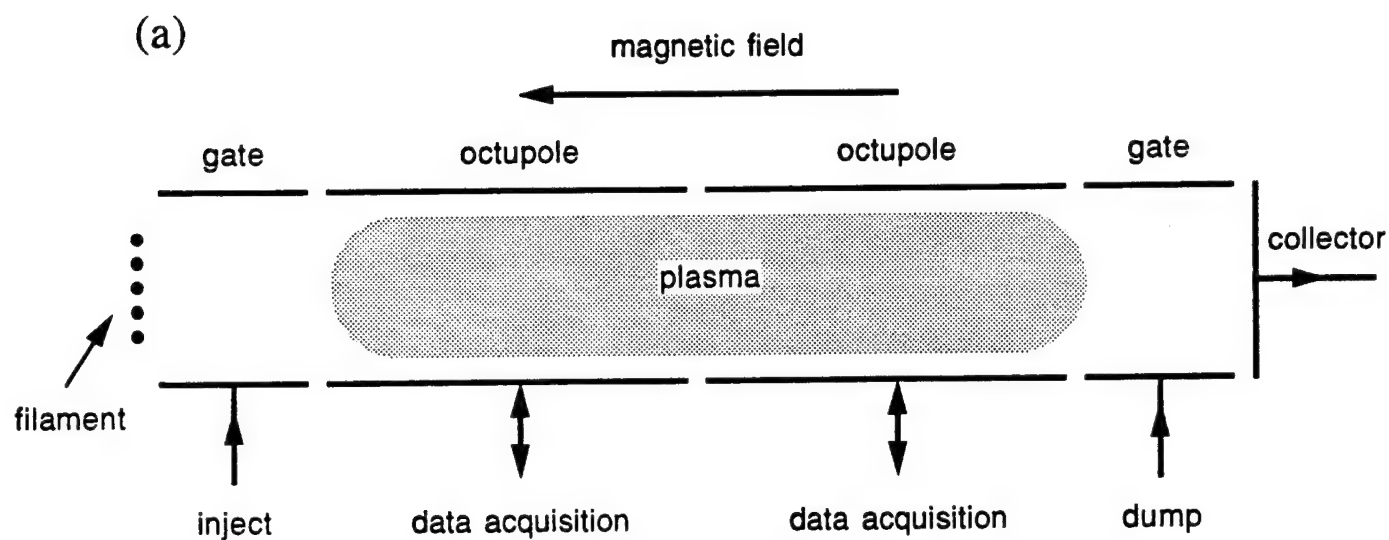


Fig. 20.



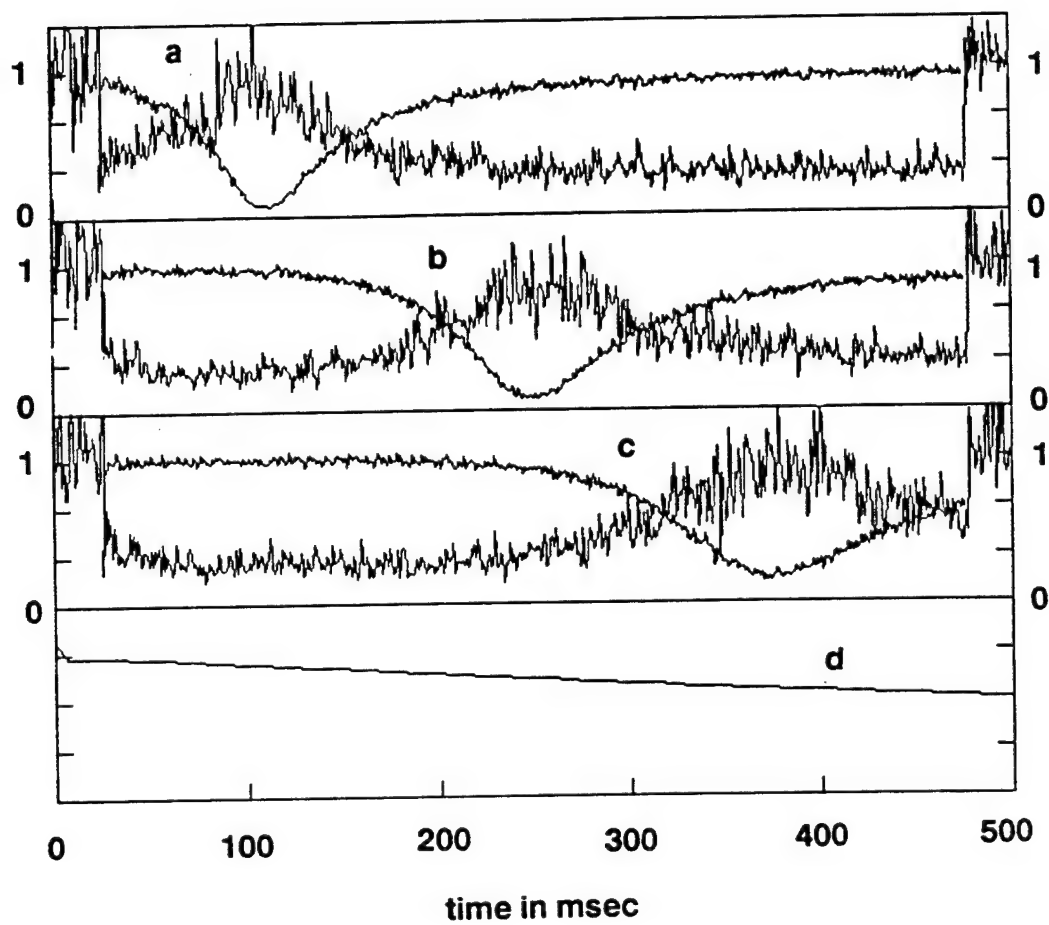


Fig. 22.

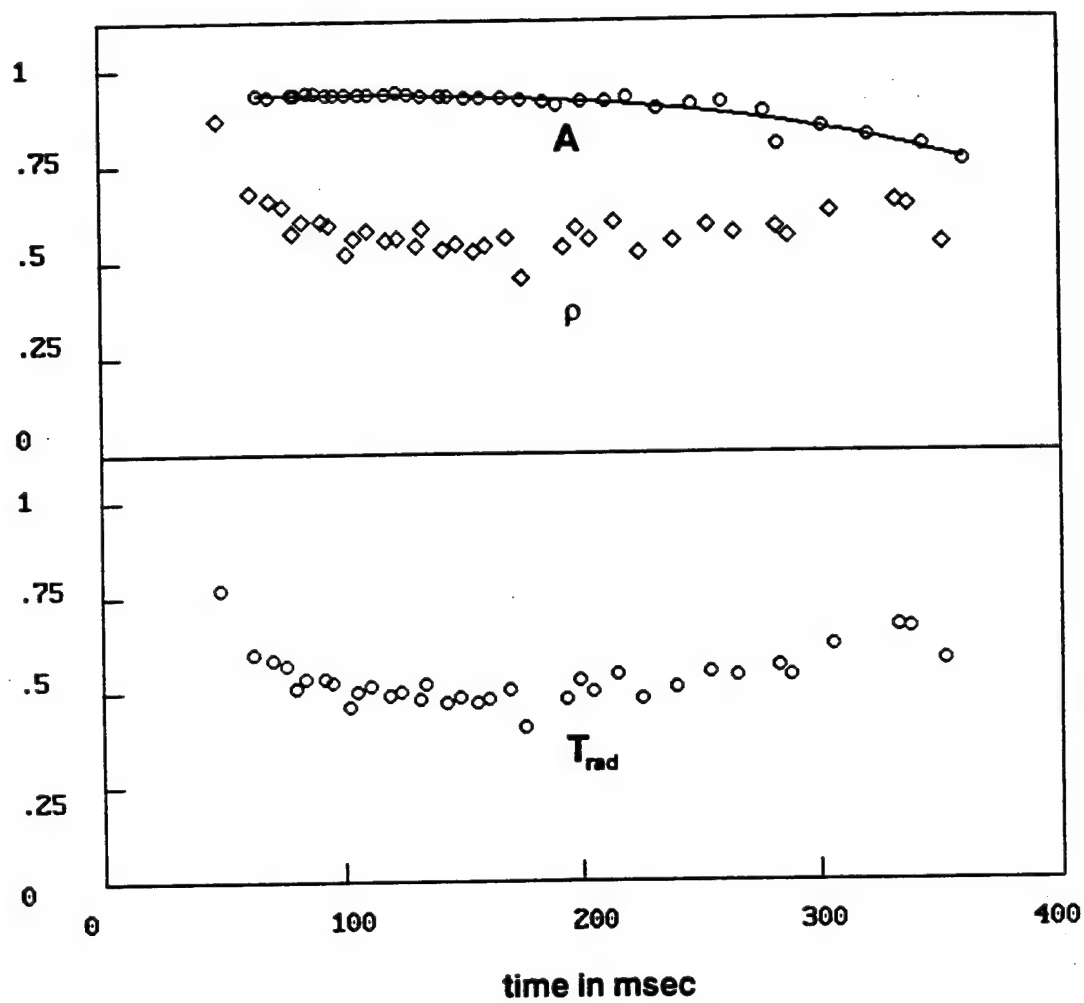
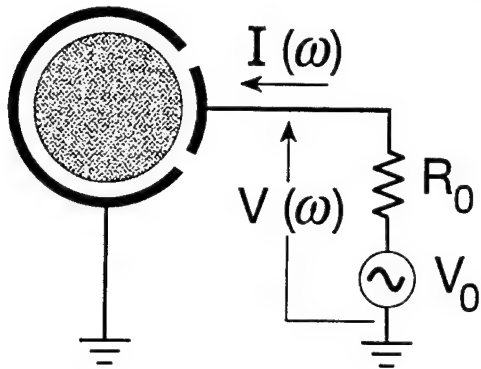
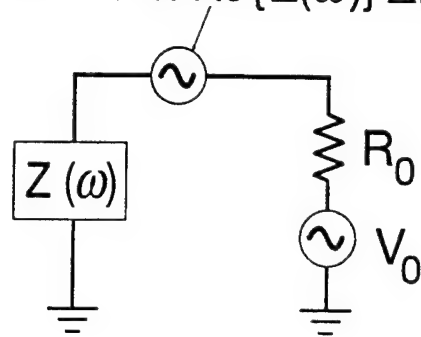


Fig. 23.

$$Y(\omega) = \frac{I(\omega)}{V(\omega)} = \frac{1}{Z(\omega)}$$



$$V^2 = 4 kT \text{Re}\{Z(\omega)\} \Delta f$$



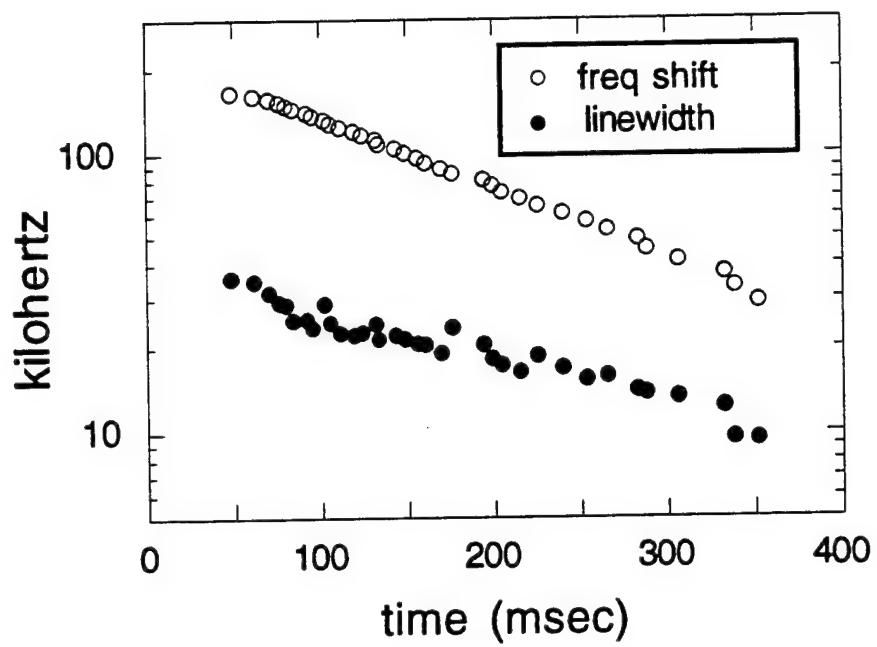


Fig. 25,

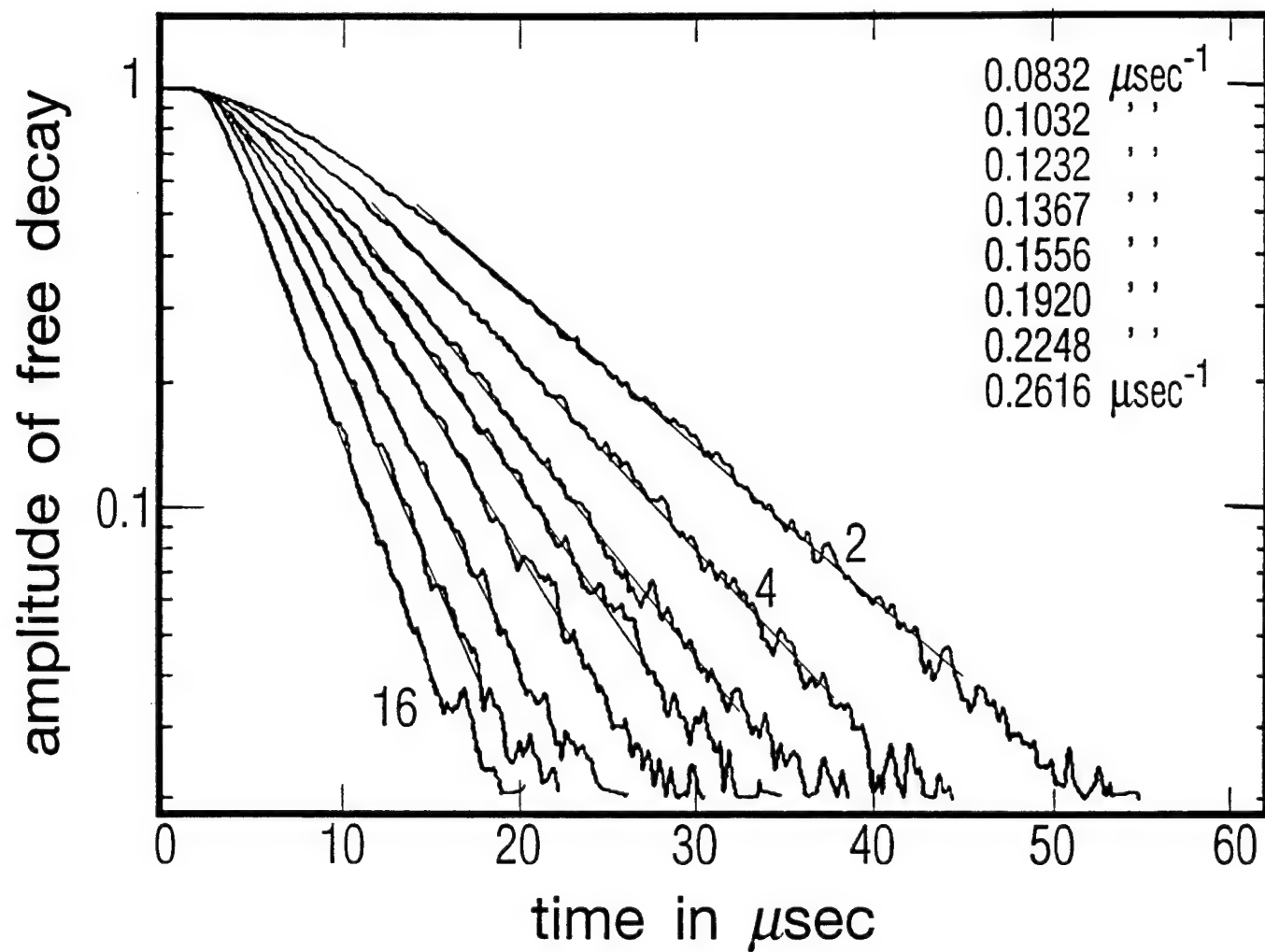


Fig. 26.

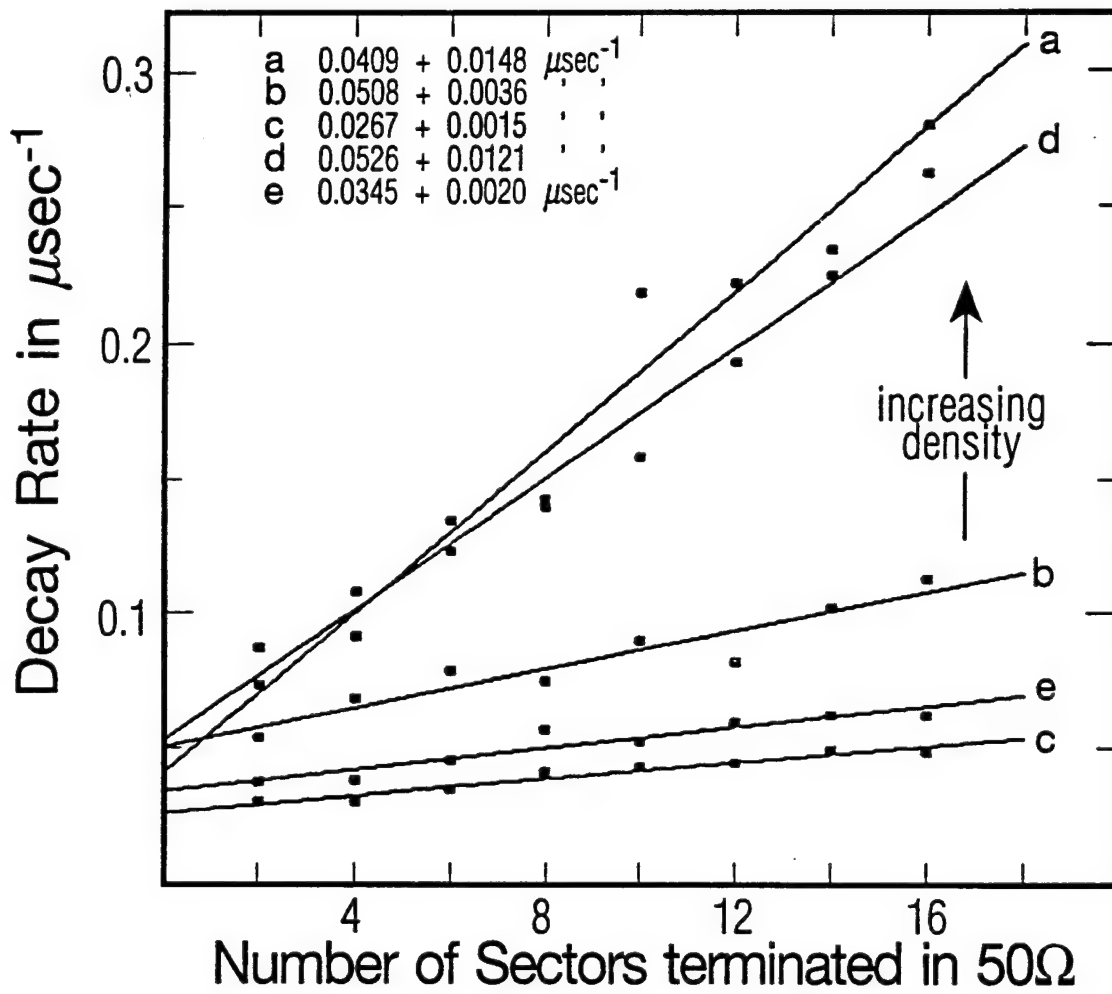


Fig. 27.

THEORY OF CYCLOTRON RESONANCE IN A CYLINDRICAL NON-NEUTRAL PLASMA

Roy W. Gould

Applied Physics

California Institute of Technology, Pasadena, CA 91125

Resonances near the cyclotron frequency of a cylindrical non-neutral plasma column with radial density and angular velocity profiles are studied. Cold plasma and warm plasma models are used to consider the various multipole modes ($e^{im\theta}$) for $k_z = 0$. For $m=1$ only a single resonance, a center of mass mode, is found. Its frequency is downshifted from the cyclotron frequency by an amount equal to the frequency of the low frequency diocotron mode. For each m greater than 1 the cold plasma model gives a continuous absorption band with spatially localized absorption at each frequency, corresponding to a continuum of singular modes. In the warm plasma model, the continuum go over to sets of discrete radially-trapped azimuthally-propagating Bernstein modes. For both cases the plasma rotation Doppler-shifts the azimuthally propagating modes up in frequency. The angular velocity profile, together with plasma temperature, determine the spacing of the Bernstein modes within a band.

Submitted to Physics of Plasmas

I. INTRODUCTION

In this paper the modes of a cylindrical nonneutral plasma column in the vicinity of the cyclotron frequency $\omega_c = eB/m_e$ are studied theoretically. This work was done in support of recent experiments.¹ Plasma rotation plays a vital role in determining the mode structure near the cyclotron frequency of nonneutral plasmas and is responsible for marked differences from otherwise similar phenomena in neutral plasmas. Nonneutral plasmas have been studied extensively in recent years and there are two good summaries of this work.^{2,3} However there has been little attention to high frequency phenomena. A notable exception is the early theoretical work of Krall and Davidson^{3,4} in which they show how to carry over certain Vlasov results from cylindrical neutral plasmas to cylindrical nonneutral plasmas. However, their results are limited to the rigid rotor equilibrium state, a situation not always obtained in laboratory plasmas because of the time required to reach this state can exceed the plasma lifetime. Recently Dubin⁵ has given a theory of the modes of cold rigid rotor spheroidal nonneutral plasma, which includes high frequency modes. Pearson⁶ gave a finite Larmor radius treatment of the Bernstein⁷ waves of a slab and cylindrical *neutral* plasmas with a spatially varying density profile but rotation was not included in the cylindrical case. More recently Prasad, Morales, and Fried⁸ have have given a small Larmor radius theory of modes of a *nonneutral slab* plasma which has sheared flow. However, because of the slab geometry, their results cannot be compared directly with experiments.

In this paper we are particularly interested in the modes of a non-equilibrium plasma in which both plasma density and angular velocity are functions of radius. While they are expected to evolve toward thermal

equilibrium, this evolution takes place on a sufficiently long time scale that the plasma may be considered to be in a steady state for the purposes of describing the phenomena discussed here. For simplicity we examine only the $k_z=0$ modes of a long column, but we consider the various cylindrical harmonics, $m \neq 0$. First we discuss the cold plasma case which leads to a continuous spectrum of modes for each m . We then give an approximate treatment of the warm plasma modes (first order in temperature), which leads to azimuthally propagating and radially trapped Bernstein modes, reminiscent of the Buchsbaum-Hasegawa modes⁹ which occur near $2\omega_c$ in a neutral plasma which has a radial density profile but no rotation¹⁰.

It is instructive as a preliminary to recall the behavior of a cold cylindrical *neutral* plasma whose density depends upon radius but which is not rotating. When an oscillating electric field is applied externally, the plasma exhibits a spatially localized resonant response at the radius where $K_{\perp}(r) = 1 - \omega_p^2(r)/(\omega^2 - \omega_c^2)$, the perpendicular dielectric function, vanishes. Because of the radial dependence of density, there is a range of frequencies for which this condition can be satisfied, corresponding to the range of upper hybrid frequencies within the plasma. This leads to a continuum of singular eigenmodes, similar to those found in other problems^{11,12}, and an upper hybrid continuum absorption band.

A *non-neutral* plasma column is necessarily in rotation in order to be in a steady state. This rotation gives rise to a Doppler shift of an applied frequency, and the upper hybrid resonance, as seen in the laboratory frame is upshifted. As we shall see later, the centrifugal and Coriolis forces associated with the rotation also give rise to a downshift of the single particle gyration frequency. For rigid rotor equilibria the downshifted

frequency is called the vortex frequency³. For non-rigid rotor steady states, the single particle downshift and the Doppler upshift both depend upon radius and this complicates the situation considerably.

In the remainder of the paper we study the response of the plasma to applied multipolar fields produced by the geometry of Figure 1. In Sections II-VI we discuss the cold plasma behavior of electrons and the absorption band which arises out of the continuum of singular normal modes. In Section VII we show, approximately, how the continuum goes over to a set of radially-trapped azimuthally-propagating Bernstein modes in a warm plasma, where finite Larmor radius effects are important. In Section VIII we extend the results to multiple ion species. Throughout the paper it is assumed that ω_p^2/ω_c^2 is a small parameter, and results are obtained only to first order in this parameter. We also assume that the dimensions are small compared with a free space wavelength so that retardation effects can be neglected.

II. COLD PLASMA EQUATIONS.

We consider a cylindrical non-neutral plasma which is contained by a static axial magnetic field B_0 and which has a radial density profile $n_0(r)$ which is assumed to be known. The density profile, $n_0(r)$, need not be an equilibrium profile in the thermodynamic sense, since a variety of non-equilibrium profiles can be produced which evolve on a time scale very long compared to the time scale of cyclotron resonance observation times. Associated with a given density profile, $n_0(r)$, is a radial electric field profile, $E_0(r)$, and an angular velocity profile, $\omega_0(r)$, which we describe in Section III.

The cold fluid equations of motion and continuity in Eulerian form for

cylindrical geometry and no z variation are:

$$\partial u_r / \partial t + u_r \partial u_r / \partial r + (u_\theta / r) \partial u_r / \partial \theta - u_\theta^2 / r = -(e/m_e)[E_r + u_\theta B_0], \quad [1]$$

$$\partial u_\theta / \partial t + u_r \partial u_\theta / \partial r + (u_\theta / r) \partial u_\theta / \partial \theta + u_\theta u_r / r = -(e/m_e)[E_\theta - u_r B_0], \quad [2]$$

$$\partial n / \partial t + (1/r) \partial(r n u_r) / \partial r + (1/r) \partial(r n u_\theta) / \partial \theta = 0. \quad [3]$$

Maxwell equations for the quasi-static electric field are:

$$(1/r) \partial(r E_\theta) / \partial r - (1/r) \partial E_r / \partial \theta = 0, \quad [4]$$

$$(1/r) \partial(r E_r) / \partial r + (1/r) \partial E_\theta / \partial \theta = - n e / \epsilon_0. \quad [5]$$

III. THE STEADY STATE.

In the steady state, E_θ and u_r vanish and the remaining quantities, E_r , u_θ , and n are independent of θ and t . The steady state quantities obey the equations:

$$r \omega_0^2 = (e/m_e) E_{0r} + r \omega_c \omega_0, \quad [6]$$

$$d(r E_{0r}) / dr = - r n_0 e / \epsilon_0, \quad [7]$$

where $\omega_0(r) = u_{0\theta}(r)/r$ is the angular velocity at radius r . The subscripts 0 refer to the steady state values. Since we are concerned with the low density limit, $(\omega_p^2 / \omega_c^2) \ll 1$, the rotational angular velocity, ω_0 , is everywhere small compared with the cyclotron frequency and the centrifugal force term $r \omega_0^2$ of [6] may be neglected. This corresponds to being well below the Brillouin density limit. Eqs. 6 and 7 then lead to the usual low density relationship between angular velocity and density:

$$(1/r) d[r^2 \omega_0(r)] / dr = \omega_p^2(r) / \omega_c. \quad [8]$$

We find it convenient to normalize the radial-dependent plasma frequency and rotational angular velocity to their central values and introduce the functions $f(r)$ and $g(r)$ to express the *normalized* density and angular velocity functions. We let

$$\omega_p^2(r) = \omega_p^2(0) f(r) \quad [9]$$

$$\omega_0(r) = \omega_0(0) g(r) \quad [10]$$

where, by definition, $f(0) = g(0) = 1$. It follows from Eq. 8 that the central rotation frequency is $\omega_0(0) = \omega_p^2(0)/2\omega_c$. With these definitions Eq. 8 takes the form

$$d[r^2 g(r)]/dr = 2 r f(r). \quad [8a]$$

A simple illustration of a monotonically decreasing density profile is the parabolic density profile $f(r)=1-(r/a)^2$, for $r < a$. This profile, together with the corresponding angular velocity profile, $g(r)=1-.5(r/a)^2$, will be used in later discussions, although the general approach is not limited to this example. $g(r)$ is obtained by integrating Eq. 8a and both $f(r)$ and $g(r)$ are shown in Fig. 2.

IV. SMALL PERTURBATIONS.

The linearized forms of Eqs. 1-3 for small perturbations (subscript 1) when one assumes $\exp(im\theta - i\omega t)$ dependence are:

$$-i[\omega - m\omega_0]u_{1r} + [\omega_c - 2\omega_0]u_{1\theta} = -(e/m_e)E_{1r} \quad [11]$$

$$-[\omega_c - 2\omega_0 - r d\omega_0/dr]u_{1r} - i[\omega - m\omega_0]u_{1\theta} = -(e/m_e)E_{1\theta} \quad [12]$$

$$-i(\omega - m\omega_0)n_1 + (1/r)d(rn_0 u_{1r})/dr + (im/r)n_0 u_{1\theta} = 0 \quad [13]$$

which are readily solved for u_{1r} and $u_{1\theta}$ in terms of E_{1r} and $E_{1\theta}$:

$$u_{1r} = -\left(\frac{e}{m_e}\right) \frac{-i[\omega - m\omega_0]E_{1r} - [\omega_c - 2\omega_0]E_{1\theta}}{-[\omega - m\omega_0]^2 + [\omega_c - 2\omega_0][\omega_c - 2\omega_0 - r d\omega_0/dr]}, \quad [14]$$

$$u_{1\theta} = -\left(\frac{e}{m_e}\right) \frac{[\omega_c - 2\omega_0 - r d\omega_0/dr]E_{1r} - i[\omega - m\omega_0]E_{1\theta}}{-[\omega - m\omega_0]^2 + [\omega_c - 2\omega_0][\omega_c - 2\omega_0 - r d\omega_0/dr]} \quad [15]$$

Now $\omega' = \omega - m\omega_0(r)$ is the local Doppler shifted frequency seen by a fluid element drifting around the axis at radius r . The other term in the denominator of

Eqs. 14 and 15 can be identified as the square of the effective single particle gyration frequency

$$\omega'_c = [(\omega_c - 2\omega_0)(\omega_c - 2\omega_0 - r d\omega_0/dr)]^{1/2}. \quad [16]$$

This frequency is downshifted slightly from $\omega_c = eB_0/m_e$ by the centrifugal and Coriolis forces and, in general, the downshift is also dependent upon radius. However, in the special case when the plasma density is independent of radius, ω_0 is also independent of radius and one recovers the rigid rotor vortex frequency, $\omega'_c = \omega_c - 2\omega_0$, which is also independent of radius.

Since we are primarily interested in frequencies close to the cyclotron frequency we can simplify Eqs. 14 and 15. It is useful to introduce the *normalized* frequency λ through the definition

$$\omega = \omega_c + (\omega_p^2(0)/2\omega_c) \lambda, \quad [17]$$

where λ is the frequency difference $\omega - \omega_c$, normalized to the central rotation frequency. Then to first order in $\omega_p^2(0)/\omega_c^2$, Eqs. 14 and 15 can be written

$$n_0 e u_{1r} = -i n_0 e u_{1\theta} = \frac{-i \omega_c \epsilon_0 f(r) [E_{1r} - i E_{1\theta}]}{[\lambda - mg + 2g + .5 r dg/dr]} \quad [18]$$

or, more simply, as $n_0 e u_+ = 0$ and

$$n_0 e u_- = \frac{-2i \omega_c \epsilon_0 f(r) E_-}{[\lambda - mg + g + f]} \quad [19]$$

We have defined $E_{\pm} = E_{1r} \pm i E_{1\theta}$ and $u_{\pm} = u_{1r} \pm i u_{1\theta}$, and used dg/dr from Eq. [8a]. E_{\pm} and u_{\pm} denote amplitudes of the two circularly polarized components of the electric field and the velocity. From this result we see that close to cyclotron resonance only one circularly polarized component is effective in exciting the motion, namely that which matches the gyration sense of the particles. The velocity which it produces is circularly polarized with

the same sense. Linear combinations of the two Maxwell equations, Eqs. 4 and 5 give

$$(1/r)d(rE_{\pm})/dr \pm (m/r)E_{\pm} = -n_1 e/\epsilon_0 \quad [20]$$

and the continuity equation, Eq. 13, together with Eq. 18 gives

$$-n_1 e/\epsilon_0 = \frac{1}{r} \frac{d}{dr} \frac{rfE_-}{[\lambda - mg + g + f]} - \frac{m}{r} \frac{fE_-}{[\lambda - mg + g + f]}, \quad [21]$$

where $\omega - m\omega_0 \approx \omega_c$ has been used. Defining a dielectric function for right circularly polarized fields as $K(r) = 1 - f/[\lambda - mg + g + f]$, the quantity $D_- = K E_-$ obeys a particularly simple equation:

$$\frac{1}{r} \frac{d}{dr}(rD_-) - \frac{m}{r} D_- = 0. \quad [22]$$

D_- is the *displacement* associated with the resonantly polarized component.

V. COLD PLASMA SOLUTIONS.

The solution of Eq. 22 is simply $D_-(r) = A r^{m-1}$, where A is an arbitrary constant, and the corresponding electric field is

$$E_-(r) = A r^{m-1} / K(r). \quad [23]$$

For $m \leq 0$ A must be zero in order for the field to be zero at $r=0$. Thus E_- is zero for $m \leq 0$. Only applied fields with positive m have the correct circular polarization to elicit a response from a pure electron plasma. Thus we need only consider positive m . For $m=+1$, $D_- = A$ is independent of radius. This corresponds to a center of mass mode.

Having obtained the solution for E_- we substitute it into [21] to obtain the perturbed density into Eq. 20 to get the equation for E_+ :

$$\frac{1}{r} \frac{d}{dr} (rE_+) + \frac{m}{r} E_+ = \frac{1}{r} \frac{d}{dr} \{ r A r^{m-1} [1 - \frac{1}{K}] \} - \frac{m}{r} A r^{m-1} [1 - \frac{1}{K}]. \quad [24]$$

The right side of Eq 24. gives the perturbed density in the plasma and we can use this expression to obtain the radial dependence of the perturbed density

for various applied frequencies. The perturbed density exhibits a singularity at the radius where $K(r)$ vanishes. This condition corresponds to a localized upper hybrid resonance condition, when the various frequency shifts incorporated into $K(r)$ are taken into account. To solve for E_+ we note that the substitution $E_+ = \psi(r)/r^{(m+1)}$ leads to an integrable equation for ψ , whose solution is

$$\psi(r) = A \int_0^r \frac{d}{dr'} \left[\frac{1}{K(r')} - 1 \right] r'^{2m} dr' . \quad [25]$$

The ratio of E_+ to E_- at a given radius is then given by

$$R_m(r) = \frac{E_+(r)}{E_-(r)} = \frac{K(r)}{r^{2m}} \int_0^r \frac{d}{dr'} \left[\frac{1}{K(r')} - 1 \right] r'^{2m} dr' . \quad [26]$$

At a radius r_{\max} beyond which the plasma density vanishes, the integral is just a constant, $K = 1$ and E_+/E_- falls off as r^{-2m} . Eq. 26 can be integrated by parts to give

$$R_m(r) = - \frac{2m}{r^{2m}} \int_0^{r_{\max}} \left[\frac{1}{K(r')} - 1 \right] r'^{2m-1} dr' , \quad [27]$$

for $r > r_{\max}$. Using the definition of $K(r')$ this can also be written

$$R_m(r) = - \frac{2m}{r^{2m}} \int_0^{r_{\max}} \left[\frac{f(r')}{\lambda - (m-1)g(r')} \right] r'^{2m-1} dr' . \quad [27a]$$

R_m is a measure of the m th multipole moment induced in the plasma column by the applied field. For the illustrative profile of Fig. 2, $r_{\max} = a$.

VI. ADMITTANCE FUNCTION.

We now relate this result, specifically the calculation of $R_m(r)$, to the measurement geometry depicted in Fig. 1. If a voltage $V e^{-i\omega t}$ is applied to the segmented cylinder shown, the current $I e^{-i\omega t}$ flowing to the electrode (as displacement current) will be

$$I = -i\omega\epsilon_0 \int_{-\theta_0}^{\theta_0} E_{1r} b d\theta \quad [28]$$

It is then straightforward to show that the observed admittance $Y = I/V$ is related to the $R_m(b)$ defined above as follows:

$$Y(\lambda) = -i\omega_c \epsilon_0 b \sum_m C_m \frac{R_m(b)+1}{R_m(b)-1} \quad [29]$$

where the $C_m = (4m/\pi)[\sin(m\theta_0)/m]^2$ are geometrical weighting factors for the various multipole contributions which depend only upon m and the angle θ_0 . C_m falls off like $1/m$ and for $\theta_0 = \pi/2$ only the odd C_m are non-zero. The fraction $(R_m+1)/(R_m-1)$ is just proportional to the m th multipole component of $E_{1r}/E_{1\theta}$ at the electrode, and from Eq. 29 it is evident that we should examine the behavior of that factor for various m . Because of the factor $(r'/b)^{2m}$ in Eq. 26 the higher multipole contributions fall off as $(a/b)^{2m}$, where we have set $r_{\max} = a$. Thus the dipole contribution ($m=1$) will dominate. If we subtract the vacuum contribution to the admittance, i.e. that part which exists in the absence of the plasma, the appropriate factor in Eq. 29 becomes $2R_m/(R_m-1)$.

A. Plasma Density Independent of Radius. For plasma of uniform density up to radius a , $f = g = 1$ for $r < a$ and Eq. 27a is particularly easy to evaluate and gives

$$R_m(b) = - (a/b)^{2m} \frac{1}{\lambda - m + 1} \quad [30]$$

so that

$$\frac{R_m(b)+1}{R_m(b)-1} = - \frac{\lambda - m + 1 - (a/b)^{2m}}{\lambda - m + 1 + (a/b)^{2m}} \quad [31]$$

Eq. 31 has a simple pole at

$$\lambda = m - 1 - (a/b)^{2m} = m - 2 + 1 - (a/b)^{2m} \quad [32]$$

with a residue $-2(a/b)^{2m}$. Thus there is a single discrete mode for each m , with the coupling decreasing with m , in accord with earlier work³. Each term in the second form of Eq. 32 can be identified with a frequency shift of a particular origin. The first is a Doppler shift due to plasma rotation. The second is a downshift of the single particle gyration frequency. The third is a plasma upshift giving rise to the upper hybrid frequency. The last is a downshift caused by the image charges in the conducting walls. For $(b/a)^{2m} \gg 1$ the influence of the walls is negligible and this shift may be neglected. In a *neutral* plasma, the first two shifts are absent. Note that the $m=1$ resonance lies below the free particle cyclotron frequency and $m=2$ and higher resonances lie above.

B. Plasma Density Dependent Upon Radius, $m=1$. When the equilibrium density, and therefore the rotational angular velocity, described by $f(r)$ and $g(r)$ respectively, depends on radius the situation is more complicated, except for $m=1$. For $m=1$, the radial dependence in the denominator of Eq. 27a disappears and $R_1(b)$ is readily found to be

$$R_1(b) = -\frac{1}{\lambda} \left[\frac{1}{b^2} \int_0^b f(r) 2r dr \right] = -\frac{\langle f \rangle}{\lambda} \quad [33]$$

and

$$\frac{R_1+1}{R_1-1} = \frac{\lambda - \langle f \rangle}{\lambda + \langle f \rangle} \quad [33a]$$

where $\langle f \rangle$ is the average of f over the entire cross-section. Thus the $m=1$ resonance occurs at $\lambda = -\langle f \rangle$, i.e it is downshifted and the downshift depends solely on the density averaged over the cross section. This *downshift is exactly equal to the frequency of the low frequency $m=1$ diocotron mode*¹³. In

Both the $m=1$ cyclotron mode and the $m=1$ diocotron mode are center of mass modes. The *downshift* of the cyclotron mode and the frequency of the diocotron mode both arise from image charges in the conducting wall, as evidenced by the fact that as a/b tends to zero (wall far away) both vanish. Wall charges produce a *downshift* because the force which they cause on the charged particles is antiparallel to the $\underline{v} \times \underline{B}$ force, thus reducing slightly the frequency of circular motion. The sum of the frequencies of the downshifted cyclotron mode and low frequency diocotron mode is equal to $\omega_c = eB_0/m_e$.

C. Plasma Density Dependent Upon Radius, $m>1$. The behaviour of the $m>1$ modes is not as simple as for $m=1$ when the density depends upon radius. Then the denominator of Eq. 27a will vanish at at some radius where $\lambda=(m-1)g(r)$. This is just the condition at which the dielectric function K vanishes and therefore E_- becomes very large. This condition is satisfied only at a particular radius, which depends upon the frequency λ , so there is a localized resonant layer, the upper-hybrid layer for a non-neutral plasma. Denoting the minimum and maximum normalized rotation frequencies where $f \neq 0$, then an upper hybrid resonant layer occurs in the frequency band

$$(m-1)g_{\min} < \lambda < (m-1)g_{\max}. \quad [34]$$

One can look at this another way. In the frequency band just described, there exists a *continuum* of singular normal modes, with singularity occurring at the radius r_s where $(m-1)g(r_s)=\lambda$. Based on the previous analysis, a prescription for finding the field of a singular normal modes is as follows. For a particular m , pick a frequency λ in the proper frequency band. Find $E_-(r)$ from Eq. 23 by interpreting $1/K(r) = P\{1/K(r)\} + \mu\delta(r-r_s)$ where $P\{ \}$

stands for the principal value and μ is a constant to be determined.

Substitute this result into Eq. 25 to find $E_+(r)$. Finally, determine the constant μ by requiring that $2iE_\theta(b)=E_+(b)-E_-(b)=0$, since $r=b$ is a conducting boundary.

For the evaluation of the R_m 's which appear in the admittance function Y , we can regard Eq. 29 as resulting from the analysis of an initial value problem in which λ has a positive imaginary part, thus resolving the question of how to handle the singularity at $r=r_s$. Alternatively, we could have assumed the existence of a small collision frequency in the earlier analysis and this would have the effect of replacing λ by $\lambda+i\nu$. For the purpose of evaluating and displaying the various multipole contributions to the admittance function, Eq. 29, we follow the latter approach, taking the limit of very small ν . For the parabolic profiles previously discussed, the expression for $R_m(b)$ can be integrated to give

$$R_m(b) = -2m\left(\frac{a}{b}\right)^{2m} \left[\sum_{k=0}^{m-2} \frac{\Lambda^k}{(m-k)(m-k-1)} - \Lambda^{m-1} - \Lambda^{m-1}(\Lambda-1)\ln\left(\frac{\Lambda-1}{\Lambda}\right) \right] \quad [35]$$

where $\Lambda = -2(\lambda-m+1)/(m-1)$. When $0 < \Lambda < 1$, the logarithm is complex and this leads to a complex admittance function representing absorption associated with a resonant layer in the plasma. The frequency band in which this occurs is just that given by Eq. 34 with $g_{\min}=.5$ and $g_{\max}=1$. In particular for $m=2$,

$$R_2(b) = -2\left(\frac{a}{b}\right)^4 \left[(4\lambda-3) - 4(1-\lambda)(2\lambda-1)\ln\left(\frac{1-2\lambda}{2(1-\lambda)}\right) \right]. \quad [35a]$$

In Fig. 3 we display the real and imaginary parts of $(R_2(b)+1)/(R_2(b)-1)$, the main factor in the admittance Y as a function of λ . We also display the magnitude of the perturbed density $n_1(r)$, obtained from Eq. 24, for selected λ . This clearly displays both the absorption band in which Y has a real part,

and the existence of a localized upper hybrid resonance layer and the dependence of its position on λ .

VII. RESONANCES OF THE WARM PLASMA.

The previous discussion assumed zero temperature electrons and this led to singular electric fields at the radius where $K(r)$ vanishes. Under these conditions, finite Larmor radius effects are important and lead to significant modifications of the behavior described above. Singular eigenmodes are no longer possible and Bernstein modes, propagating across the magnetic field, become possible. We now give an approximate treatment of consequences of finite Larmor radius effects by modifying the dielectric function $K(r)$ obtained earlier to include finite Larmor radius effects, to first order in the plasma temperature. When the disturbance takes the form of a plane wave with wave number k , the effect of finite Larmor radius of the particles is to *reduce the effectiveness of the electric field* in producing plasma currents by a factor $4 I_1(k^2 \rho^2/2) e^{-(k^2 \rho^2/2)} / (k\rho)^2$ where ρ^2 is the mean square Larmor radius, averaged over a Maxwellian distribution. To first order in $(k\rho)^2$, i.e to first order in the temperature, this factor is approximately $1 - .5(k\rho)^2$. This approximation is useful so long as the Larmor radius is small compared with the wavelength. Since the particles average the electric field over the orbit, the dielectric function is no longer local. Neighboring regions of the plasma are coupled together and the continuum of singular normal modes is replaced by a discrete set of Bernstein modes. We apply this result to a situation where the waves are not strictly plane waves because the plasma properties vary slowly with position. This approximation is useful so long as the wavelength of the wave is small compared with the distance over which the

plasma properties vary. This leads to the following modification of the dielectric function

$$K(r) = 1 - \frac{f[1 - .5(k\rho)^2]}{\lambda - mg + g + f} \quad [36]$$

where f and g have their previous meanings and are functions of radius. However, it should be pointed out that while we have included temperature to first order in the form of finite FLR effects in the wave dynamics, we have *not* included the effect of temperature in the form of the diamagnetic contribution to the angular velocity. This will modify slightly the relationship between f and g . As before, Eq. 36. is valid only around the cyclotron frequency. We now apply this result to the non-plane wave fields replacing k^2 by $-\nabla^2$, the Laplace operator. This assumes that the density and angular velocity scale lengths are large compared to the wavelength of the waves. This leads to an approximate wave equation for the Bernstein modes which will determine the eigenmodes of the system,

$$\frac{1}{r} \frac{d}{dr}(rR) - \frac{m^2}{r^2} R + k^2(r) R = 0 \quad [37]$$

where

$$k^2(r) = \frac{2[(m-1)g(r) - \lambda]}{\rho^2 f(r)} \quad [38]$$

$k(r)$ could be interpreted as the local wave number and it obviously depends upon radius through $g(r)$ and $f(r)$. When $k^2(r) > 0$ the waves are propagating and when $k^2(r) < 0$ the waves are evanescent, with $k=0$ defining the turning point.

To proceed further, we need to make an assumption about the density profile function $f(r)$. According to Eq. 8a this also determines the angular velocity profile function $g(r)$. For simplicity we use the parabolic density and angular velocity profiles illustrated in Fig. 2. We note that this choice

of $f(r)$ is very close to a diffusion profile, $f(r) = J_0(2.405 r/a)$ if $a = b$, the radius of the wall. For $(m-1)g(r) > \lambda$ the Bernstein waves are propagating and for $(m-1)g(r) < \lambda$ the waves are evanescent. For $m > 1$ and λ a little less than $(m-1)$ the waves are *trapped in the inner part of the plasma column and evanescent in the outer part of the column* (like the Buchsbaum-Hasegawa modes⁹ near $2\omega_c$ and opposite from the Tonks-Dattner modes¹³ near ω_p , which are trapped in the outer region of the plasma. The lowest modes are trapped quite close to the center where $f(r) \approx 1$. If we make this approximation in Eq. 38 then Eq. 37 becomes the two-dimensional harmonic oscillator equation for which the eigenvalues are readily shown to be

$$\lambda_{\ell m} = (m-1) - \sqrt{m-1} (2\ell+m-1) \frac{\rho}{a}, \quad [40]$$

where ℓ is the radial mode number.

Alternatively, Eq. 37 can be integrated numerically to obtain the eigenvalues. The appropriate boundary conditions are $E_- \sim r^{m-1}$ near the origin and $E_- = 0$ at $r = a$ (one solution of Eq. 37 can be shown to have such behavior at $r = a$). One begins the integration at $r=0$ and adjusts the eigenvalue λ in successive integrations so as to assure the the eigenfunction vanishes at $r=a$. The radial dependences of the first few $m=2$ modes obtained in this manner are shown in Fig. 4. One can see from Fig. 4 that the turning point for successively higher radial trapped Bernstein modes is closer to the plasma edge and would, for some higher radial mode number, approach the wall. Under these circumstances, the evanescent layer becomes thin and one can no longer argue that the conditions at the edge of the plasma are unimportant. Thus this approximate approach breaks down for very high radial mode numbers. The eigenvalues obtained are plotted in Fig. 5 for the range $0 < \rho/a < .05$. For very small values of this parameter (low temperature) the

Bernstein mode spectrum is very dense, approaching a continuous spectrum, as found earlier, when $T \rightarrow 0$. For a given $m > 0$, the eigenvalues all have $\lambda < m-1$, and for this profile $\lambda > (m-1)/2$.

VIII. EXTENSION TO MULTIPLE ION SPECIES. Only a few changes are required to extend the previous results to two or more ion species. This extension is motivated by the recent experiments of Sarid et al¹⁴. First, we limit the discussion to two species for simplicity. Second, because the particles have positive charge, they gyrate in the opposite direction, the plasma rotation is in the opposite direction, and fields which can drive cyclotron resonance have the opposite polarization. In the discussion below, we simply ignore these changes in sign and extend the previous analysis for electrons of different mass, and make appropriate changes. Thus the quantities ω_c and ω_0 below are positive. As before we characterize the density profiles of the two species by

$$n_{01}(r) = n_{01}(0) f_1(r) \quad f_1(0) = 1 \quad [40a]$$

$$n_{02}(r) = n_{02}(0) f_2(r) \quad f_2(0) = 1. \quad [40b]$$

The $E \times B$ angular velocity of each species is the same so we define a common angular velocity function $g(r)$,

$$\omega_0(r) = \omega_0(0) g(r) \quad g(0) = 1 \quad [41]$$

where

$$\omega_0(0) = \frac{\omega_{p1}^2(0)}{2\omega_{c1}} + \frac{\omega_{p2}^2(0)}{2\omega_{c2}}. \quad [42]$$

If we let $\epsilon_2 = \omega_{p2}^2/2\omega_{c2} / (\omega_{p2}^2/2\omega_{c2} + \omega_{p1}^2/2\omega_{c1})$ be the charge fraction of species 2, then Eq. 8a becomes (using a similar definition for ϵ_1 ,

$$\frac{1}{r} \frac{d}{dr} [r^2 g(r)] = 2[\epsilon_1 f_1(r) + \epsilon_2 f_2(r)]. \quad [43]$$

When $f_1(r)$ and $f_2(r)$ are specified the $g(r)$ is determined. For example if $f_1(r) = 1 - \alpha_1(r/a)^2$ and $f_2(r) = 1 - \alpha_2(r/a)^2$ then

$$g(r) = 1 - \frac{\alpha_1 \epsilon_1 + \alpha_2 \epsilon_2}{2} \left(\frac{r}{a}\right)^2. \quad [44]$$

Parabolic profiles serve as simple illustrative examples of diffusion-like non-rigid rotor profiles, and reduce to $T=0$ rigid rotor profiles when the α 's are set to zero.

We now examine cyclotron resonance when the frequency is near the cyclotron frequency of species 1. The dynamics of species 2 can be ignored, since it is far from resonance. However its effect on $\omega_0(r)$ has been included in $g(r)$. As before, we introduce a normalized frequency shift, λ_1 , for the mode near $\omega \approx \omega_{c1}$, normalized to the central rotation frequency

$$\omega = \omega_{c1} + \omega_0(0) \lambda_1 \quad [45]$$

The analysis leading up to Eq. 19 is unchanged, except that $f(r)$ is replaced by $\epsilon_1 f_1(r)$. The dielectric function for circularly polarized fields becomes

$$K(r) = 1 - \frac{\epsilon_1 f_1(r)}{\lambda_1 - (m-1)g(r) - .5rdg(r)/dr}$$

and when we use Eq. 43 and solve for $1/K - 1$ we obtain

$$\frac{1}{K(r)} - 1 = \frac{\epsilon_1 f_1}{\lambda_1 - (m-1)g + \epsilon_2 f_2}. \quad [46]$$

with a similar expression (with subscripts 1 and 2 interchanged) when $\omega \approx \omega_{c2}$.

For the plasma extending to $r=a$ and the wall at $r=b$ we get

$$R_m(b) = -\frac{1}{b^{2m}} \int_0^a \frac{\epsilon_1 f_1}{\lambda_1 - (m-1)g + \epsilon_2 f_2} 2mr^{2m-1} dr \quad [47]$$

This gives the behavior when the frequency is in the vicinity of ω_{c1} and a

similar expression (with the subscripts 1 and 2 interchanged) gives the behavior when the frequency is in the vicinity of ω_{c2} . When $\epsilon_2=0$, no second species, and $m=1$ we recover Eq. 33, our previous single species result. As in the single species case, the two-species integrals such as Eq. 47 can be evaluated in the case of a parabolic density profile, and this evaluation leads to logarithmic functions as given in Eq. 35. A. Plasma Density Independent of Radius. For rigid rotor, or "top hat" profiles,

$f_1(r)=f_2(r)=g(r)=1$ for $r \leq a$ so that

$$R_m(b) = - \frac{\epsilon_1}{\lambda_1 - (m-1) + \epsilon_2} \left(\frac{a}{b}\right)^{2m}, \quad \omega \approx \omega_{c1}$$

$$R_m(b) = - \frac{\epsilon_2}{\lambda_2 - (m-1) + \epsilon_1} \left(\frac{a}{b}\right)^{2m}, \quad \omega \approx \omega_{c2}$$

The resonant modes are obtained by setting $R_m(b)$ equal to unity and this gives

$$\lambda_1 = (m-1) - \epsilon_2 - \frac{a^{2m}}{b^{2m}} \epsilon_1, \quad \omega \approx \omega_{c1} \quad [48a]$$

$$\lambda_2 = (m-1) - \epsilon_1 - \frac{a^{2m}}{b^{2m}} \epsilon_2, \quad \omega \approx \omega_{c2}. \quad [48b]$$

Upon comparison with Eq. 32 we see that the terms involving ϵ describe the changes in resonant frequencies arising from the presence of a another species. For the center of mass modes ($m = 1$),

$$\lambda_1 = - \frac{a^2}{b^2} - \left(1 - \frac{a^2}{b^2}\right) \epsilon_2, \quad [49a]$$

$$\lambda_2 = - \frac{a^2}{b^2} - \left(1 - \frac{a^2}{b^2}\right) \epsilon_1. \quad [49b]$$

where we have used the fact that $\epsilon_1 + \epsilon_2 = 1$. The second term, proportional to the density of the other species, represents an additional downshift caused by the presence of the other species.

B. Plasma Density Dependent Upon Radius. We now consider density profile effects and, for simplicity, limit our discussion to the parabolic profiles used earlier. When we examine Eq. 47, and the similar expression with subscripts 1 and 2 interchanged, we note that it is possible for the denominator of the integral to vanish at some radius in certain frequency bands. In the cold plasma theory this signifies absorption bands and in the warm plasma theory these are the bands in which the Bernstein modes may be found. To determine these frequency bands consider the vanishing of the denominator with the assumed profiles. Note that bands associated with *each* of the species is expected. The denominator for the species 1 resonance has the form

$$\lambda_1 - (m-1)\left(1 - \frac{\alpha}{2} \frac{r^2}{a^2}\right) + \epsilon_2 \left(1 - \alpha \frac{r^2}{a^2}\right)$$

where, for simplicity, we assume that $\alpha_1 = \alpha_2 = \alpha$, i.e. that both species have the same density profile. Vanishing of this denominator at $r=0$ and $r=a$ serves to determine the limits of the absorption bands. These limits are, for species 1,

$$\lambda_1 = (m-1) - \epsilon_2 \quad [50a]$$

$$\lambda_1 = (m-1)\left(1 - \frac{\alpha}{2}\right) - \epsilon_2(1-\alpha) \quad [50b]$$

with similar expressions for the limits associated with the second species. For the center of mass modes ($m=1$), the frequencies of these two bands can be described as

$$-\epsilon_2 \leq \lambda_1 \leq -\epsilon_2(1-\alpha) \quad [51a]$$

$$-\epsilon_1 \leq \lambda_2 \leq -\epsilon_1(1-\alpha), \quad [51b]$$

i.e. both bands lie *below* their respective cyclotron frequencies. From this result, we see that, unless the density is independent of radius ($\alpha=0$,

top-hat distributions), there are now *absorption bands associated with the $m=1$ cyclotron modes*, whereas for the single species case, there was only a single discrete resonance. We speculate that the inclusion of temperature will lead to Bernstein modes in these bands.

IX. SUMMARY AND CONCLUSIONS.

We have studied the $k_z=0$ cyclotron modes of a cylindrical nonneutral plasma of low density ($\omega_p^2/\omega_c^2 \ll 1$). Particular attention has been given to a single species (electrons) which is in nonuniform rotation, i.e. where the density and angular velocity are functions of radius. We have illustrated the general features of the behavior near cyclotron resonance by using a simple parabolic profile. The qualitative behavior for other monotonically decreasing profiles is similar but differs in details. A We have obtained the admittance function, $Y(\omega)$, which characterizes the current flowing to a segment of the wall when an oscillating potential whose frequency is near the cyclotron frequency is applied to that segment. An absorption band is found for each m value, for the range of frequencies for which a local upper hybrid resonance occurs at some radius in the nonuniform plasma. These absorption bands correspond the the frequency bands in which the plasma has a continuum of singular eigenfunctions, although that approach is not persued here. The plasma responds only to the circularly polarized component of the electric field which has the same sense as the gyrating charged particles and, because of plasma rotation, the each absorption band is upshifted by the Doppler effect. $m=1$ is found to be a special case with only a single discrete mode and no continuum, a property which it shares with the low frequency $m=1$ diocotron mode. Both are center of mass modes. Presumably in both cases an $m=1$ continuum of singular eigenmodes exists but they have no electric field

exterior to the plasma, and therefore not observable, or excitable, with electrodes exterior to the plasma. The $m=1$ cyclotron mode was shown to have a frequency which lies below the cyclotron frequency by an amount equal to the low frequency diocotron mode frequency $\langle \omega_p^2 \rangle / 2\omega_c$, where the average is taken over the cross section of the cylinder.

When finite Larmor radius effects, owing to plasma temperature, are taken into account in an approximate fashion, Bernstein modes are found in the frequency bands for which the cold plasma theory predicts an absorption continuum associated with the continuous spectrum of singular eigenmodes. Because of the radial density and angular profiles the Bernstein modes are trapped in the central core of the plasma. They are traveling waves in the azimuthal direction and standing waves in the radial direction. The relative frequency spacing between modes with different numbers of radial nodes is proportional to the ratio of Larmor radius to gradient scale length, a small quantity. The Bernstein mode spacing can be used to estimate the plasma temperature. Finally, we have outlined an extension of the cold plasma results to plasmas with multiple ion species.

A more complete theory of the trapped Bernstein modes in a cylindrical nonuniform nonneutral plasma, such as a solution of the Vlasov equation to first order in the temperature, is desirable. This approach has been used in Ref. 6 for a neutral plasma and in Ref. 8 for a planar nonneutral plasma. In order to carry out such an analysis one would also have to find a suitable steady state with radial profiles of the density and angular velocity which includes the diamagnetic drifts as well as the $E \times B$ drifts.

ACKNOWLEDGEMENT. The author is pleased to acknowledge E. Sarid for

discussion of his experimental results and the Office of Naval Research for support of this work under Grant N000014-89-J-1264.

REFERENCES

1. Roy W. Gould and Michael A. LaPointe, Phys. Rev. Lett. 67, 3685 (1991); Phys. Fluids B4, 2038 (1992).
2. *Non-Neutral Plasma Physics*, AIP Conf. Proc. 175, edited by C. W. Roberson and C. F. Driscoll (AIP, New York, 1988).
3. R. C. Davidson, *Physics of Nonneutral Plasmas* (Addison Wesley, Redwood City, CA, 1990).
4. R. C. Davidson and N. A. Krall, Phys. Rev. Lett. 22, 833 (1969); Phys. Fluids 13, 1543 (1970).
5. D. H. E. Dubin, Phys. Rev. Lett. 66, 2076 (1991).
6. G. A. Pearson, Phys. Fluids 9, 2454 (1966).
7. I. B. Bernstein, Phys. Rev. 109, 10 (1958).
8. S. A. Prasad, G. J. Morales, and B. D. Fried, Phys. Fluids 30, 3093 (1987).
9. S. J. Buchsbaum and A. Hasegawa, Phys. Rev. Lett. 12, 685, (1964); Phys. Rev. 143, 303 (1966).
10. For a good review of Bernstein waves in neutral plasmas, see G. Bekefi, *Radiation Processes in Plasmas* (Wiley, New York, 1966).
11. N. G. Van Kampen, Physica, 21 949 (1955).
12. K. M. Case, Annals of Phys. 7, 349 (1959).
13. J. V. Parker, J. C. Nickel, and R. W. Gould, Phys. Rev. Lett. 11, 183 (1963); Phys. Fluids, 7, 1489 (1964).
14. E. Sarid, F. Anderegg, and C. F. Driscoll, Bull. Am. Phys. Soc. 38, 1971 (1993).

FIGURE CAPTIONS

Figure 1. Schematic diagram of the plasma, surrounding electrodes, and driving circuitry (end view), with definition of $Y(\omega)$, the plasma admittance function with $\omega = \omega_c + \omega_0(0)\lambda$.

Figure 2. Illustrative density and angular velocity profiles of a rotating nonneutral plasma, normalized to their central values.

$$f(x) = n_0(x)/n_0(0), \quad g(x) = \omega_0(x)/\omega_0(0), \quad x = r/a.$$

Figure 3. Admittance versus frequency for the $m = 1, 2, 3, 4$ modes and the profiles shown in Fig. 2. Plotted are the real and imaginary parts of the plasma contribution, $2R_m(b)/[R_m(b)-1]$. The ratio of wall radius, b , to plasma radius, a is 1.25. Plots for $m = 3$ and 4 have been expanded by factors of 5 and 10 with respect to $m = 2$ for clarity in presentation.

Figure 4. Radial Wave Functions for $m=2$, $\rho/a=0.02$, with their normalized frequencies. The first five radial modes are shown.

Figure 5. Theoretical spacing of the trapped $m=2$ Bernstein modes versus Larmor radius, ρ/a , normalized to the *central* rotation frequency

$$f_p^2(0)/2f_c \text{ for the profiles of Fig. 2.}$$

$$Y(\omega) = \frac{I(\omega)}{V(\omega)}$$

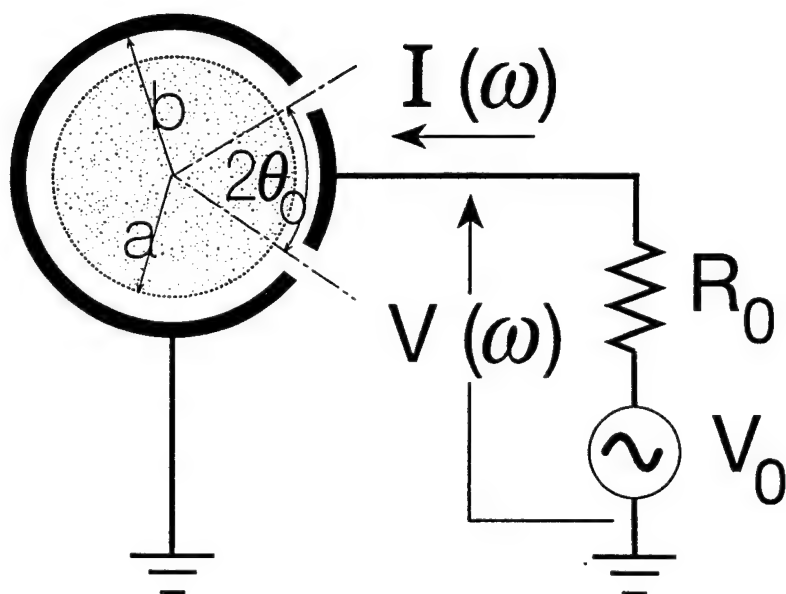


FIG. 1. Schematic diagram of the plasma, surrounding electrodes, and driving circuitry (end view), with definition of $Y(\omega)$, the plasma admittance function with $\omega = \omega_c + \omega_0(0)\lambda$.

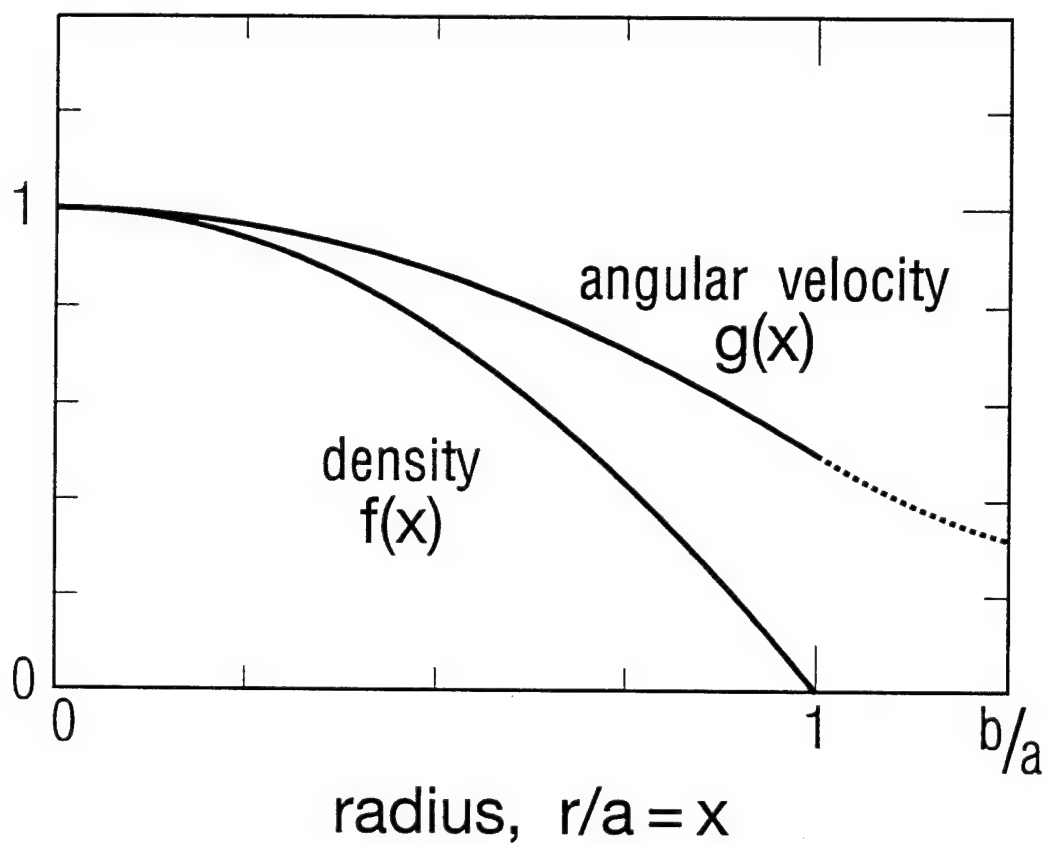


FIG. 2. Illustrative density and angular velocity profiles of a rotating nonneutral plasma, normalized to their central values: $f(x) = n_0(x)/n_0(0)$, $g(x) = \omega_0(x)/\omega_0(0)$, $x = r/a$.

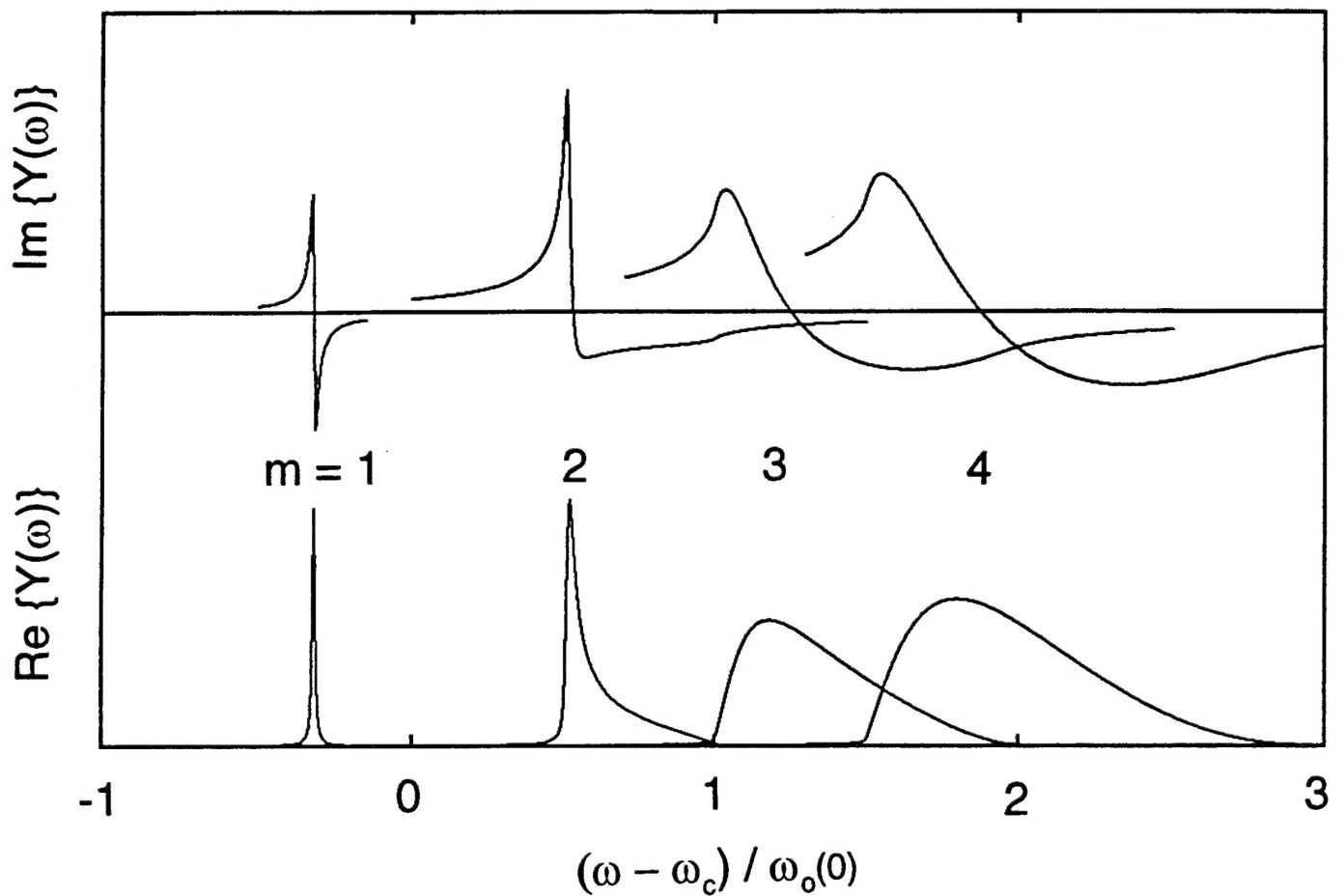


FIG. 3. Admittance versus frequency for the $m=1,2,3,4$ modes and the profiles shown in Fig. 2. Plotted are the real and imaginary parts of the plasma contribution, $2R_m(b)/[R_m(b)-1]$. The ratio of wall radius to plasma radius, b/a , is 1.25. Plots for $m=3$ and 4 have been expanded by factors of 5 and 10 with respect to the $m=2$ for clarity in presentation

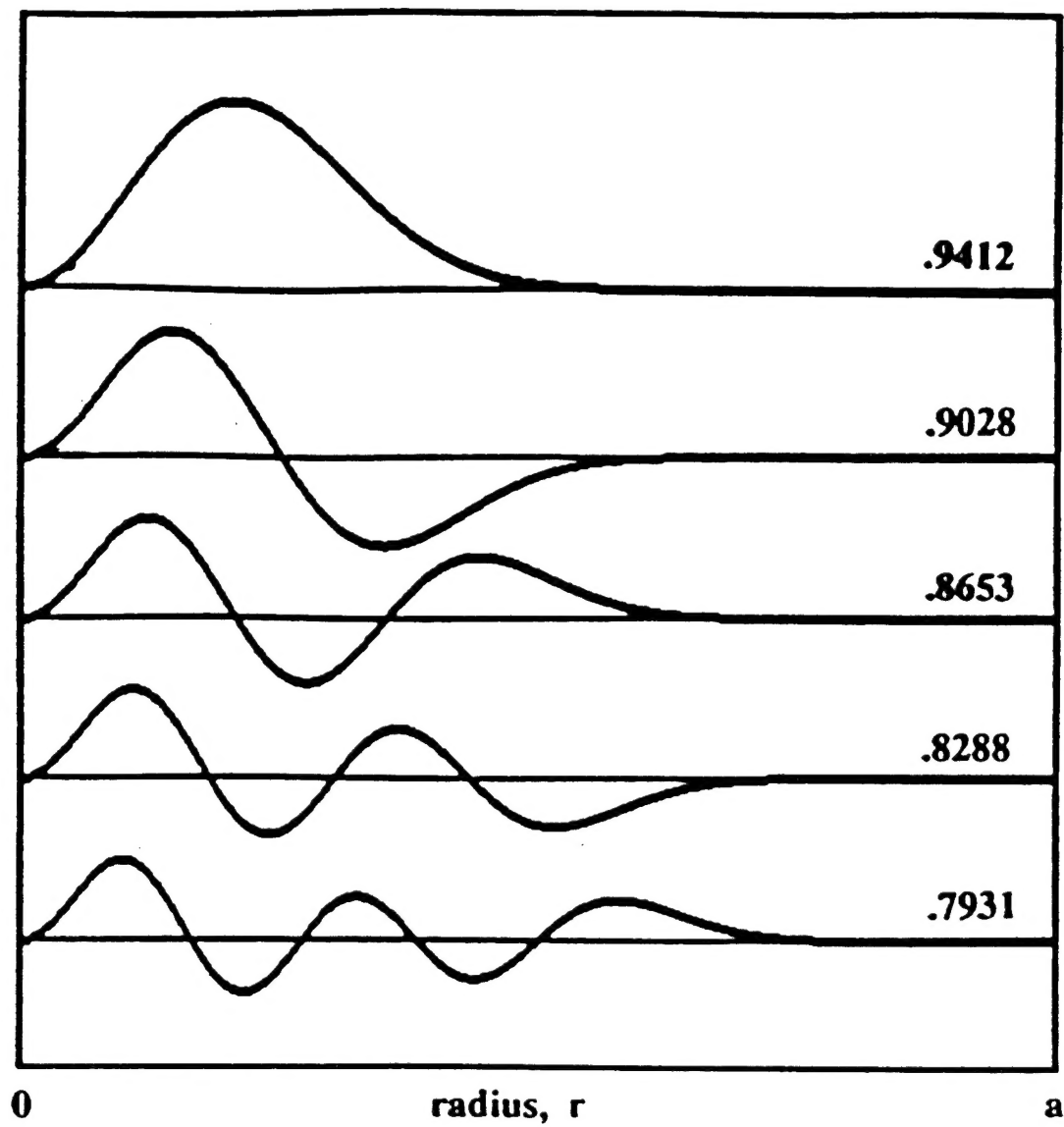


Fig. 4. Radial wave functions for $m = 2$, $\rho/a = 0.02$, with their normalized frequencies. The first five modes are shown.

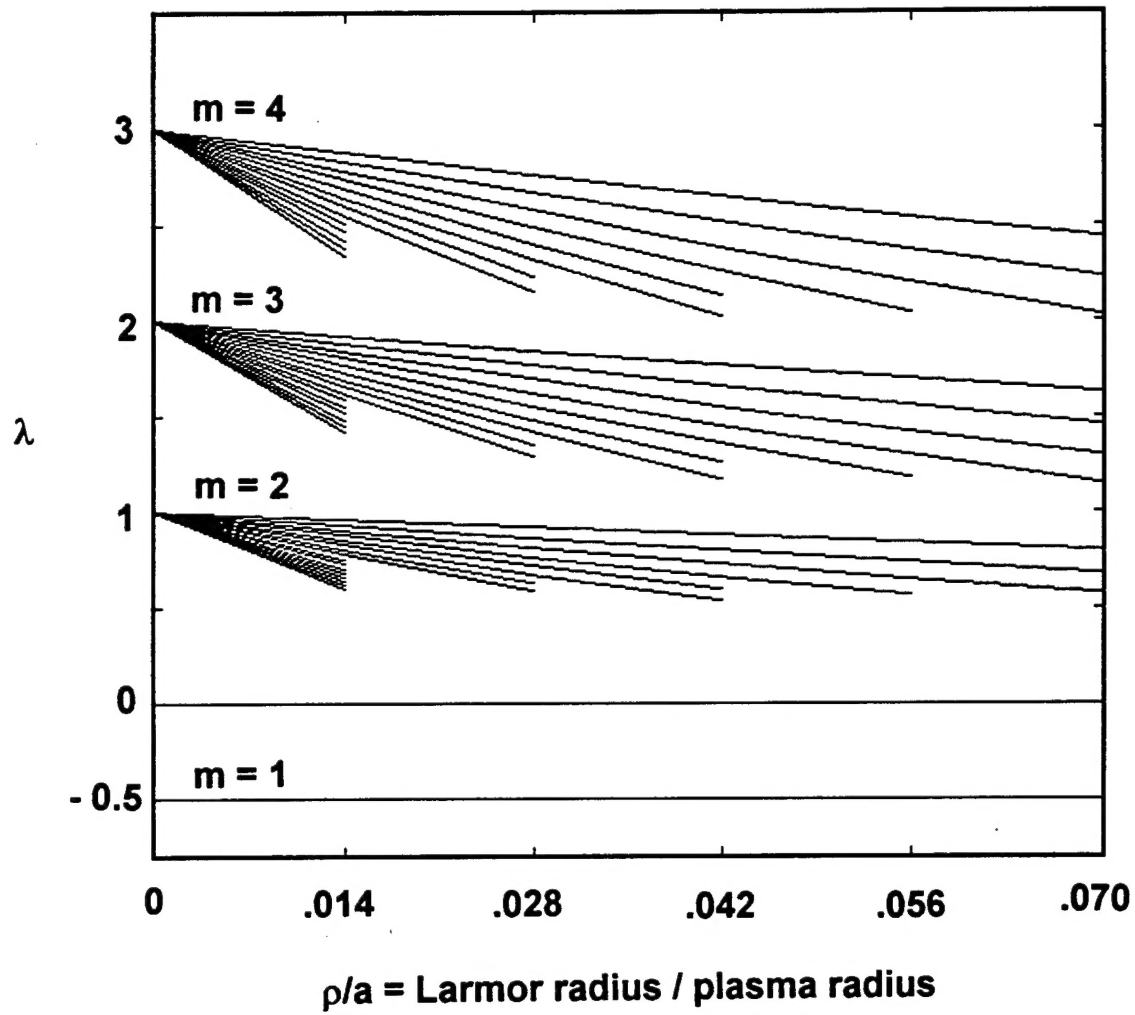


Fig. 5. Theoretical spacing of the trapped $m = 2$ Bernstein modes versus Larmor radius, ρ/a , normalized to the central rotation frequency $f_p^2 / 2f_c$ for the profiles of Fig. 2.

Papers Presented at the
1994 Meeting of the Plasma Physics Division
of the American Physical Society
Minneapolis, MN - Nov. 10 1994

SESSION 7RV: DYNAMICS OF NON-NEUTRAL PLASMAS
Thursday morning, 10 November 1994; Nicollet Ballroom at 8:15; A. Trivelpiece, presiding

7RV 1
Dynamics of Nonneutral Plasmas.
ROY W. GOULD, *California Institute of Technology.*

8R 19 Negative Energy and Dispersion of the Diocotron Resonances*. Sateesh Pillai and Roy W. Gould, *California Institute of Technology.* A cylindrical column of pure electron plasma exhibits characteristic quasi-mode "diocotron" resonances around the angular rotation frequencies. These are resonances caused by the fluid nature of the system and are identified with the eigen number " m " corresponding to its circular symmetry. It has been experimentally demonstrated that the undamped $m=1$ diocotron is a negative energy mode¹. The $m=2$ quasi-mode is normally damped by a collisionless process². We present first experimental evidence showing that the addition of external resistors to the wall segments decrease the damping rate for the $m=2$ mode, demonstrating that the $m=2$ diocotron is also a negative energy mode. Based on the linear theory the higher diocotron modes are also negative energy modes.

The dispersion characteristics of the diocotron modes for a particular profile will also be presented.

1. W.D. White, J.H. Malmberg and C.F. Driscoll, *Phys. Rev. Letters* 49, 1822 (1982)

2. S. Pillai and R.W. Gould, *BAPS* November 1993

* Research supported by the U.S. Office of Naval Research

8R 20 Numerical Collisionless Damping of the Diocotron Resonance*. David A. Bachman and Roy W. Gould, *California Institute of Technology.* A cylindrical pure electron plasma features diocotron resonances near the angular rotation frequency. These resonances are characterized by their circular symmetry. Experimentally, the $m=2$ diocotron mode is found to decay by a collisionless process. Additionally, a solution of the linearized fluid equations for representative density and angular profiles also gives collisionless decay.

A two dimensional nonlinear fluid code of a pure electron plasma has been used to study the plasma response to an applied pulse. The fluid code also exhibits the collisionless damping of the $m=2$ diocotron mode, and the damping rate of this mode found from the nonlinear fluid code matches the damping rate found from the linearized numerical calculation.

* Research supported by the U.S. Office of Naval Research